https://ntrs.nasa.gov/search.jsp?R=19880001298 2020-03-20T08:43:53+00:00Z

Final Report

NAS-5-26466

OPTIMIZATION OF SIS MIXER ELEMENTS

Submitted to:

National Aeronautics and Space Administration
Goddard Space Flight Center
Greenbelt, Maryland 20771

Attention: Dr. Anthony Kerr
Code 130

Submitted by:

R. J. Mattauch
Principal Investigator

Department of Electrical Engineering
SCHOOL OF ENGINEERING AND APPLIED SCIENCE
UNIVERSITY OF VIRGINIA
CHARLOTTESVILLE, VIRGINIA

Report No. UVA/528204/EE86/101
December 1985

Copy No. ________

1. Report No.	2. Government Accession No.	3. Recipient's Catalog No.
4. Title and Subtitle Optimization of SIS Mixer Elements		5. Report Date December 1985
		6. Performing Organization Code 5-28204
7. Author(s) Dr. Robert J. Mattauch Arthur W. Lichtenberger		8. Performing Organization Report No. UVA/528204/EE86/101
9. Performing Organization Name and Address Semiconductor Device Laboratory University of Virginia Thornton Hall Charlottesville, Virginia 22901		10. Work Unit No.
		11. Contract or Grant No. NAS-5-26466
12. Sponsoring Agency Name and Address National Aeronautics and Space Administration Goddard Space Flight Center Greenbelt, Maryland 20771		13. Type of Report and Period Covered Final Report 3/20/81-8/31/85
		14. Sponsoring Agency Code

15. Supplementary Notes

16. Abstract

Superconductor-Insulator-Superconductor (SIS) quantum mixers provide a new approach to millimeter wave mixing - potentially offering conversion gain, a low local oscillator power demand and potential mixer noise temperatures near the quantum limit. This work is focused on the development of a reliable fabrication technology for producing such high quality SIS devices for mixer applications in radio astronomy.

17. Key Words (Suggested by Author(s))	18. Distribution Statement
SIS, Mixer, Edge junctions	Unlimited

19. Security Classif. (of this report)	20. Security Classif. (of this page)	21. No. of Pages	22. Price
Unclassified	Unclassified	134	

For sale by the National Technical Information Service, Springfield, Virginia 22161

TABLE OF CONTENTS

Page

LIST OF FIGURES.................................... v

LIST OF TABLES..................................... vii

LIST OF SYMBOLS.................................... ix

CHAPTER

1 INTRODUCTION.................................. 1

2 SUPERCONDUCTIVITY - THE PHENOMENA.......... 4

3 SIS TUNNELING THEORY.......................... 31

4 THEORETICAL MODELING.......................... 46

5 INITIAL FABRICATION RESULTS................... 67

6 A SEARCH FOR THE MECHANISM OF DEVICE QUALITY DETERIORATION......................... 81

7 CONCLUSION AND RECOMMENDATION FOR FUTURE RESEARCH............................ 105

APPENDIX A... 107

APPENDIX B... 114

PRECEDING PAGE BLANK NOT FILMED

LIST OF FIGURES

Figure		Page
1.1	SSB noise temperatures for SIS mixer elements at 115 GHz...........................	2
2.1	Specific heat for normal and superconducting states....................................	5
2.2	Entropy for normal and superconducting states....................................	5
2.3	Typical reflection coefficient of a superconductor versus frequency.............	8
2.4	Density of Bloch status versus energy for a normal metal..............................	11
2.5	Fermi-Dirac distribution function...........	11
2.6	Bloch state energies versus crystal momentum....................................	11
2.7	Excitation energies defined in terms of Bloch state energies........................	14
2.8	Normal metal excitation energies............	14
2.9	Probability that the double-electron state is occupied..................................	18
2.10	Superconductor energy gap dependence on temperature..................................	18
2.11	Probability of pair occupancy in the superconducting state........................	20
2.12	Permitted excitation energies for a superconductor with energy gap Δ............	20
2.13	Graphical construction of d and dE for an incremental interval of momentum dp.........	22
2.14	Expanded view of the superconductor excitation energy mean P_p..................	24
2.15	Graphical analysis of $N_s(E)$.................	25

Figure		Page

2.16	Superconductor density of states $N_sJ(E)$ shown to scale for Δ = 1.5 meV.............	28
2.17	Superconductor density of states $N_s(E)$ in the semiconductor representation.........	30
3.1a	Electron population diagram for a normal metal, T=0................................	32
3.1b	Electron population diagram for a normal metal, T > 0..............................	32
3.2	Excitation tunneling diagram for a NIN junction..................................	34
3.3a	Excitation tunneling diagram for a NIS junction..................................	34
3.3b	Graphical demonstration that $U_j^2+U_k^2 = 1$....	34
3.4	Semiconductor representation of a NIS junction for T=0...........................	36
3.5	Excitation tunneling diagram of a SIS junction..................................	36
3.6	Semiconductor representation of an SIS junction for T=0 with eV = $\Delta_1 + \Delta_2$...........	38
3.7	Semiconductor representation of a SIS junction for T > 0..........................	38
3.8	Semiconductor representation at T=0 for a positive bias (eV = $\Delta_1 + \Delta_2$) applied to metal two................................	40
3.9	SIS I-V curve for T=0......................	40
3.10	Semiconductor model, T > 0, eV = $\Delta_2 - \Delta_1$....	42
3.11	Typical ideal I-V curve for an SIS junction $\Delta_1 \neq \Delta_2$, T > 0................................	42
3.12	Theoretical I-V curve for an SIS junction Δ_1 = 1.44 meV, Δ_2 = 1.7 meV................	45
4.1	Typical SIS I-V curve with and without L.O. bias..................................	49

Figure		Page
4.2	J_c as a function of barrier thickness d......	53
4.3	J_c versus Q, $(Q = \omega R_n C)$....................	55
4.4	Lines of constant Q and A are shown on a R_n versus C plot for a Nb/PbBi junction........	56
4.5	Lines of constant R_n are shown on an A versus C plot...............................	60
4.6	Lines of constant R_n are shown on a Q versus A plot...............................	61
4.7a	SIS I-V curve, for a case of a graded distribution of effective turn on voltage...	64
4.7b	I-V curve for a NIS junction................	64
5.1	Schematic of a Nb/Pb alloy edge contact device....................................	69
5.2	Base electrode patterning with photoresist..	71
5.3	Gold contact pads on Nb.....................	71
5.4	Counterelectrode photoresist profile........	73
5.5	Typical I-V curve of a Nb/PbBi device for initial results..........................	73
5.6	Tapered edge profile with edge angle of 30°.....................................	76
5.7a	Al_2O_3 pad on top of the Nb film.............	76
5.7b	Photoresist definition prior to base electrode formation with ion miling machine....................................	76
5.7c	Resulting Al_2O_3/Nb base electrode edge structure............................	76
5.8	Initial I-V curve obtained with Al_2O_3 technology................................	80
6.1	Original and replacement designs of the filament assembly..........................	84
6.2	Typical I-V curve obtained with thermal oxidation technology.......................	86

Figure		Page

6.3	Typical I-V curve obtained with extended cleaning step (40 min.)......................	86
6.4	Typical I-V curve obtained with low voltage clean and oxidation (350 volts)............	88
6.5	New vacuum chamber design...................	94
6.6	New vacuum chamber design...................	95
6.7	Initial I-V curve obtained with new chamber.....................................	96
6.8	Resulting I-V curve obtained with new glass insulator rings...........................	98
6.9	I-V curve of the highest quality obtained in this work.......................	99
6.10	SiO_2 window defined junction................	101
6.11	Typical I-V curve obtained with NBS Nb......	104
6.12	Typical I-V curve obtained by Mr. Beall on NBS Nb..................................	104
B.1	Typical ion source schematic................	115
B.2	Variation of potential in a typical dual grid system................................	118
B.3	Schematic of the vacuum system associated with the ion source in this work...........	120

LIST OF SYMBOLS

C	capacitance
C_A	capacitance per unit area
C_l	crystal lattice component of specific heat
C_{el}	conduction electron component of specific heat
C_s	specific heat
d	barrier thickness
E	excitation energy
E_b	energy necessary to break apart a Cooper pair
E_e	electron excitation energy
E_h	hole excitation energy
$f(\varepsilon)$	Fermi-Dirac function
fF	femto farad, 10^{-15}F
GHz	10^9Hz
G_n	conductance of the ohmic device in the normal state
$\hbar$	$h/2\pi$, where h is Planck's constant
h_i^2	probability that a Cooper pair state is occupied
I	current
I_c	critical current
J	current density
J_c	critical current density
k	crystal momentum
K	material tunneling constant

k_B	Boltzmann's constant
mil	.001 inch
mV	10^{-3} volt
m_e	electron mass
$N_n(\varepsilon)$	density-of-Bloch-states
$N_n(E)$	density-of-normal-excitation-states
$N_s(\varepsilon)$	density-of-superconductor-excitation states
$N'_{sx}(E)$	defined as $E/(E^2 - \Delta_x^2)^{1/2}$
p	crystal momentum
P	tunneling probability
p_f	fermi crystal momentum
pf	pico farad, 10^{-12}F
Q	defined as $\omega R_n C$
R_n	normal state resistance
$R_{2,4}$	R(2mV)/R(4mV), the "resistance ratio"
s	entropy
T	temperature
T_c	superconducting transition temperature
u_k^2	probability that state p_k is empty
v	volume per unit mass
V	applied voltage
V_a	accelerating supply voltage
V_{bs}	beam supply voltage
V_d	drop back voltage
V_{dc}	D.C. bias voltage
V_{gap}	gap voltage

V_{LO}	local oscillator voltage
$V(r)$	electric potential presented by a lattice
V_T	defined as $\|V_a\| + V_{bs}$
β	tunneling constant, dependent on the given geometry
ε_o	permittivity of free space
ε_r	dielectric constant
ε	energy of the Bloch state
ε_e	Bloch state energy above ε_F
ε_F	fermi level
ε_n	Bloch state energy below ε_F
λ	wavelength
μA	10^{-6} Amp
μm	micron, 10^{-6} meters
μm^2	micron squared
ϕ	phase difference across the junction of the two pair wave function
ϕ'	probability function for two uncorrelated electrons
Φ'	probability function for a Cooper pair state
π	$2\pi f$, where f is frequency
Γ	reflection coefficient
Δ	energy gap associated with a superconductor
ΔI_{ss}	quasiparticle current jump
Ω	ohm
$\psi(r)$	permitted energy states of Schrodinger equation
Å	Angstrom, 10^{-10}
$\uparrow, \downarrow$	spin up, down

CHAPTER I

Introduction

This work is focused on the development of a reliable fabrication technology for producing high quality Superconductor-Insulator-Superconductor (SIS) junctions for mixer applications in radio astronomy. Schottky barrier diode devices have generally been the standard in radio astronomy for low noise highly sensitive mixers in the millimeter and submillimeter wavelength regions. In the past couple of years, however, the lowest mixer noise temperatures, for frequencies below 115 GHz, have been obtained with SIS devices (see Fig. 1.1) [1]. SIS mixers also require a local oscillator power level several orders of magnitude lower than conventional devices. The potential for conversion gain, predicted by John Tucker in his theory of quantum mixing [2], has been physically realized by several experimentalists [3,4]. Tucker's theory also predicts a minimum mixer noise temperature limited only by quantum noise ($\hbar\omega/k$). These advantages of SIS devices have prompted our research in this area.

Chapter II presents a brief introduction to the phenomena of superconductivity, the concepts of "Cooper pairs", and quasiparticle excitations, and the development of the superconducting density-of-states. In Chapter III, basic SIS tunneling theory is developed and the typical SIS I-V

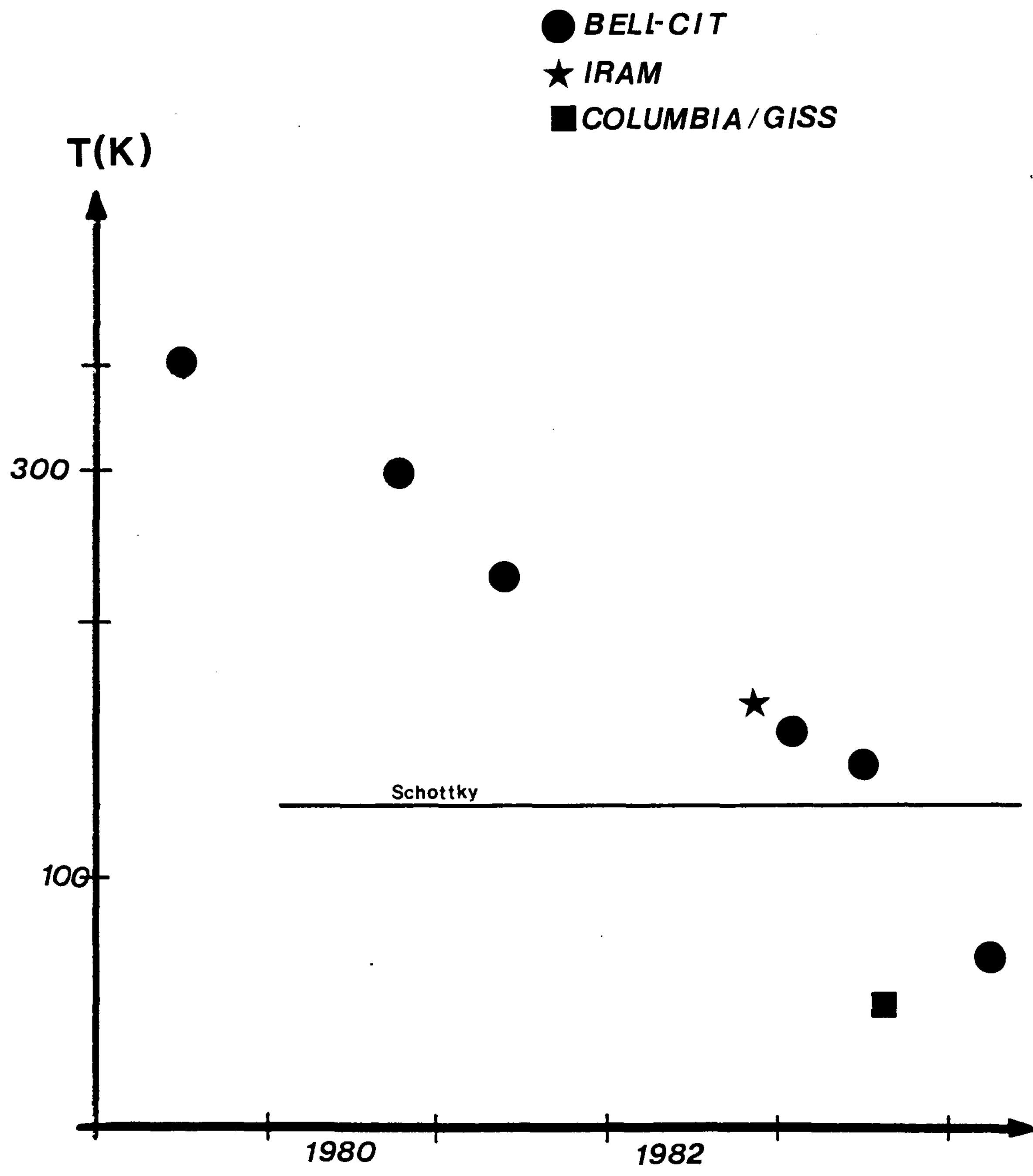

Figure 1.1 SSB noise temperatures for SIS mixer elements at 115 GHz

characteristics are examined. A theoretical modeling of the physical device parameters for use as optimal mixers is developed in Chapter IV. In Chapter V, initial fabrication results are discussed and a subsequent deterioration of device quality examined. The resolution of this degradation problem is presented in Chapter VI and potential avenues for future research are outlined in Chapter VII.

CHAPTER II

Superconductivity - The Phenomena

Superconductivity is a term used to describe the quality of materials which exhibit a state change to zero resistivity when cooled below a critical temperature (T_c). The loss of resistivity is typically abrupt for pure samples, with T_c dependent on the material. Investigation of the properties of metals at very low temperatures followed the discovery of helium liquification by Kammerlingh Onnes in 1908.

The sharply contrasting zero resistivity of superconductors can be better understood by examining the specific heat C_s of the transition. Figure 2.1 reveals a discontinuity in the specific heat at the critical temperature. The expression for the specific heat is given by

$$C_s = vT\, ds/dT, \qquad (2\text{-}1)$$

where v is the volume per unit mass and s is the entropy. An entropy diagram Fig. 2.2 can therefore be obtained from Fig. 2.1.

The specific heat can be separated into two parts - the crystal lattice component C_l and the conduction electrons contribution C_{el}. X-ray crystallographic investigations have shown that lattice properties are unchanged when superconductors are cooled below T_c. The change in specific

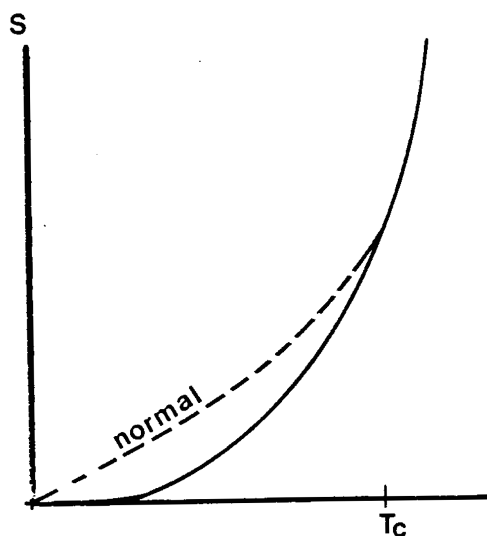

Figure 2.2

Entropy for normal and superconducting states

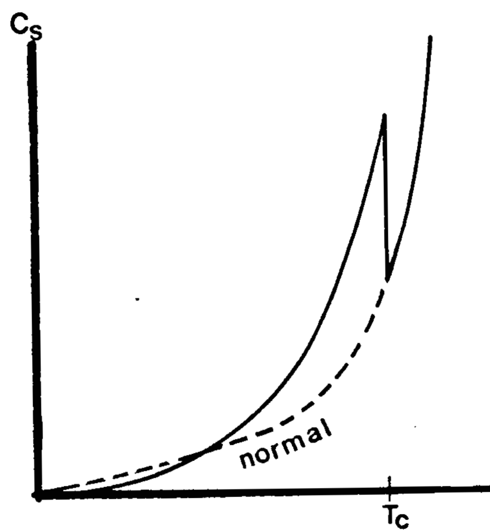

Figure 2.1

Specific heat for normal and superconducting states

heat between superconductors and normal states is therefore due to the conduction electrons. Since the entropy of the superconducting metal decreases with respect to the normal state, the electrons in the superconducting state must undergo a transition to a higher form of order. The electronic specific heat of metals in the superconducting state, far below T_c, has been experimentally shown to have an exponential dependency on T given by

$$C_{el} = a \exp(-b/kT), \qquad (2\text{-}2)$$

where a and b are constant. Such an exponential dependency is expected for materials with a gap in the energy spectrum of the electrons [5]. The existence of an energy gap is crucial to the theory of SIS devices and will be investigated further in this chapter.

The phenomena of zero resistivity for constant direct currents indicates the absence of a voltage drop across the metal. For alternating currents an electric field exists such that resistivity is present. This a.c. resistivity, the general entropy diagram and many other characteristics of superconductors can be explained with a simple, physically appealing, "two-fluid" model. In this model the conduction electrons are separated into two species - "superelectrons", which induce the unusual superconducting properties, and "normal electrons", which behave like electrons in a normal metal. As the temperature is lowered below T_c the fraction

of superelectrons increases from zero until at absolute zero all are superelectrons. In the two fluid model, as the temperature is lowered below T_c, some normal electrons undergo a transition to highly ordered superelectrons, explaining the lower entropy states for the superconducting material.

Constant direct current must be carried by the superelectrons; however, for alternating current, the inertial mass of the superelectrons presents an inductive impedance, causing the superelectrons to lag behind the changing electric field. In an electric field the normal electrons are accelerated, presenting a resistive impedance. Bulk superconductors can therefore be represented by an inductance in parallel with a resistance.

Further evidence of a gap in the energy spectrum of electrons is obtained from studies of reflection coefficients of the superconducting and normal states. A typical absorption curve (Fig. 2.3) [6] shows the existence of an absorption edge, for a superconductor, similar to the infrared radiation edge found with semiconductors. While the semiconductor infrared edge indicates an energy gap on the order of electron volts, the superconductor absorption curves imply a much smaller gap, on the order of milli electron volts. The two fluid model provides no insights for understanding this unusual phenomenon.

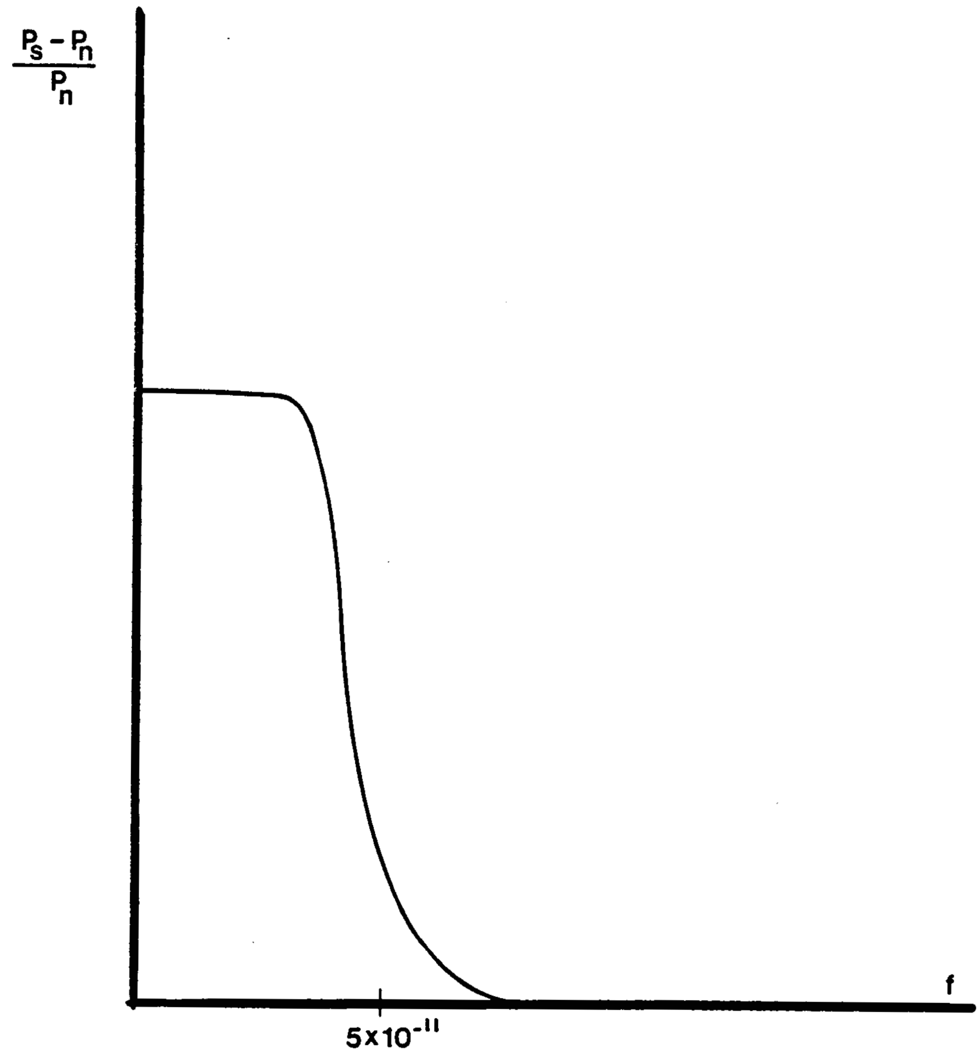

Figure 2.3

Typical reflection coefficient of a superconductor versus frequency

Another interesting phenomena that provides insight into the source of the energy gap is the characteristic of a "long-range order" by the superelectrons. It has been experimentally shown that the physical definition between superconducting and normal material cannot be sharp. The properties of the superelectrons can change significantly only over a distance greater than the "coherence length" - typically of the order of 10^{-4} cm. This long range order implies that an unusual interaction between the electrons occurs. The fairly strong repulsive coulomb interaction can not create an energy gap. The mechanism must be attractive and much weaker to create the small energy gap measured for superconductors. In 1950, Frohlich proved theoretically that two electrons can be coupled together through an electron-phonon interaction. The electrons exchange momentum through the lattice in a virtual process, while the lattice is effectively undisturbed after the exchange. If the energy difference of the electrons, after the virtual phonon transfer, is less than the energy of the phonon, then the interaction will be attractive. This result, though proving the existence of a bound state between two electrons in a lattice, does not address a more realistic case of possible interaction between all of the conduction electrons.

Before examining the BCS theory of superconductivity which followed Frohlich's work, a number of associated terms and notation must be developed. The simple case of the

electron distribution in a normal metal will first be examined, establishing the notation for the more complex superconductive case.

The states that electrons can occupy ((r)) are given by the solution to the Schrodinger equation,

$$-\frac{h^2}{2m}\nabla^2\psi(r) + V(r)\ \psi(r) = \varepsilon\psi(r), \qquad (2\text{-}3)$$

where V(r) is the electric potential presented by the lattice. The solution to (2-3) can be given in the form of Bloch functions. With the well known free-electron model of metals, electrons can occupy Bloch states according to

$$N_n(\varepsilon) = k\sqrt{\varepsilon} \qquad (2\text{-}4)$$

where $N_n(\varepsilon)$ is the density-of-Bloch-states for a normal metal, k is a constant dependent on the electron mass and ε is the energy of the Bloch state. $N_n(\varepsilon)$ is shown in Fig. 2.4. The distribution of electrons with energy is described by the Fermi-Dirac statistics such that the probability of occupancy at energy ε is given by

$$f(\varepsilon) = \frac{1}{1 + \exp[(\varepsilon-\varepsilon_F)/k_BT]} \qquad (2\text{-}5)$$

where ε_F is the Fermi level. This function is shown in Fig. (2.5) for both the $T = 0$ ground state and the $T > 0$ cases. For $T > 0$, it is seen that there exists electron excitations for the case of a normal metal.

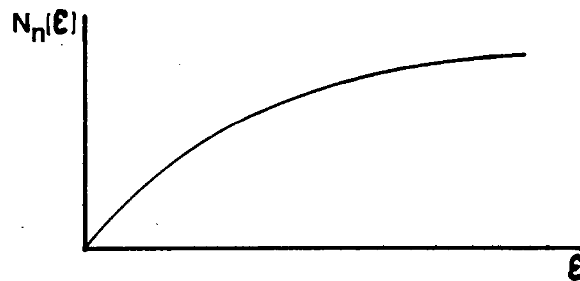

Figure 2.4

Density of Bloch status versus energy for a normal metal

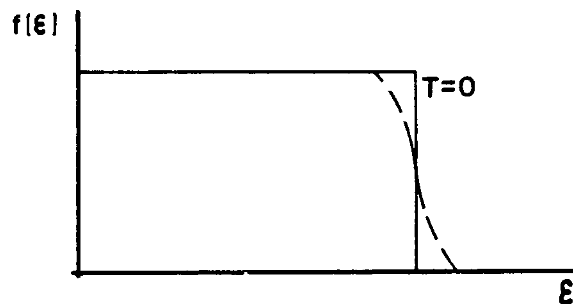

Figure 2.5

Fermi-Dirac distribution function

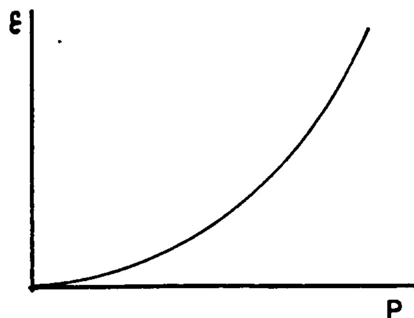

Figure 2.6

Bloch state energies versus crystal momentum

The relationship between Bloch states energies and crystal momentum p, obtained with the free-electron model and the Schrodinger equation, is given by

$$\varepsilon = \frac{h^2}{2m_e} p^2 \tag{2-6}$$

and shown in Fig. (2.6). The ε versus p diagram can be used to illustrate the phenomena of electron excitation from the ground state. Since the density of Bloch states presents a continuum of states in energy, any increase in temperature from T = 0 of the system, will result in electron excitations. It will be shown later in this chapter that this effect does not occur with superconductors, due to the energy gap that exists between the ground state and superconducting excitation states. Bloch states above and below ε_F will be designated by ε_e and ε_h respectively. With the system at T = 0, if conceptually one electron is excited from a Bloch state energy ε_{hj} to ε_{ei}, then the energy of the subsequent state above the ground state is called the excitation energy E. The excitation energy can be thought of as being composed of an electron excitation energy E_{ei} and a hole excitation energy E_{hj}. This definition of excitation energies is illustrated graphically in Fig. (2.7) with respect to Bloch state energies. For this conceptual case, the excitation energy is given by

$$E = E_{ei} + E_{hj} = (\varepsilon_{ei} + \varepsilon_F) + (\varepsilon_F - \varepsilon_{hj}) \tag{2-7}$$

For $T > 0$, the excitations are distributed continuously with energy, as is illustrated in Fig. (2.8). It is seen again that a continuum of excitation energies exists above the ground state energy $E = 0$.

Returning now to the theory of electron-phonon interaction, Cooper, in 1956, built upon Frohlich's work by investigating the effects of adding two electrons to a metal at absolute zero. It is assumed artificially that the existing electrons in the metal obey 'normal' Fermi-Dirac statistics, which presents a step-function at absolute zero (Fig. 2.5). If there is an electron phonon interaction, the two electrons can be thought of as scattering each other such that their individual momenta are continually changing with time. At any instant of time, the two electrons can be viewed as having some momentum p_i and p_j. The continual scattering of the two electrons can be thought of as being composed of a collection of such scattering cases (or "events") under the constraint that the total momentum is constant. Cooper showed that potential energy is minimized for the system with the greatest number of permitted scattering combinations, i.e. the total number of possible (p_i,p_j) combinations. If the electrons with equal but opposite momentum are paired, then the maximum number of allowed scattering pair states are available, such that the system energy is minimized. The pairing of two electrons, $p_i\uparrow$ and $-p_i\downarrow$ (where "$\uparrow$" denotes spin up) is now known as a Cooper

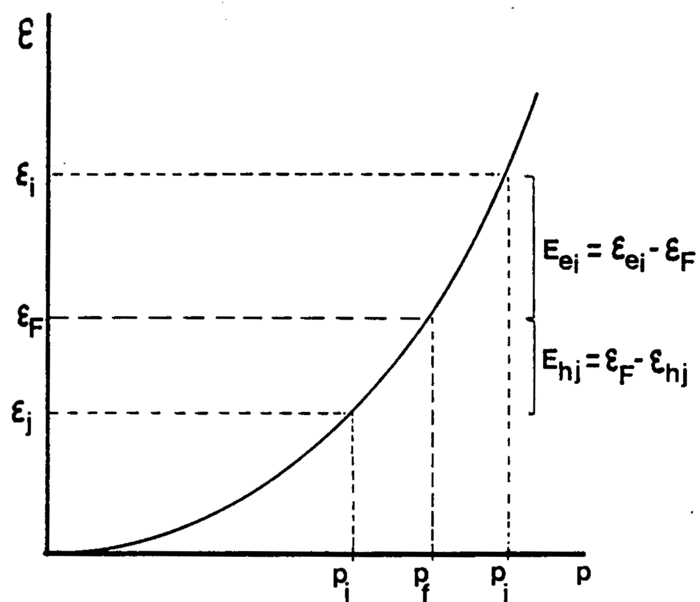

Figure 2.7

Excitation energies defined in terms of Bloch state energies

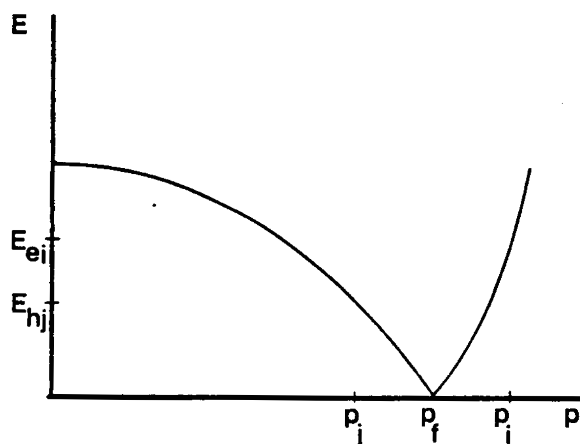

Figure 2.8

Normal metal excitation energies

pair. Cooper showed that this type of pairing yields the largest decrease of potential energy. If two electrons, which previously were in normal states made a transition to such a scattering state, then the decreased potential energy would offset the increased kinetic energy such that the total energy of the system would decrease.

A single electron can be represented by a quantum mechanical waveform $\psi(r,p)$,where $\psi^*\psi$ describes the probability that the electron has momentum p and is located at position r. The probability function for two uncorrelated electrons with momenta p_i and p_j and position r is described by the wavefunction

$$\phi'(r,p_i,p_j) = \psi(r,p_i)\psi(r,p_j) \qquad (2\text{-}8)$$

The Cooper pair state, which consists of two paired electrons in a mixture of wavefunctions with equal and opposite momenta, is described by the wavefunction Φ' where

$$\Phi(r) = \sum_{ij} a_{ij}\phi(r,p_i\uparrow,-p_i\downarrow), \qquad (2\text{-}9)$$

If the system energy is lowered by the formation of one pair, then it would seem logical for many electrons to make the transition. The probability of finding a given pair state $(p_j\uparrow,-p_j\downarrow)$ empty at any given time decreases as more Cooper pairs are formed with $p > p_f$. Open momentum states become increasingly unavailable to the Cooper pairs for occupation. Since reduction of system energy is a function

of the number of scattering processes available (i.e. the number of possible $(p_i, -p_i)$ states available for the next scattering event per electron pair), there exists a tradeoff between increased kinetic energy and reduced potential energy. There is therefore a limit to system energy reduction by forming Cooper pairs with $p > p_f$.

In 1957 Bardeen, Cooper and Schrieffer developed a theory of superconductivity which addressed this question of many pair interaction [7]. The crucial assumption of the"BCS" theory is that pairs influence each other only by making unavailable, for the next scattering event of the other pairs, the momentum states which they are occupying. In the BCS theory, at absolute zero all the conduction electrons form Cooper pairs with the wavefunction Φ given by eqn. (2-9). These pairs are described by Bose-Einstein statistics and exist at one energy value in the same quantum state. Some of these pairs form with $p > p_f$ as described earlier such that the system energy is lowered. The probability h_i^2, that a two electron state $(p_i\uparrow, -p_i\downarrow$ is occupied, is given by

$$h_i^2 = \frac{1}{2}\left[1 - \frac{\varepsilon_i - \varepsilon_F}{((\varepsilon_i - \varepsilon_F)^2 + \Delta^2)^{1/2}}\right] \qquad (2.10)$$

where $\varepsilon_i = (p_i^2/2m)$, and Δ is given quantitatively by

$$\Delta(T) = (0)\tanh\left[\frac{\Delta(T)}{\Delta(0)}\right]\frac{T_c}{T} \qquad (2\text{-}11)$$

Figure 2.9 shows the probability h_i^2 that the double-electron state is occupied as a function of momentum at T = 0. The superconducting state has the unusual property of possessing vacancies below p_f and occupied states above p_f for the T = 0 case, unlike a normal metal.

From BCS theory, the energy necessary to break apart a Cooper pair is given by

$$E_b = ((\varepsilon_i - \varepsilon_F)^2 + \Delta^2)^{1/2} + ((\varepsilon_h - \varepsilon_F)^2 + \Delta^2)^{1/2} \qquad (2\text{-}12)$$

where ε_e and ε_h are Bloch state energies above and below ε_F respectively, as defined earlier. The theory therefore predicts a gap of 2Δ in the excitation energy of the superconductor, centered about the fermi energy. This energy gap, as noted above, was seen experimentally in specific heat and absorption studies but could not be explained with the simple two-fluid model. The separation of a Cooper pair $(p_i\uparrow, -p_i\downarrow)$ implies that the electrons no longer form that pair with equal and opposite momentum. If an excitation to momentum state $p_i\uparrow$ occurs, then its Cooper pair partner is absent from state $-p_i\downarrow$. These excitations (called "quasiparticles") no longer participate in the scattering interactions - they act almost like free electrons. The splitting of the Cooper pair increases the potential energy of the system by its binding energy. With an excitation in momentum state $p_i\uparrow$ but the state $-p_i\downarrow$ empty, the pair state

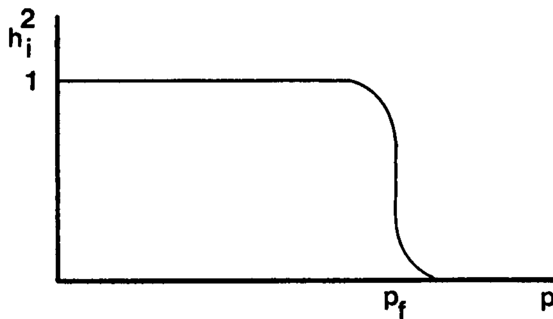

Figure 2.9

Probability that the double-electron state is occupied

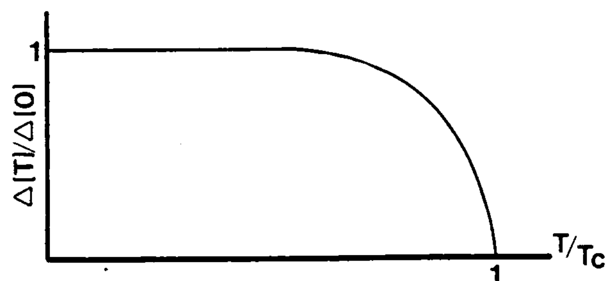

Figure 2.10

Superconductor energy gap dependence on temperature

$(p_i\uparrow, -p_i\downarrow)$ is unavailable to the other pairs for occupation in the next scattering event. The energy of each electron pair in the total system is therefore raised. These two energetic effects cause the noted gap in the excitation spectrum. As the temperature is raised and quasiparticles are created, the decrease in scattering interactions yields a decrease in the energy gap as shown in Fig. 2-10. The gap energy continues to decrease as the temperature is raised until the critical temperature is reached and $\Delta = 0$. It is important to note that Δ does not substantially decrease until the temperature is raised above $T_c/2$.

The excited electrons are named quasiparticles because of the unusual properties of these states. Consider again Fig. 2.11 which shows h_i^2, the probability that the double-electron state is occupied. If a quasiparticle is excited with momentum p_i, then the state $-p_i$ is empty. If p_i is much greater than p_f, then the excitation exists in the state p_i, which previously had a very small probability for occupancy ($h_i^2 << 1$). The electron therefore exists in a state which was previously unoccupied, such that the quasiparticle acts like an electron (and is called a quasielectron). Similarly, if p_j is much less than p_f, then the excitation exists in the state p_j, which previously had a very large probability for occupancy ($h_i^2 >> 1$). The electron therefore exists in a state which was previously occupied. The corresponding state $-p_j$, which previously was occupied is now unoccupied, such

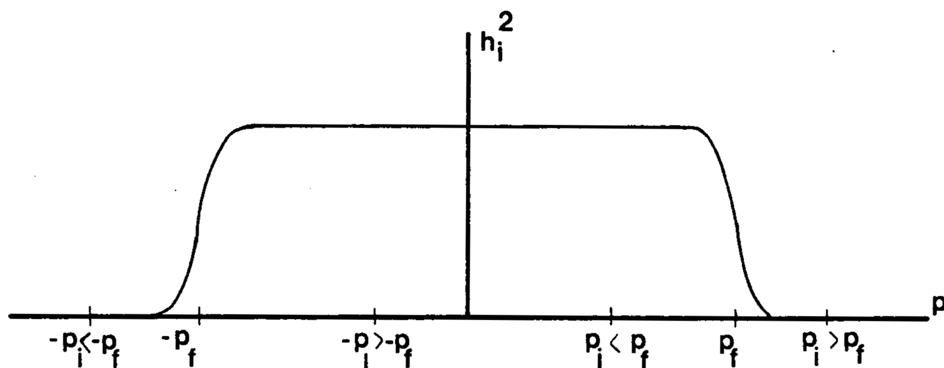

Figure 2.11

Probability of pair occupancy in the superconducting state

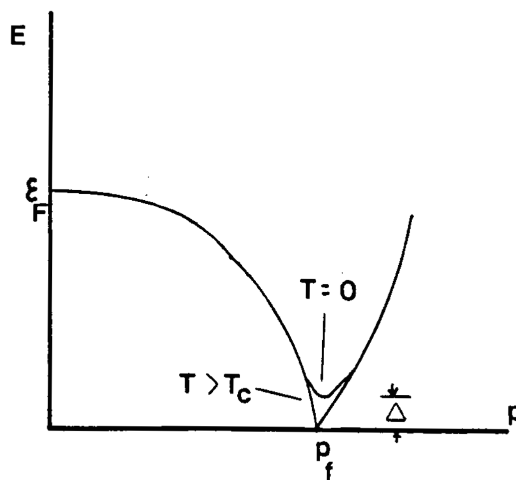

Figure 2.12

Permitted excitation energies for a superconductor with energy gap Δ

that the excitation acts like a hole (and is called a quasihole). If p_i is near p_f, such that h_i^2 is a fraction of unity, then the quasiparticle cannot be regarded totally like an electron or a hole. Instead the quasiparticle acts as a mixture of both.

The permitted excitation energies (E) versus crystal momentum, as given by BCS theory, are shown in Fig. 2.12 for $T = 0$ and $T > T_c$. Away from p_f, the E versus P diagrams for the superconductor and the normal case are equivalent. Note the gap in the excitation energy of energy Δ for the $T = 0$ case. In contrast to the normal metal case, excitations can only occur in the superconductor case for energies larger than Δ.

Earlier in this chapter, the density-of-Bloch-states for a normal metal was given. In order to analyze the tunneling phenomena of quasiparticles in a SIS junction, the density-of-excitation-states must also be known. For the case of a normal metal, it is evident from Figs. 2.7 and 2.8 that, for every value of p, there exists a corresponding Bloch energy and a corresponding excitation energy. For the Bloch states, in an incremental interval of momentum dp, there is a corresponding range of Bloch state energies $d\varepsilon$. For the excitation states, in this same interval of momentum dp, there is a corresponding range of excitation energies dE. These two cases are shown in Fig. 2.13. Since the number of Bloch states and excitation states in this interval dp, are equal, the number of states in $d\varepsilon$ equals the number of states

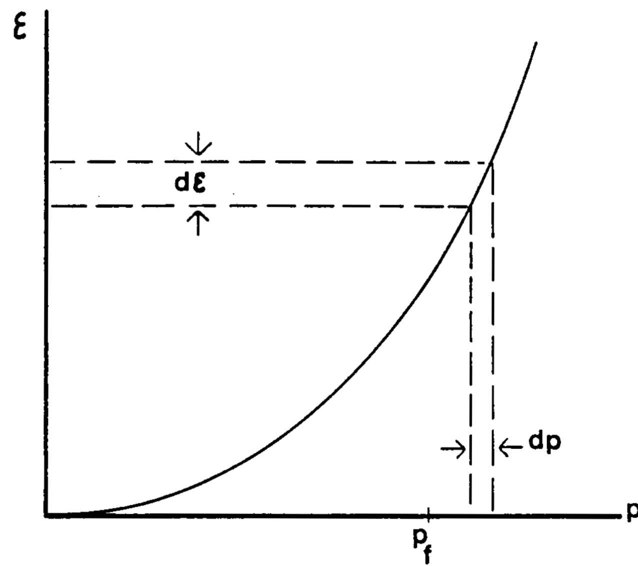

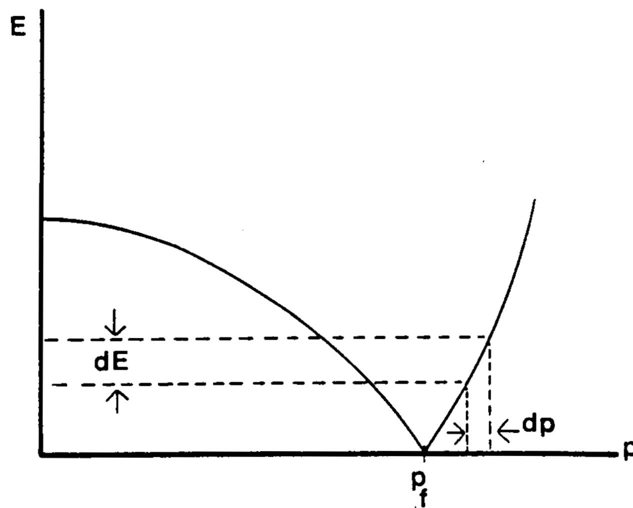

Figure 2.13

Graphical construction of dε and dE for an incremental interval of momentum dp

in dE. The density-of-normal-excitation-states, $N_n(E)$, is therefore given by

$$N_n(E)dE = N_n(\varepsilon)d\varepsilon. \qquad (2\text{-}13)$$

For the normal metal, the excitation energy is just $E = |\varepsilon - \varepsilon_F|$, as discussed above, such that $dE = d\varepsilon$ and the density of excitations for a normal metal, $N_n(E)$, is simply equal to $N_n(\varepsilon)$, the density-of-Bloch-states. Though the approach for deriving the density-of-excitation-states-function of the superconductor is simlar, the resulting function will be shown to be quite different.

The derivation of the density-of-excitation-states for a superconductor will now be examined. From Fig. 2.8, it is evident for the superconductor that for every value of p there exists an excitation state such that (2-13) is modified to

$$N_s(E)dE = N_n(\varepsilon)d\ . \qquad (2\text{-}14)$$

Because there exists a gap about the Fermi level in the excitation energy, the simple relationship $d\varepsilon/dE = 1$ does not hold for the superconductor. In fact, the value of the density-of-superconducting-excitation-states is expected to be equal to zero for $E < \Delta$. However, far above or below p_f, the E versus p diagrams for the superconductor and the normal case are equivalent such that the superconducting density-of-states $N_s(E)$ is identical to that of a normal metal $N_n(E)$. Near the energy gap of the superconductor,

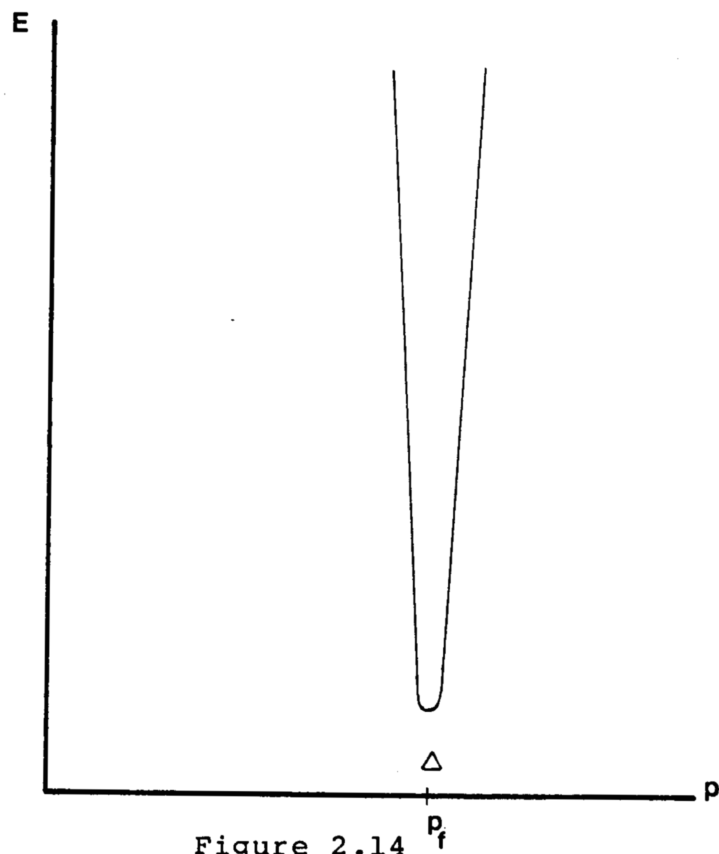

Figure 2.14

Expanded view of the superconductor excitation energy

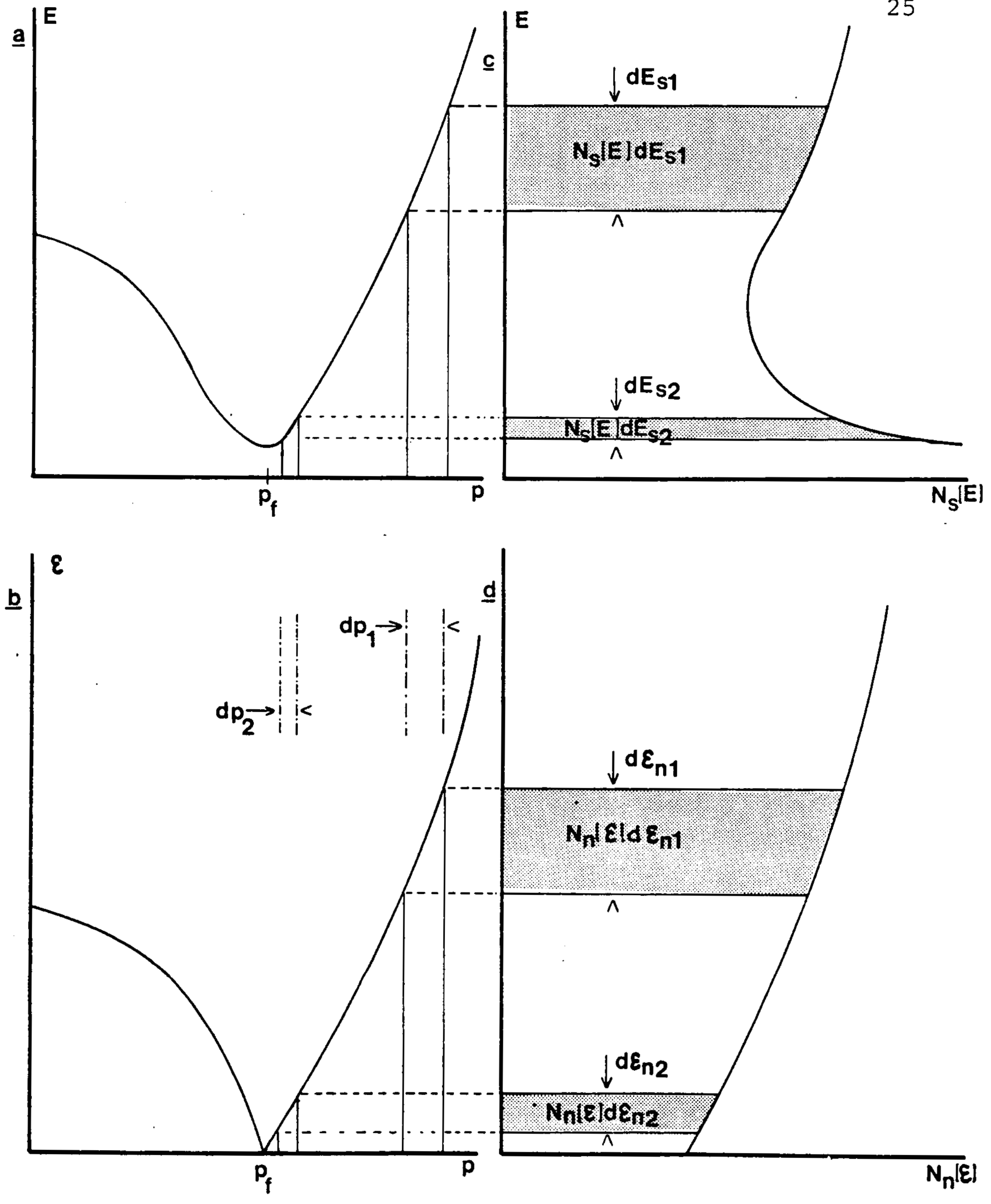

Figure 2.15 Graphical analysis of $N_s(E)$

however, $N_s(E)$ will be quite different from $N_n(E)$.

The form of $N_s(E)$ will now be illustrated graphically. In Fig. 2.14, an expanded view of the superconductor excitation energy near p_f is shown. Since the energy gap has such a relatively small value, when we expand the energy axis to show Δ graphically, the E versus p curve away from p_f becomes nearly vertical. In order to illustrate the origin of the unusual superconducting density-of-states, the scale of the E versus p diagram for Fig. 2.15a is distorted. Figures 2.15b - 2.15d show ε versus p (normal case), $N_s(E)$ and $N_n(\varepsilon)$ respectively. For momentum values far from p_f, an incremental interval dp_1 is shown to map into a range of normal Bloch state energies ($d\varepsilon_{n1}$) and superconductive excitation energies (dE_{s1}). Since $N_n(\varepsilon)d\varepsilon_{n1} = N_s(E)dE_{s1}$, the density-of-excitation-states for the superconductor can be constructed graphically, as $N_n(E)$ is shown. From Fig. 2.15d, the shaded area, under the known density-of-states curve of the normal metal for the $d\varepsilon_{n1}$ interval, represents the number of normal states for this interval and is denoted $N_n(\varepsilon)d\varepsilon_{n1}$. In Fig. 2.15c, $N_s(E)$ (corresponding to the dE_{s1} mapping) is constructed such that the shaded area $N_s(E)dE_{s1}$ is equal to $N_n(\varepsilon)d\varepsilon_{n1}$. Since the chosen momentum interval dp_1 is not close to p_f, the density-of-excitation-states construction for the superconductor is similar to the normal case as seen in Figs. 2.15c and 2.15d. If another momentum interval (dp_2) closer to p_f is chosen, the energy gap will strongly alter

the density-of-states function for the superconductor. Due to the decreasing slope of the E versus p superconductor curve, dp_2 intersects a superconductor excitation interval dE_{s2} which is much smaller than $d\varepsilon_{n2}$. In order to construct a $N_s(E)dE_{s2}$ equal to $N_n(\varepsilon)d\varepsilon_{n2}$, the superconductor density-of-states must increase greatly with respect to the normal function. As p approaches p_f, the interval of excitation energies decreases to zero such that the density-of-states function $N_s(E)$ approaches infinity. Note that no excitation states exist in the energy gap; they can be thought of as having been pushed above $E = \Delta$. $N_s(E)$, for $E < E_F$, can be graphically derived in a similar manner. From BSC theory, the excitation density-of-states for a superconductor is given by

$$N_s(E) = \frac{N_n(E)E}{(E^2-\Delta^2)^{1/2}} \tag{2-15}$$

If the undistorted energy scale of Fig. 2.14 is used, then the normal density-of-states curve away from p_f is seen to be nearly constant for tens of energy gaps. For this work the energy range of interest is less than + 10 Δ. $N_n(E)$ can therefore be approximated by $N_n(0)$, such that (2-15) becomes

$$N_s(E) = \frac{N_n(0)E}{(E^2-\Delta^2)^{1/2}} \tag{2-16}$$

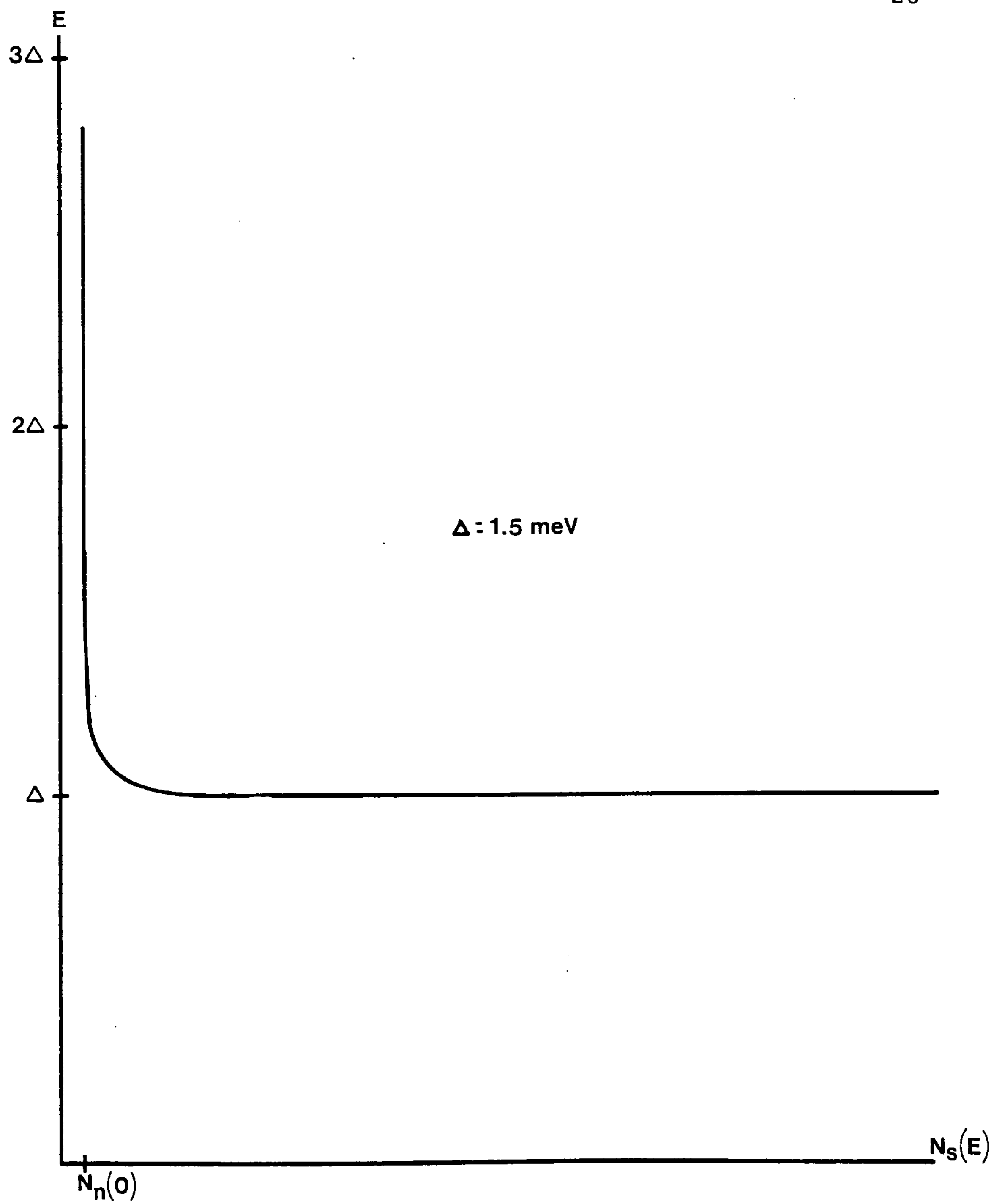

Figure 2.16 Superconductor density of states N_s (E) shown to scale for Δ = 1.5 meV

$N_s(E)$ is shown to scale in Fig. 2.16. In order to show $N_s(E)$ graphically for this work's purposes, the scale will again be distorted as shown in Fig. 2.17. Here the density-of-states is shown in what is known as the "semiconductor" representation, where the excitation energy is positive for both directions from the origin. The top half denotes quasielectron excitation energy and the lower half, quasihole excitation energy.

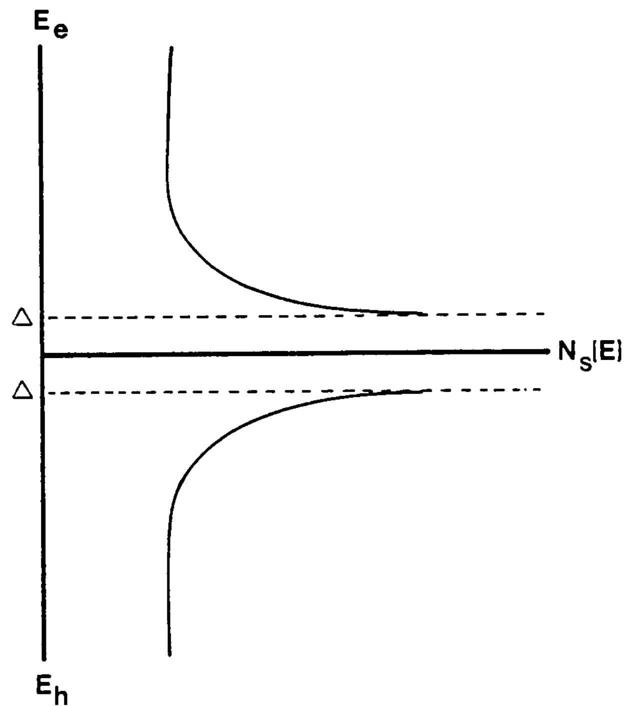

Figure 2.17 Superconductor density of states $N_s(E)$ in the semiconductor representation

CHAPTER III

SIS Tunneling Theory

As an introduction to SIS tunneling theory, the case of normal metals (NIN) will first be examined. For an insulator which presents a relatively larger barrier, the thermal component of current over the potential barrier is negligible. Current transport is due to tunneling through the oxide with a tunneling probability P which can be given by a quantum mechanical analysis of the particular barrier shape. In general, however, P decreases exponentially with barrier thickness and increases linearly with area. The actual characterization of a barrier is often limited to a tunneling resistance which contains P implicitly.

Figure 3.1a is an electron population diagram for a NIN junction at T = 0. As discussed above, since the energy range of interest is on the order of millielectron volts, $N_n(\varepsilon)$ has been taken equal to $N_n(0)$. For T > 0 the electron occupation is therefore described by the Fermi-Dirac distribution f(E), such that the resulting population is given by Fig. 3.1b. Tunneling transitions must of course be made horizontally on these diagrams to conserve energy. The current due to tunneling from left to right in an energy interval dE, is found by simple analysis to be proportional to

$$I_{1\to 2} \propto P[N_1(E-eV)f(E-eV)][N_2(E)(1-f(E))]dE \qquad (3\text{-}1)$$

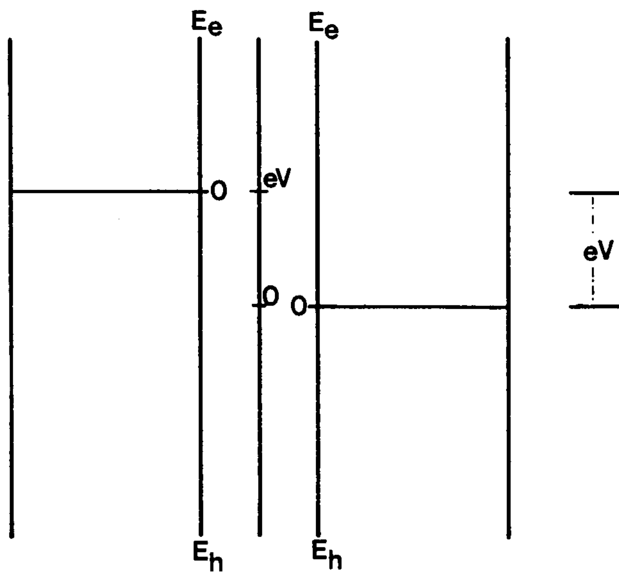

Figure 3.1a Electron population diagram for a normal metal, T=0

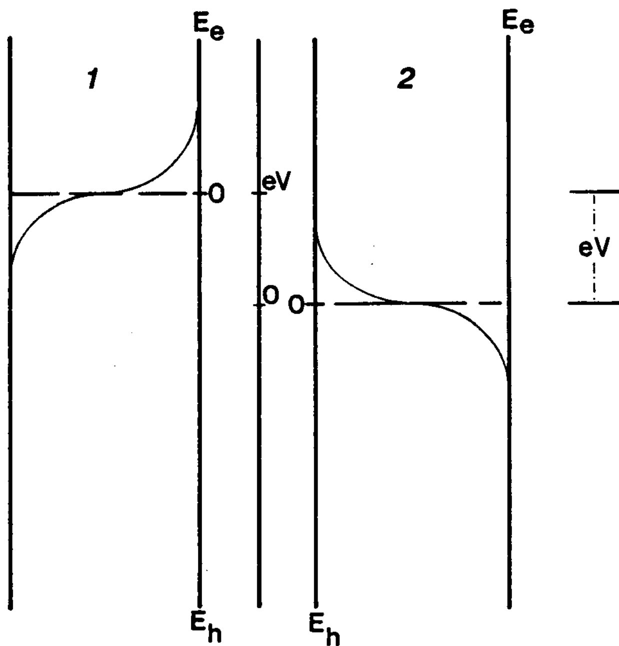

Figure 3.1b Electron population diagram for a normal metal, T > 0

while the current from right to left is proportional to

$$I_{2\to 1} \alpha\ P[N_1(E-eV)(1-f(E-eV)][N_2(E)f(E)]dE. \quad (3-2)$$

The total current is found by integrating over all energies. For the NIN case, the current expression is

$$I = \beta P\ N_1(0)N_2(0) \int_{\text{all } E} (f(E-eV)-f(E))dE \quad (3-3)$$

or

$$I = \beta P\ N_1(0)N_2(0)eV \quad (3-4)$$

where β is a constant which is related to the geometry and the integral has been approximated by eV. Equation (3-4) can be written as

$$I = Gnn\ V, \quad (3-5)$$

where Gnn is the conductance of the ohmic device in the normal state.

Figure 3.2 shows an excitation tunneling diagram for a NIN junction. This form of tunneling diagram will be very useful in understanding the physics of superconductive devices later in this chapter. The NIN case will serve as a simple introduction to the concepts involved. In Fig. 3.2, a negative bias has been applied to the left side (metal one) such that the zero excitation level of metal one is raised by an energy eV relative to metal two. The tunneling of an electron from metal one to metal two is represented by a hole

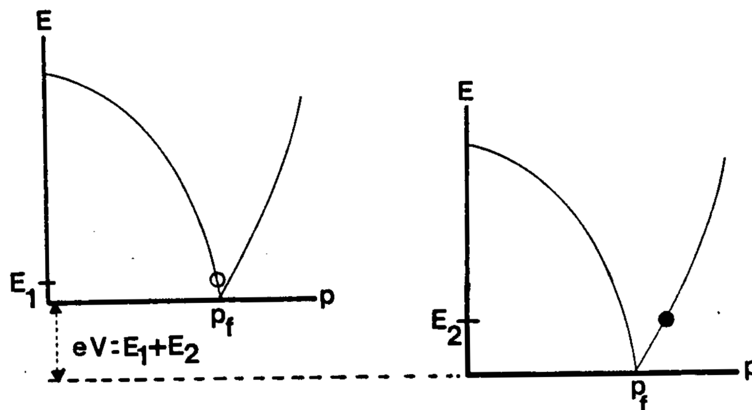

Figure 3.2 Excitation tunneling diagram for a NIN junction

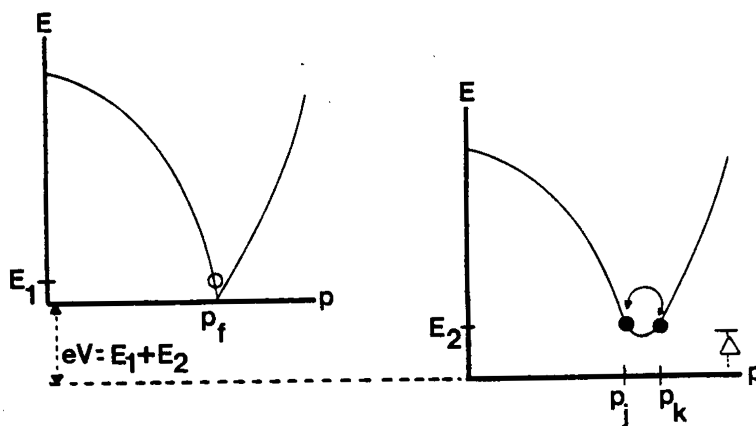

Figure 3.3a Excitation tunneling diagram for a NIS junction

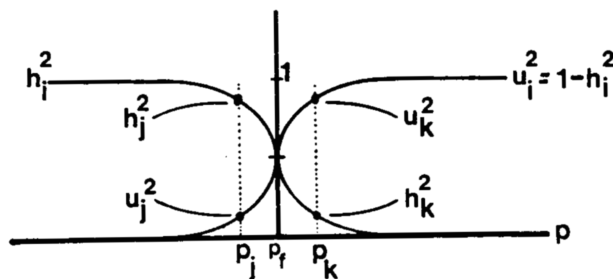

Figure 3.3b Graphical demonstration that $U_j^2+U_k^2 = 1$

excitation ($p < p_f$) of energy E_1 in metal one and an electron excitation ($p > p_f$) of energy E_2 in metal two. The applied bias results in excitation energies such that $E_1 + E_2 = eV$.

The case of a SIN excitation tunneling diagram is shown in Fig. 3.3a, where an electron of energy E_1 can tunnel into state p_j or p_k, both states at energy E_2. For the T = 0 case, the probability that state p_k is empty is given by $u^2{}_k = 1 - h^2{}_k$. Since $h^2{}_i$ has symmetry about p_f it is also evident that $h^2{}_j = 1 - h^2{}_k$ or $u^2{}_k = h^2{}_j$ (Fig.3.3b). Since the sum of the probabilities for occupancy and non occupancy of a given state is unity ($h^2{}_j + u^2{}_j = 1$) it follows that

$$u_j^2 + u_k^2 = 1 \qquad (3\text{-}6)$$

Equation (3-6) reveals that the total probability of a vacant state is unity. Though the electron may actually tunnel into either state p_j or p_k, the current can be conveniently modeled by describing all states below p_F as full and those above p_F as vacant. In this scheme, the electron tunnels into the vacant state p_k. The semiconductor representation for the electron population diagram of a SIN junction at T = 0 is therefore shown in Fig. 3.4. In this representation, electrons tunnel from the normal metal only into states above the energy gap, though physically states both above and below p_f are involved.

Figure 3.5 shows an excitation tunneling diagram for a SIS junction. The representation of states in the superconductor

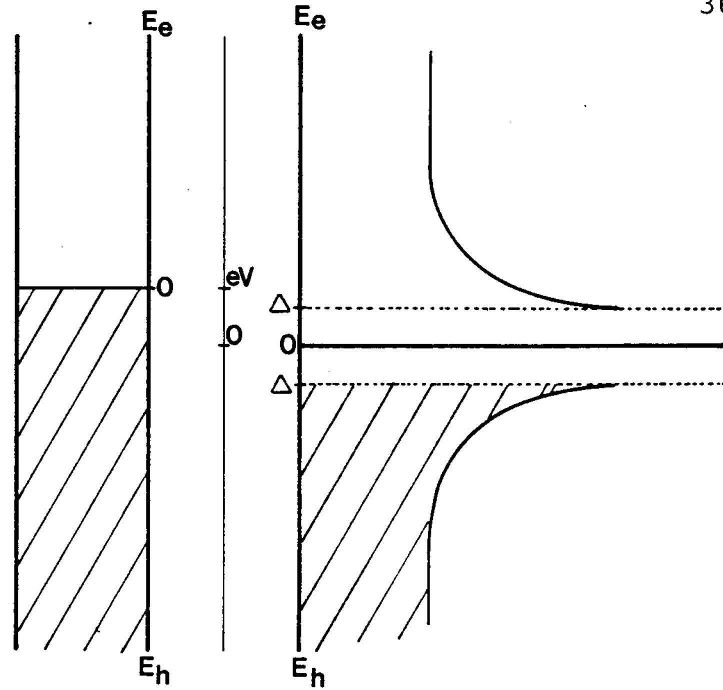

Figure 3.4 Semiconductor representation of a NIS junction for T=0

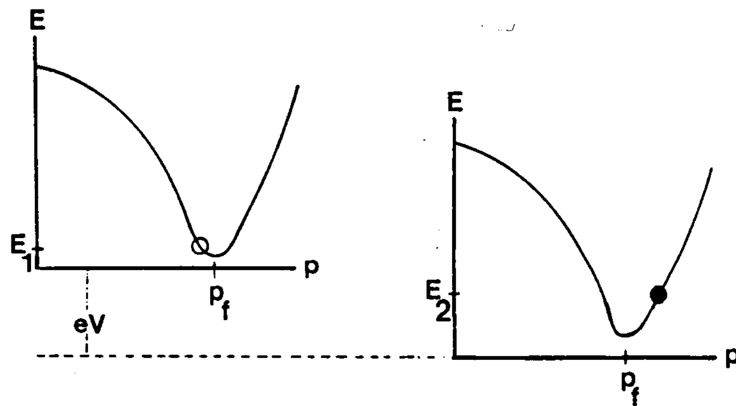

Figure 3.5 Excitation tunneling diagram of a SIS junction

as empty above p_F is used for both superconductors. Ideally, there are two tunneling processes.

In the first case (for T = 0) a Cooper pair may separate into a hole excitation and an electron which subsequently tunnels through the barrier into the other superconductor as an electron excitation. The minimum applied bias for tunneling occurs when the bias is equal to the sum of the two gap energies. This process is shown in Fig. 3.6 (for T = 0) using the semiconductor representation. The second process is the tunneling of an existing excited electron across the junction, occurring for T > 0. The general semiconductor representation of a SIS junction for T > 0 is shown in Fig. 3.7. BCS theory shows that the distribution of single electron states in a superconductor is of the Fermi-Dirac form

$$f(E_p) = \frac{1}{1 + \exp(E_p/kT)} , \qquad (3-7)$$

where E_p is the excitation energy corresponding to momentum state p from Fig. 2.12. The excitations above and below the gap energies in Fig. 3.7 (corresponding to quasiparticle occupation of states about p_F) are therefore distributed according to the Fermi function. The shaded areas (for E_e) can be thought of as potential tunneling electrons and the unshaded areas as open states for tunneling electrons. Alternatively, the shaded areas (for E_h) are empty hole states and the unshaded are are empty electron states.

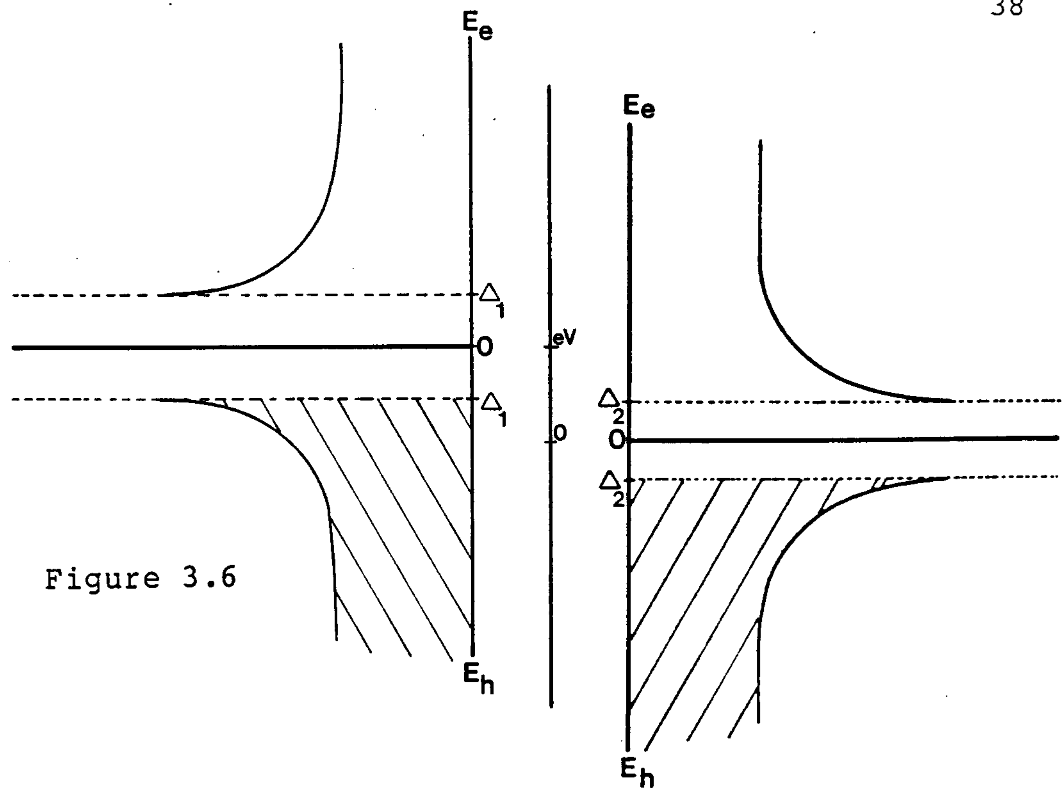

Semiconductor representation of an SIS junction for T=0 with $eV = \Delta_1 + \Delta_2$

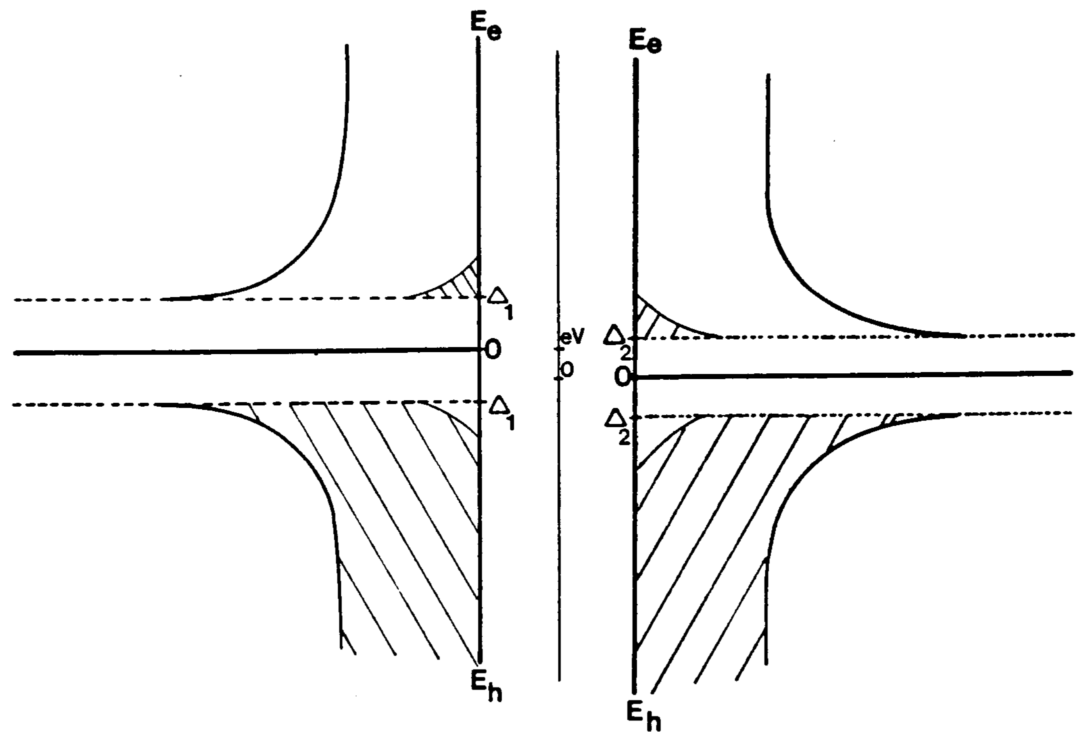

Figure 3.7 Semiconductor representation of a SIS junction for T > 0

Consider first the T = 0 case for two superconductors with gap energies $\Delta 1$ and $\Delta 2$. When a positive bias is applied to metal two, electron tunneling is not permitted until $eV = \Delta 1 + \Delta 2$, as shown graphically in Fig. 3.8. At this potential, the singularities in both density of state functions are aligned such that (with our semiconductor model) the tunneling of electrons from metal one to metal two increases substantially. Since the superconductor density-of-states curve approaches the normal case for energies larger than Δ, the current approaches the normal curve for large biases. The T = 0 I-V curve, for this SIS case, is shown in Fig. 3.9.

The general current expression, analagous to (3-3) is

$$I = \beta P \int N_{s1}(E-eV) N_{s2}(E) \{f(E-eV) - f(E)\} dE. \qquad (3\text{-}8)$$

If eqn. (2-16) is substituted, the expression simplifies to

$$I = \quad N_{s1}(E-eV) N_{s2}(E-eV) \{f(E-eV) - f(E)\} dE \qquad (3\text{-}9)$$

where $N'_{sx}(E)$ is defined as

$$N'_{sx}(E) = \frac{E}{(E^2 - \Delta_x^2)^{1/2}} \qquad (3\text{-}10)$$

Equation (3-9) can be solved directly when T = 0 to give Fig. 3.9; however, the T > 0 case can only be solved numerically.

For the T > 0 case, excited quasiparticle tunneling is permitted through the barrier for biases less than $\Delta_1 + \Delta_2$. When a negative potential is applied to metal one,

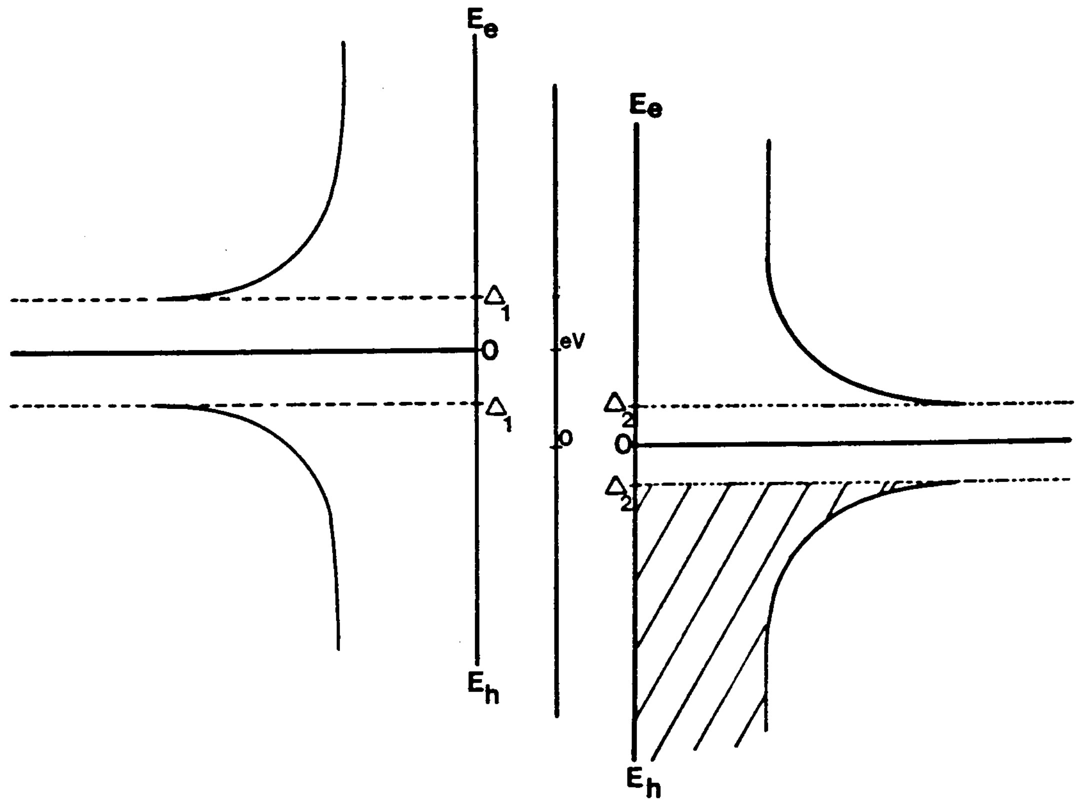

Figure 3.8 Semiconductor representation at T=0 for a positive bias (eV = $\Delta_1 + \Delta_2$) applied to metal two

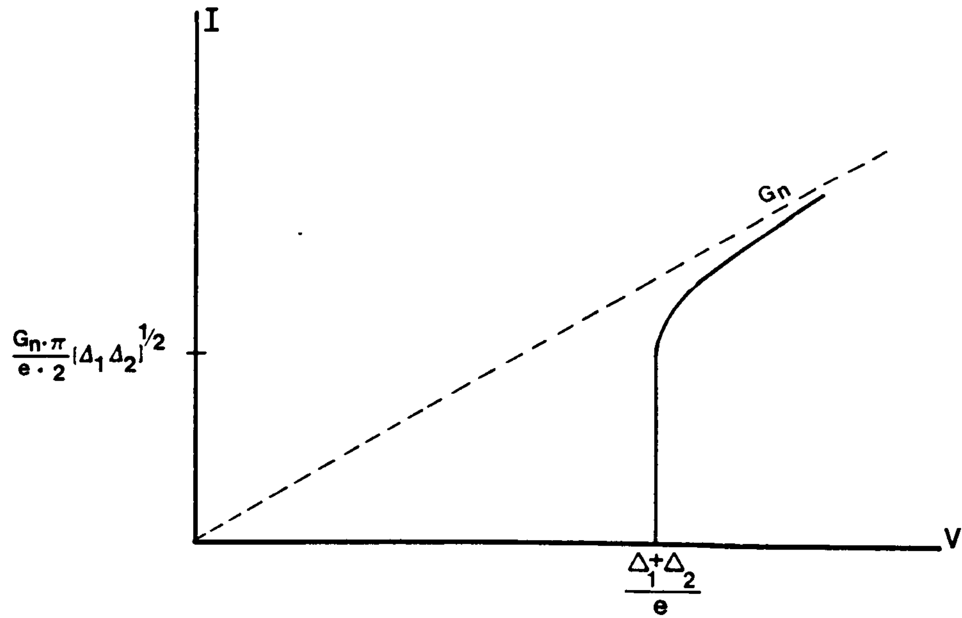

Figure 3.9 SIS I-V curve for T=0

the subgap current will increase until $eV = \Delta_2 - \Delta_1$. At this bias, the upper edges of both energy gaps are aligned as shown in Fig. 3.10. With the semiconductor model, for larger biases, the thermally excited electrons above the gap and holes below the gap tunnel into a decreasingly available density-of-states. The current, therefore, decreases until $eV = \Delta_1 + \Delta_2$, yielding a negative resistance region. With a SIS homojunction, where $\Delta_1 = \Delta_2$, this phenomena does not occur, such that this negative resistance region is peculiar to heterojunctions. For $eV = \Delta_1 + \Delta_2$, the tunneling current, as in the $T = 0$ case, increases substantially and approaches the normal curve for larger biases. A typical $T > 0$ ideal I-V curve is shown in Fig. 3.11.

Though the exact solution of the current equation (3-9) requires a numerical integration, a number of theoretical properties of the I-V structure have been derived from BCS theory. The quasiparticle current discontinuity at $eV = \Delta 1 + \Delta 2$ is given by

$$\Delta I_{ss} = \frac{Gnn}{2e} [\Delta_1 \Delta_2]^{1/2} [1-\exp[-(\Delta_1 + \Delta_2)/kT]] / [1 + \exp(-\Delta_1/kT)][1 + \exp(-\Delta_2/kT)] \quad (3-11)$$

For temperatures below $T_c/2$, such that the energy gap has nearly obtained a $\Delta(0)$ value, ΔI_{ss} can be approximated by

$$\Delta I_{ss} = \frac{Gnn\pi}{2e} [\Delta_1 \Delta_2]^{1/2} \quad (3-12)$$

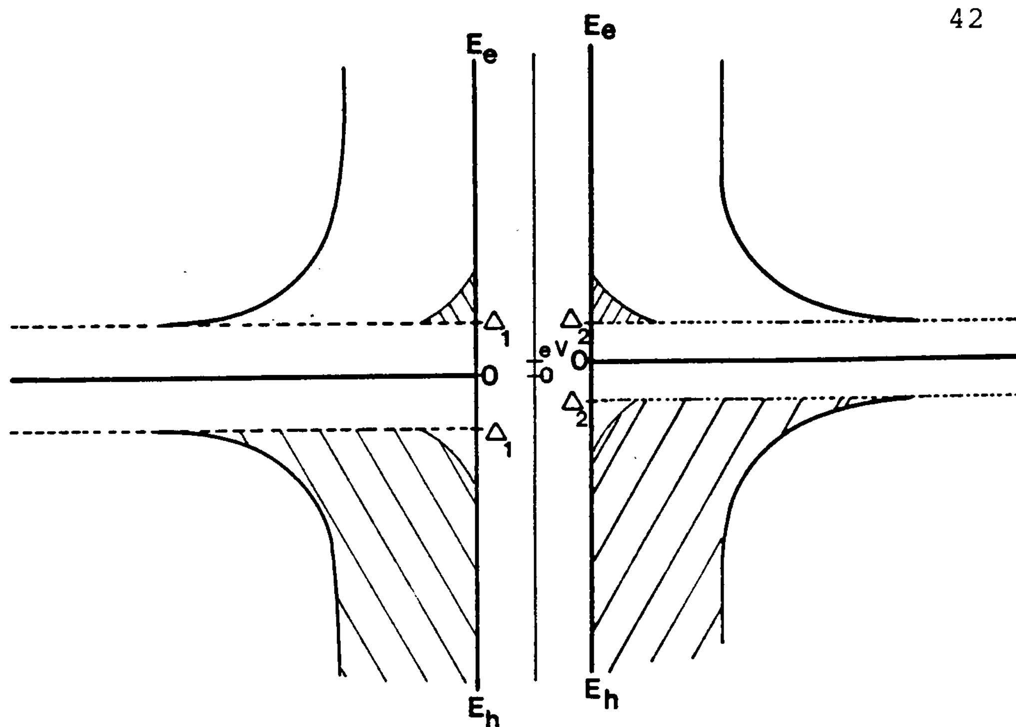

Figure 3.10 Semiconductor model, $T > 0$, $eV = \Delta_2 - \Delta_1$

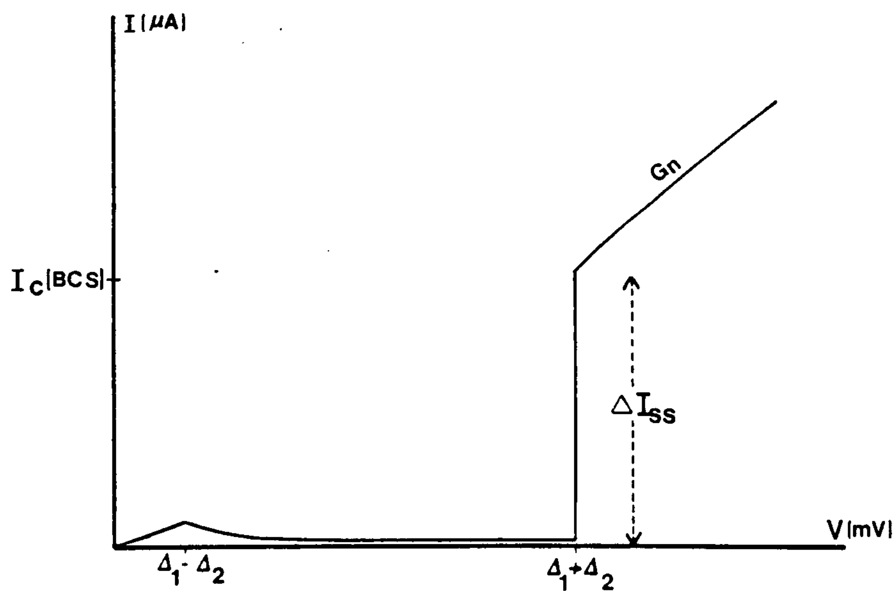

Figure 3.11 Typical ideal I-V curve for an SIS junction $\Delta_1 \neq \Delta_2$, $T > 0$

In addition to quasiparticle tunneling, pair tunneling can occur in a SIS junction. Pair tunneling can be described by the Josephson equations

$$I = I_c \sin \phi \tag{3-13}$$

and

$$\frac{d\phi}{dt} = 2 \frac{eV}{\hbar} \tag{3-14}$$

where ϕ is the phase difference across the junction of the two pair wavefunctions. Two separate phenomena, the dc and ac Josephson effect, are described by these equations. The ac effect occurs when ϕ changes at a constant rate in proportion to the applied voltage. This results in an alternating current at the frequency $2 \frac{e}{h} V_{dc}$. The dc effect occurs when ϕ is constant such that pairs can tunnel through the barrier even though the voltage across the junction is zero. When the critical current (I_c) is exceeded, a voltage develops across the junction and ϕ begins to change.

The dc Josephson critical current is often suppressed by stray magnetic fields and unwanted noise. The low temperature form of I_c, derived from BCS theory, is

$$I_c = \frac{\pi}{eR_n} \frac{\Delta_1 \Delta_2}{\Delta_1 + \Delta_2} \tag{3-15}$$

With eqn. (3-12), the ratio of the critical current to quasiparticle current jump is found to be

$$\frac{I_c}{\Delta I_{ss}} = \frac{2\sqrt{\Delta_1 \Delta_2}}{\Delta_1 + \Delta_2} \tag{3-16}$$

such that the ratio is theoretically less than one, except for the $\Delta_1 = \Delta_2$ case. If Ic is suppressed, the value can theoretically be obtained from ΔI_{ss} and eqn. (3-16).

Figure 3.12 shows a theoretical I-V curve for two electrodes (Δ(Nb) = 1.44 mV and Δ(PbBi) = 1.7 mV) which are used in this work. With these materials, the quasiparticle current jump ΔI_{ss} = 49.15 μA is theoretically only slightly larger than the critical current I_c = 48.98 μA, for R_n = 50 Ω.

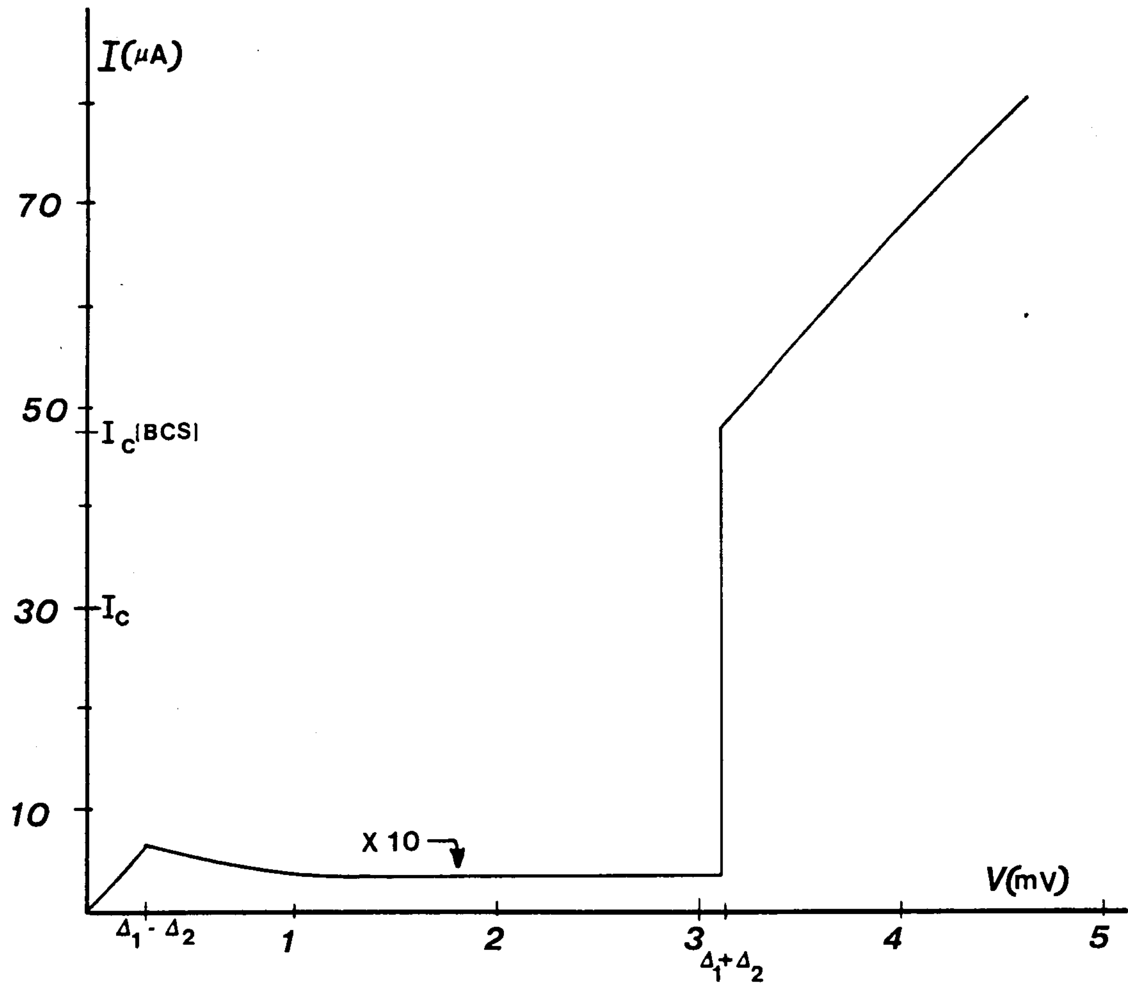

Figure 3.12 Theoretical I-V curve for an SIS junction $\Delta_1 = 1.44$ meV, $\Delta_2 = 1.7$ meV

CHAPTER IV

Theoretical Modeling

This work is focused on developing an optimal fabrication technology to produce high quality SIS junctions for mixer applications. In this chapter, the mixing requirements on junction parameters are stated and the theoretical modeling of these parameters is subsequently developed. The pair of electrodes utilized in this work (Nb/PbBi) are examined.

Ideally, the I-V curve of an SIS mixer should look like that of a switch - the subgap current below $V = \Delta_1 + \Delta_2$ should be small and the quasiparticle current jump should be abrupt. Unfortunately, the ideal SIS I-V characteristics (Fig. 3.11) are usually altered by numerous nonideal effects. For real devices, the subgap current is found to be higher and the current jump less abrupt than theoretically predicted. These effects will be discussed later in this chapter.

The abrupt nonlinearity of the SIS quasiparticle current causes an unusual effect in the mixing process. While the D.C. nonlinearity ideally occurs over a small percentage of a millivolt, the voltage equivalent of the photon energy at 115 GHz is 0.475 mV. Unlike the case of Schottky mixers at this frequency, an application of L.O. power will "significantly" add to the D.C. bias due to the phenomena of photon assisted tunnelling. The effective excitation energies are modulated by the applied L.O. field. This phenomena is illustrated

(for the T=0 case) in Fig. 4.1b with a semiconductor diagram. In this diagram three cases are illustrated: no L.O. field, photon absorption and photon emission. With no application of a L.O. field, it is seen that an applied bias of $(\Delta_1 + \Delta_2)/e$ is necessary for current flow. For the second case, however, the excitation energy of electrons, which have absorbed photons of frequency V_{LO}, has increased by $h\omega_{LO}$. The associated energy levels in the semiconductor diagram have been shifted by $h\omega$. It is seen that a smaller applied bias of $(\Delta_1 + \Delta_2 - \hbar\omega)/e$ is therefore required for current flow. For the third case, the excitation energies of electrons, which have emitted photon of frequency V_{LO}, have decreased by $\hbar\omega_{LO}$. It is seen that a larger bias of $(\Delta_1 + \Delta_2 + \hbar\omega)/e$ is therefore required for current flow.

The pumped I-V curve can therefore be thought of as a superposition of unpumped I-V curves, each one shifted on the voltage axis by an integer number of photon step increments (of voltage $\hbar\omega/e$). A typical SIS I-V curve with and without L.O. bias is shown in Fig. 4.1b.

If the instantaneous voltage is driven below a certain voltage (called the dropback voltage, V_d) the voltage across the junction drops to zero. The critical current of the junction must then be surpassed before the device can return to its quasiparticle branch.

This Josephson effect noise must be avoided in SIS mixers; i.e., the D.C. bias should exceed $V_d + V_{LO}$. However,

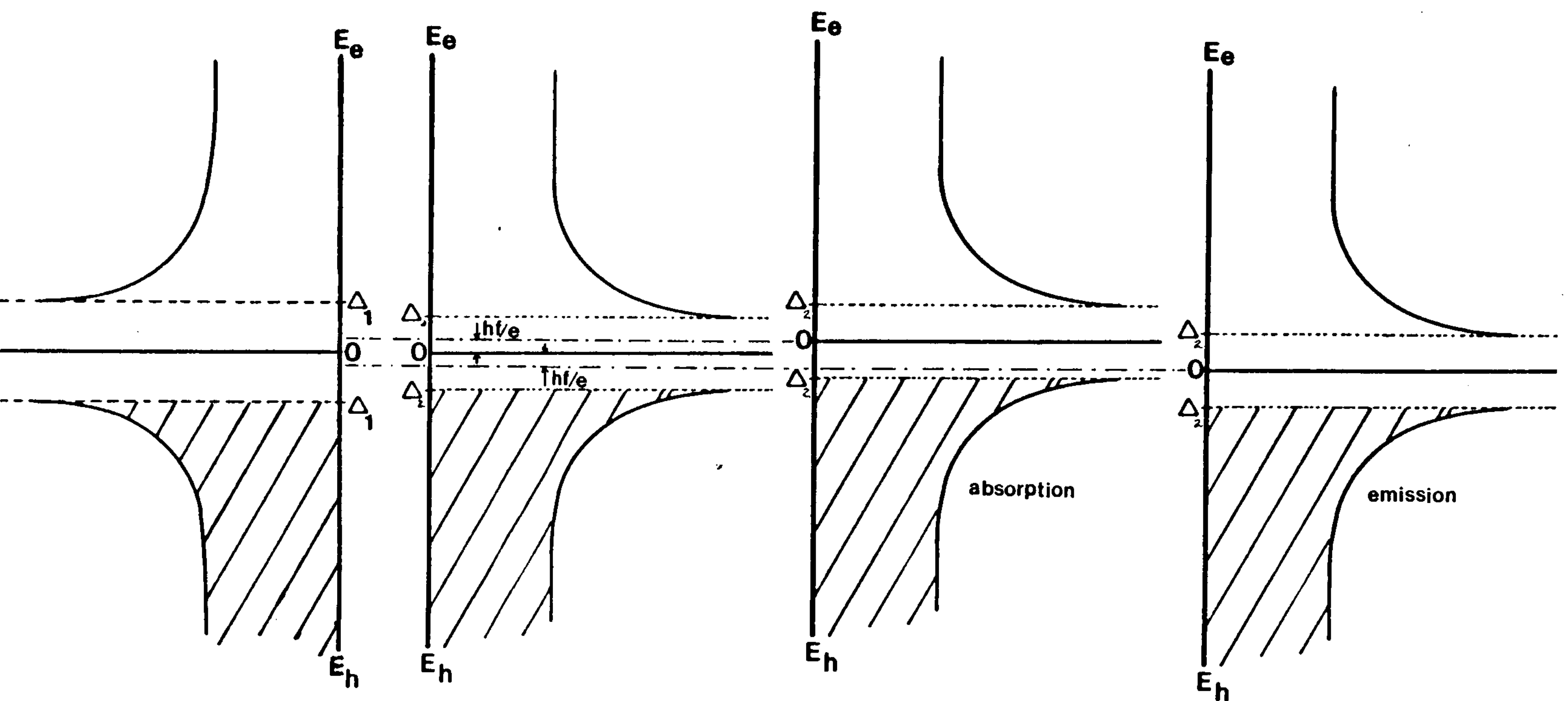

Figure 4.1a

Semiconductor representation of photon emission and absorption.

Figure 4.1b Typical SIS I-V curve with and without L.O. bias

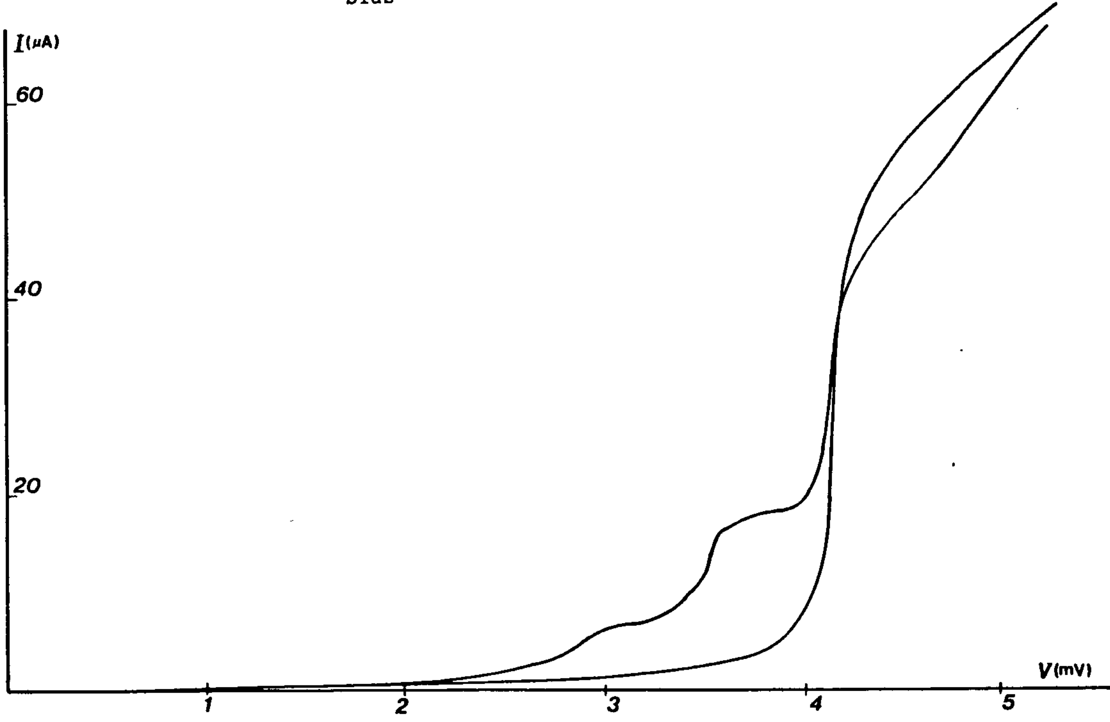

the optimum D.C. bias is approximately $V_{dc} \approx V_g - \hbar\omega/2e$ while the optimum L.O. voltage is $V_{LO} = \hbar\omega\alpha/e$ (where α should be relatively constant) [9]. The condition for avoiding this Josephson effect noise, therefore, becomes

$$V_{gap} - V_d \geq \frac{h\omega}{e} (\alpha + \frac{1}{2}) \tag{4-1}$$

With a Josephson effect analysis, the dropback voltage is found to be proportional to [10]

$$V_d \propto \left(\frac{\omega}{\omega R_n C}\right)^{1/2} \tag{4-2}$$

In contrast to the case of Schottky diodes, a RC cutoff frequency does not exist for the superconductive device. Capacitance is in fact desirable for SIS mixer operation in order to provide a lossless termination for the undesirable upper sidebands. If the device capacitance is too large, however, the signal bandwidth is reduced and optimal R.F. tuning is complicated. A value of Q=4 ($Q \approx \omega R_n C$) has been demonstrated by Feldman [11] and Kerr [12] to be an effective compromise where a normal resistance of $R_n \approx 50\ \Omega$ is typically chosen as a compromise between RF and IF matching requirements.

Since $Q \approx 4$, from eqn. (4-2) it is seen that the dropback voltage is proportional to $\omega^{1/2}$. There is, therefore, a maximum frequency of operation for which the inequality of eqn. (4-1) is obeyed. The upper frequency limit of an SIS

mixer with $V_g \approx 3$ mV has been numerically estimated to be [13] 300 GHz.

This upper frequency estimation is not, however, an absolute limit. A number of different techniques exist for supressing the Josephson critical current and reducing V_d. [14,15] The potential for the use of Josephson effect mixers [16] at higher frequencies has also been largely unexplored.

For a given set of electrode and barrier materials, there are two physical variables to be chosen - barrier width and area. The junction capacitance and normal state resistance R_n are set by a choice of these variables. A value of Q = 4 results in a capacitance

$$C = \frac{6.366 \times 10^5}{f\ R_n}\ \text{fF}/(\text{GHz} - \Omega)\,. \qquad (4\text{-}3)$$

For $R_n = 50\ \Omega$ and f = 115 GHz, the desired junction capacitance is 111 ff.

Experimental optimization of a given SIS device design requires a method for obtaining a value for the R_nC product. Experimentally, R_n is relatively easy to determine, however, the measurement of capacitance can be quite involved and difficult. If the tunneling barrier thickness, area and dielectric constant are known, then the desired capacitance can be calculated from

$$C = \frac{\varepsilon_r \varepsilon_o A}{d}\,, \qquad (4\text{-}4)$$

where ε_r is the barrier dielectric constant. However, the barrier thickness is very difficult to measure. A value for C, however, can be obtained indirectly from the critical current. Since R_n increases exponentially with d, and with eqn. (3-15), J_c can be written as

$$J_c = J_o \, e^{-Kd} \qquad (4\text{-}5)$$

where K is a material tunneling constant. With eqn. (4-4), eqn. (4-5) can be rewritten as

$$C_A^{-1} = \left(\frac{A}{C}\right) = \left(\frac{\ln J_o}{K\varepsilon_r\varepsilon_r}\right) - \left(\frac{1}{K\varepsilon_r\varepsilon_o}\right) \ln J_c \qquad (4\text{-}6)$$

where C_A is the capacitance per unit area of the junction. Experimental results for Nb/PbBi junctions [17] have been used to fit C_A to within approximately 10% for $100 < J_c <$ 5,000 A/cm^2) yielding

$$C_A^{-1} = 10.5 \, \frac{\mu m^2}{pf} - 0.45 \, \frac{\mu m^2}{pf} \ln\left(\frac{J_c}{A/cm^2}\right) \qquad (4\text{-}7)$$

where J_c is the experimentally observed value of the critical current density. With eqn. (4-7), a value for C can be found with a measurement of I_c and A, such that a $\omega R_n C$ product is, therefore, obtained.

The interrelationship between Q, R_n, J_c, C, A and d will now be examined in detail. With eqn. (4-7), K and J_o can be identified such that solving eqn. (4-5) for d yields

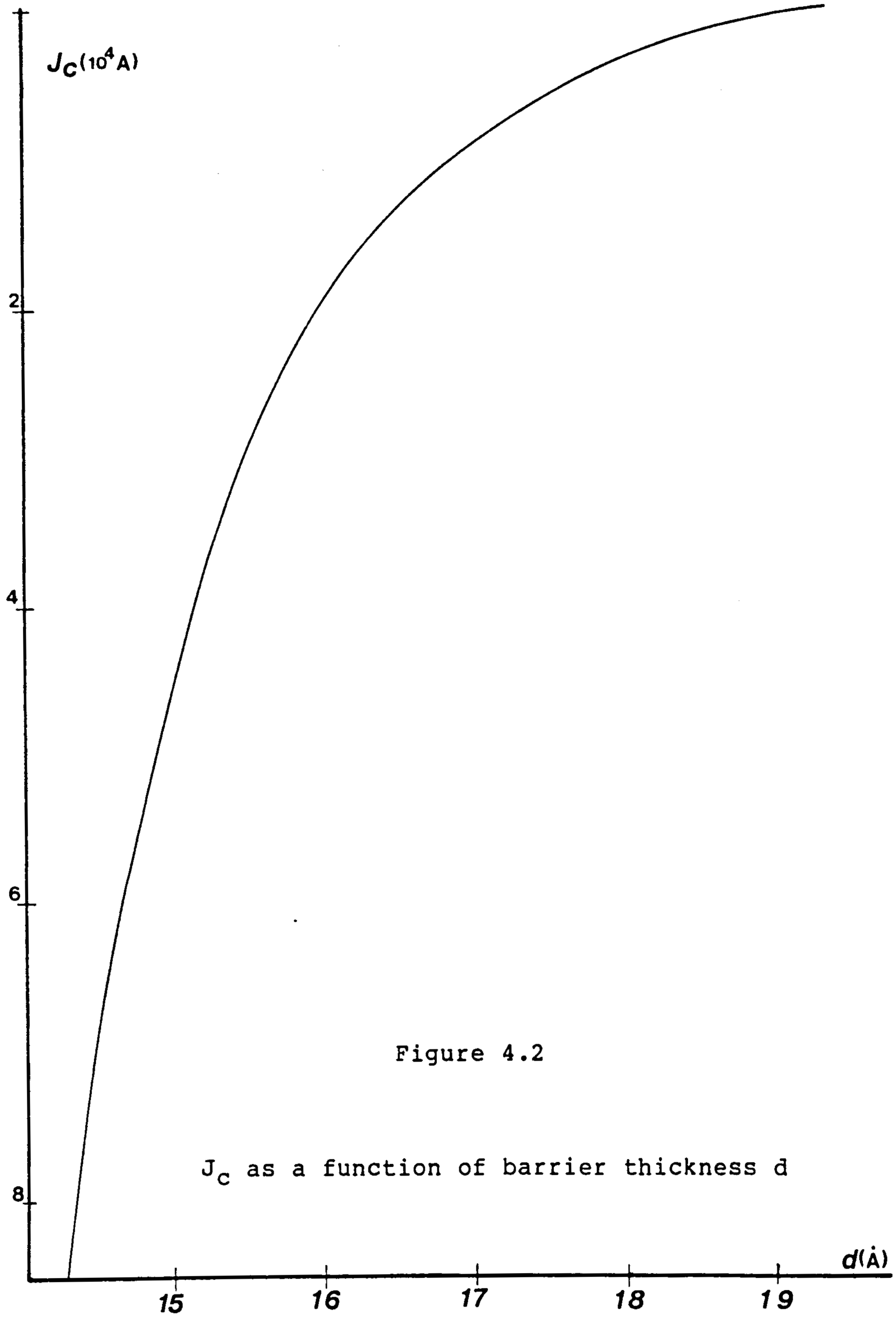

Figure 4.2

J_c as a function of barrier thickness d

$$d = \frac{23.3 - \ln(\frac{J_c}{A\text{-}cm^2})}{8.43 \times 10^3} \ \mu m \qquad (4\text{-}8)$$

J_c as a function of d, for Nb/PbBi junctions is shown in Fig. 4.2 where J_c is seen to depend strongly on d. In order to fabricate devices with a desired J_c value, a tight control on the barrier thickness is required.

It has been shown that the expected BCS value of the critical current must be multiplied by an empirical correction factor (0.64 for Nb/PbBi [18]) to correspond with experimental results. For the experimental measurement of J_c, (3-15) is, therefore, modified to

$$J_c = \frac{0.64\,\pi}{AeR_n} \frac{\Delta_1\Delta_2}{\Delta_1\Delta_2} \qquad (4\text{-}9)$$

If eqn. (4-9) is multiplied with eqn. (4-4), then Q can be written as

$$Q = \frac{\omega\pi(0.64)}{J_c} \frac{\Delta_1\Delta_2}{\Delta_1+\Delta_2} \frac{\varepsilon_r\varepsilon_o}{d} \qquad (4\text{-}10)$$

With eqn. (4-8), it follows that Q and J_c are inversely related. (J_c versus Q is shown in Fig. 4.3). For a choice of J_c (or Q) C can be varied such that from eqn. (4-7) values of A can be calculated and values of R_n finally obtained from eqn. (4-9). With this method, the range of values of the parameters R_n,C,A and J_c (or Q), yielding desirable RF characteristics, can be found. In Fig. 4.4, lines of constant Q and A are shown on a R_n versus C plot for a Nb/PbBi junction.

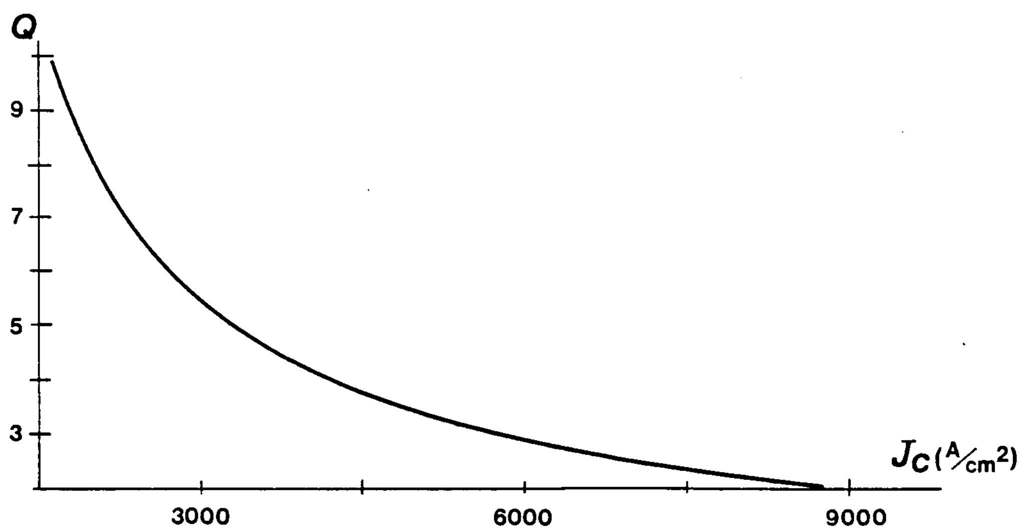

Figure 4.3 J_c versus Q, $(Q = \omega R_n C)$

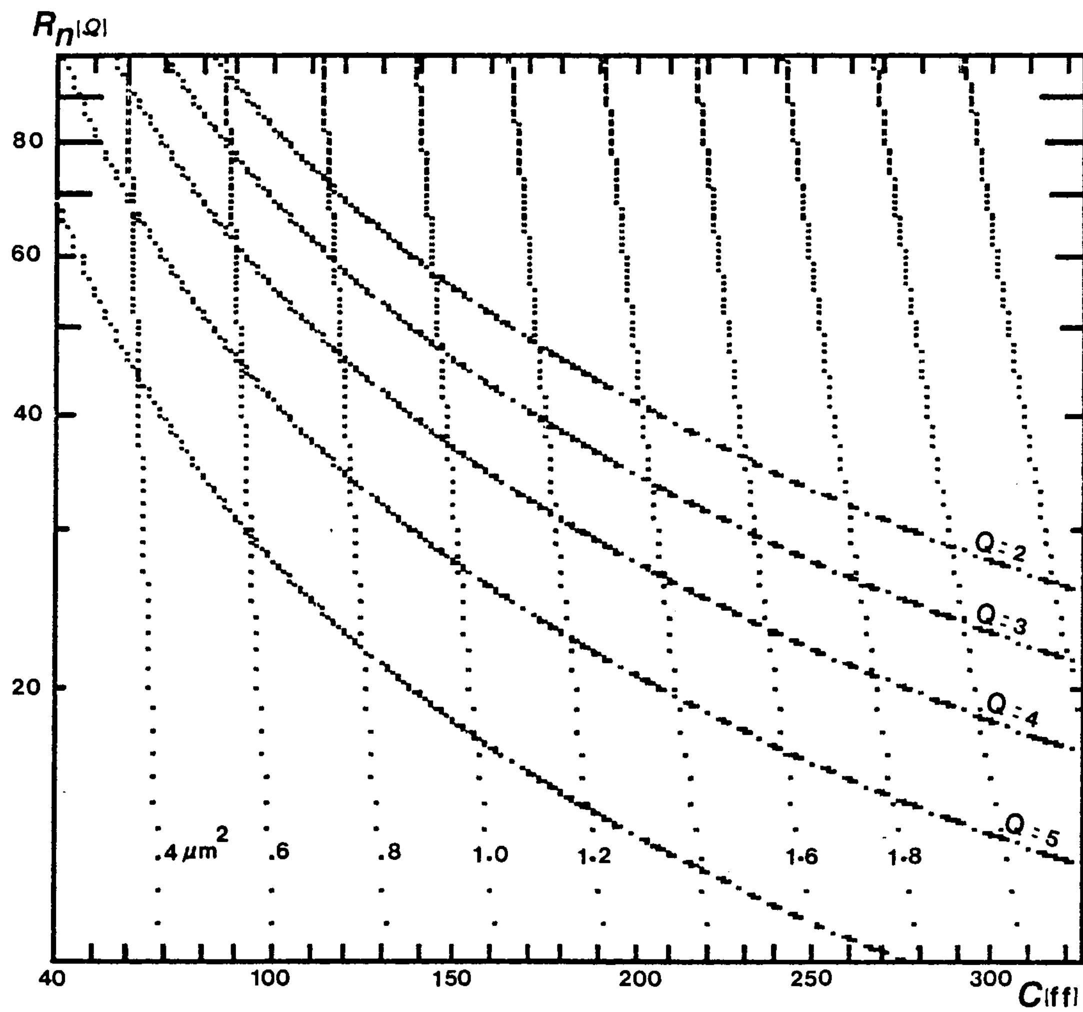

Figure 4.4 Lines of constant Q and A are shown on a R_n versus C plot for a Nb/PbBi junction

Acceptable junction characteristics fall between the Q = 3 and Q = 5 curves for R_n between 30 and 70 ohms. Tabulated values of R_n,C,A and J_c have been listed in Table 4-1. It is seen for a given A, that C is almost constant, decreasing slightly for increasing R and Q. This is understood by noting that a very small increase in barrier thickness will result in a much larger increase of R_n and decrease of J_c values, yet the junction capacitance will decrease only slightly. Further insight can be obtained from Fig. 4.5, where constant R_n curves of 30 and 70 ohms are plotted versus A and C. Again it is seen for a given area, that the capacitance is a weak function of normal resistance.

Control of the fabrication process, as has been mentioned above, is of critical importance if the desired Q values are to be achieved. In Fig. 4.6, constant lines of R_n are shown on a Q versus A plot where acceptable characteristics fall within the shaded area). The desired values of junction area, therefore, range from 0.4 to 1.6 square microns. Only a small range of areas, from 0.7 to 0.9 μm^2, permit fabrication of devices with the full range of desired Q.

Definition of areas less than 1 μm^2 is difficult to obtain utilizing a planar geometry with standard photolithographic techniques. Special fabrication techniques such as shadow masking or an edge geometry are needed to achieve smaller geometries without resorting to electron beam lithography. Mixer use at higher frequencies necessitates even smaller

Q= 2 f = 115 Ghz Jc = 8.83230E3

R	C	A
R = 2.00000E1	C = 1.38396E2	A = 8.87285E-1
R = 3.00000E1	C = 9.22637E1	A = 5.91524E-1
R = 4.00000E1	C = 6.91978E1	A = 4.43643E-1
R = 5.00000E1	C = 5.53582E1	A = 3.54914E-1
R = 6.00000E1	C = 4.61319E1	A = 2.95762E-1
R = 7.00000E1	C = 3.95416E1	A = 2.53510E-1
R = 8.00000E1	C = 3.45989E1	A = 2.21821E-1
R = 9.00000E1	C = 3.07546E1	A = 1.97175E-1
R = 1.00000E2	C = 2.76791E1	A = 1.77457E-1

Q= 3 f = 115 Ghz Jc = 5.71350E3

R	C	A
R = 2.00000E1	C = 2.07593E2	A = 1.37162
R = 3.00000E1	C = 1.38396E2	A = 9.14413E-1
R = 4.00000E1	C = 1.03797E2	A = 6.85809E-1
R = 5.00000E1	C = 8.30374E1	A = 5.48648E-1
R = 6.00000E1	C = 6.91978E1	A = 4.57206E-1
R = 7.00000E1	C = 5.93124E1	A = 3.91891E-1
R = 8.00000E1	C = 5.18984E1	A = 3.42905E-1
R = 9.00000E1	C = 4.61319E1	A = 3.04804E-1
R = 1.00000E2	C = 4.15187E1	A = 2.74324E-1

Q= 4 f = 115 Ghz Jc = 4.19700E3

R	C	A
R = 2.00000E1	C = 2.76791E2	A = 1.86725
R = 3.00000E1	C = 1.84527E2	A = 1.24483
R = 4.00000E1	C = 1.38396E2	A = 9.33623E-1
R = 5.00000E1	C = 1.10716E2	A = 7.46898E-1
R = 6.00000E1	C = 9.22637E1	A = 6.22415E-1
R = 7.00000E1	C = 7.90832E1	A = 5.33499E-1
R = 8.00000E1	C = 6.91978E1	A = 4.66811E-1
R = 9.00000E1	C = 6.15092E1	A = 4.14943E-1
R = 1.00000E2	C = 5.53582E1	A = 3.73449E-1

Table 4-1

ORIGINAL PAGE IS
OF POOR QUALITY

Q= 5 f = 115 Ghz Jc = 3.30490E3

R	C	A
R = 2.00000E1	C = 3.45989E2	A = 2.37126
R = 3.00000E1	C = 2.30659E2	A = 1.58084
R = 4.00000E1	C = 1.72995E2	A = 1.18563
R = 5.00000E1	C = 1.38396E2	A = 9.48505E-1
R = 6.00000E1	C = 1.15330E2	A = 7.90421E-1
R = 7.00000E1	C = 9.88540E1	A = 6.77504E-1
R = 8.00000E1	C = 8.64972E1	A = 5.92816E-1
R = 9.00000E1	C = 7.68864E1	A = 5.26947E-1
R = 1.00000E2	C = 6.91978E1	A = 4.74253E-1

Q= 6 f = 115 Ghz Jc = 2.71930E3

R	C	A
R = 2.00000E1	C = 4.15187E2	A = 2.88195
R = 3.00000E1	C = 2.76791E2	A = 1.92130
R = 4.00000E1	C = 2.07593E2	A = 1.44098
R = 5.00000E1	C = 1.66075E2	A = 1.15278
R = 6.00000E1	C = 1.38396E2	A = 9.60651E-1
R = 7.00000E1	C = 1.18625E2	A = 8.23415E-1
R = 8.00000E1	C = 1.03797E2	A = 7.20488E-1
R = 9.00000E1	C = 9.22637E1	A = 6.40434E-1
R = 1.00000E2	C = 8.30374E1	A = 5.76391E-1

Q= 7 f = 115 Ghz Jc = 2.30620E3

R	C	A
R = 2.00000E1	C = 4.84385E2	A = 3.39820
R = 3.00000E1	C = 3.22923E2	A = 2.26546
R = 4.00000E1	C = 2.42192E2	A = 1.69910
R = 5.00000E1	C = 1.93754E2	A = 1.35928
R = 6.00000E1	C = 1.61462E2	A = 1.13273
R = 7.00000E1	C = 1.38396E2	A = 9.70913E-1
R = 8.00000E1	C = 1.21096E2	A = 8.49549E-1
R = 9.00000E1	C = 1.07641E2	A = 7.55155E-1
R = 1.00000E2	C = 9.68769E1	A = 6.79639E-1

Table 4-1 continued

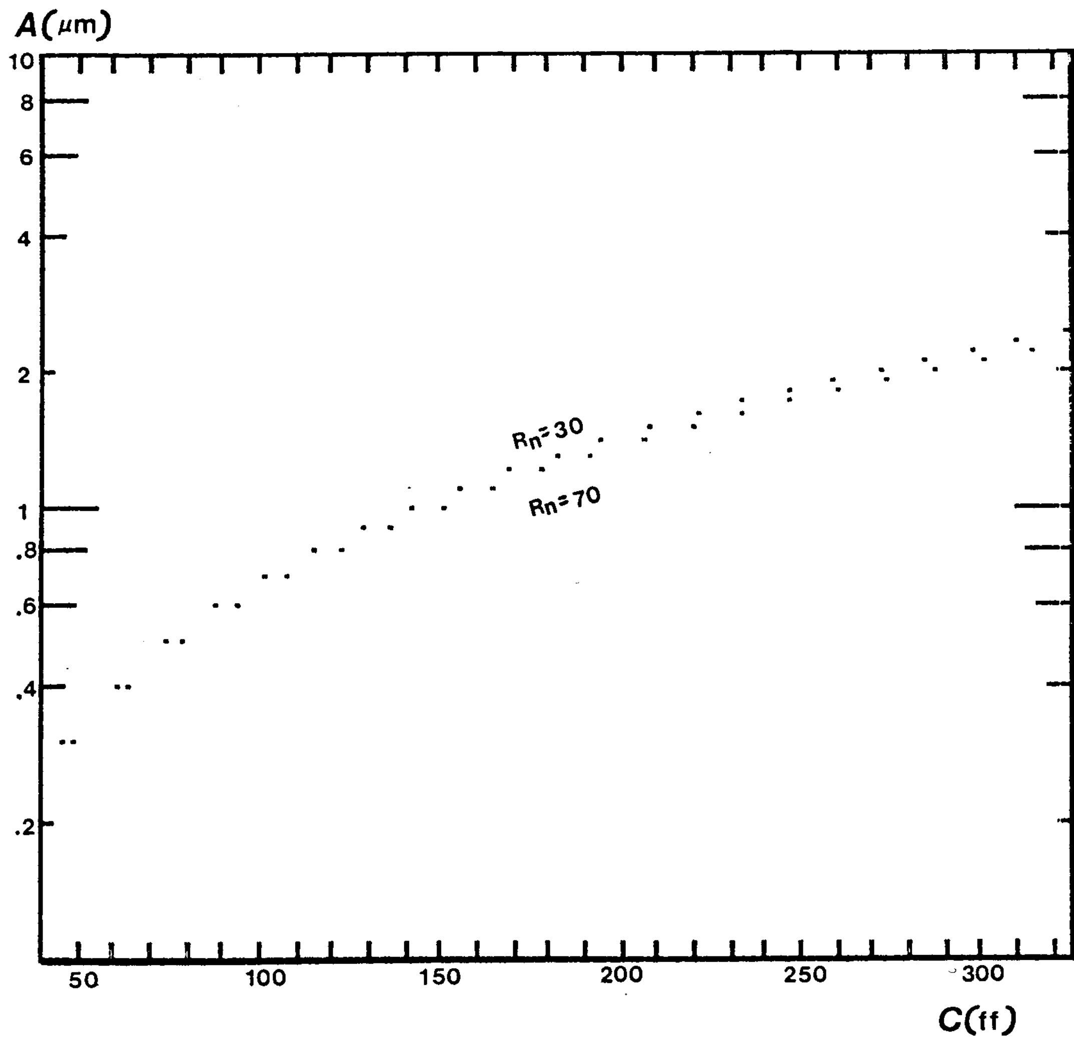

Figure 4.5 Lines of constant R_n are shown on an A versus C plot

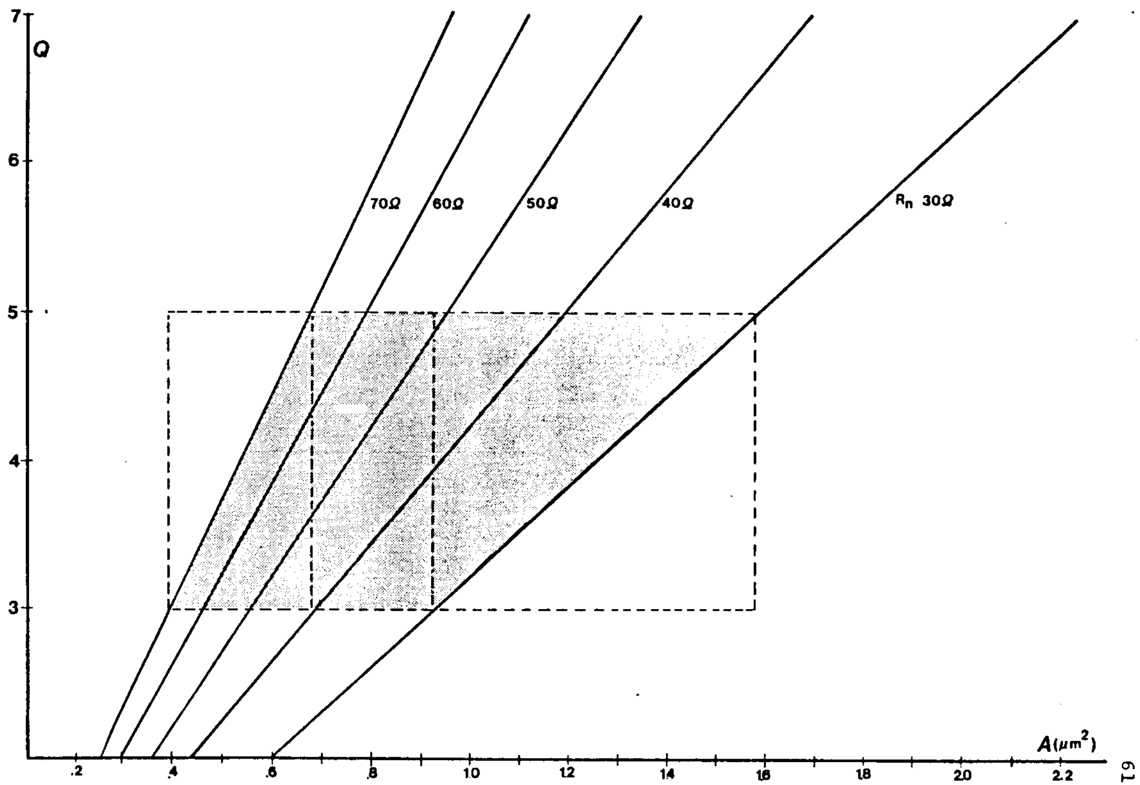

Figure 4.6 Lines of constant R_n are shown on a Q versus A plot

geometries. With Q = 5 and R_n = 50 Ω, a device designed for operation at 220 GHz and 350 GHz requires device areas of 0.48 and 0.29 square microns respectively.

An alternative to small area junction fabrication, is to utilize series arrays of junctions. If identical junctions are used, each junction with an area equal to N A, then the array presents a Q which is equivalent to that of a single junction with area A. Junctions with larger areas, which are easier to fabricate, can, therefore, be used to obtain the critical Q value. Since voltage and current scale with N, the use of arrays increases the saturation level of the device. Though arrays present potential advantages, for optimum use the array dimension should be small compared with $\lambda/4$ and all junctions must have approximately the same R_n [19]. These conditions, especially the uniformity of device characteristics, can prove difficult to achieve.

In addition to the parameters discussed previously (Q, R_n, A) the degree of deviation from the ideal I-V characteristics is very important for optimum mixer quality. The expected low subgap current and abrupt quasiparticle current jump are typically not fully obtained with actual devices. Often a ratio of the small signal resistance below the gap voltage to the small signal resistance above the gap voltage is given as a junction quality parameter. For Nb/Pb-alloy junctions, the chosen ratio is R(2mv)/R(4mv) or R2,4, such that the values collar the turn on voltage by

approximately 1mv. For the Nb/PbBi case (Fig. 3.12) the ideal value of R2,4 (at 4.2K) is approximately 55. [20]

There are three critical physical components in realizing a high quality SIS junction - the base electrode, insulating barrier and counterelectrode. The crucial step in device fabrication is the formation of the regions between 100 Å on either side of the barrier. A high quality base electrode material can be easily disturbed by the chosen cleaning process used prior to barrier formation or by formation of the barrier itself. The surface damage may reduce the T_c and the gap energy or even change the material to a normal metal, while the effects can occur locally or over the whole junction area. The reduction of gap energy and formation of states within the gap will result in a distribution of effective turn-on voltages such that the theoretically abrupt quasiparticle current jump can become quite rounded and render the device useless for mixer purposes.

Figures 4.7 a and b schematically show the effects of two cases of surface damage to the base electrode, assuming an ideal barrier and counterelectrode. In Fig. 4.7a, the damage has occurred in varying degrees across the surface, resulting in locally fluctuating values of gap energies. This device can be thought of as being composed of a number of junctions in parallel, each with a different $\Delta i + \Delta j$ turn on voltage. The resulting I-V curve will have a low subgap current for voltages below the smallest effective gap energy. Above this

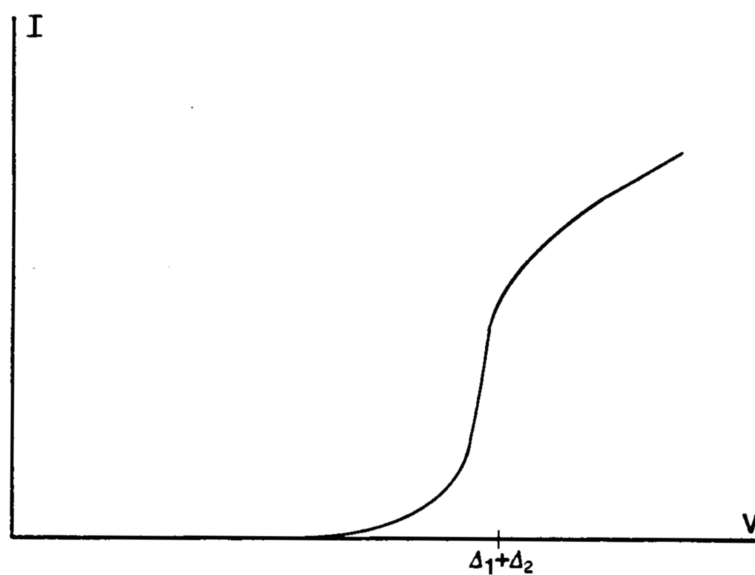

Figure 4.7a SIS I-V curve, for a case of a graded distribution of effective turn on voltage

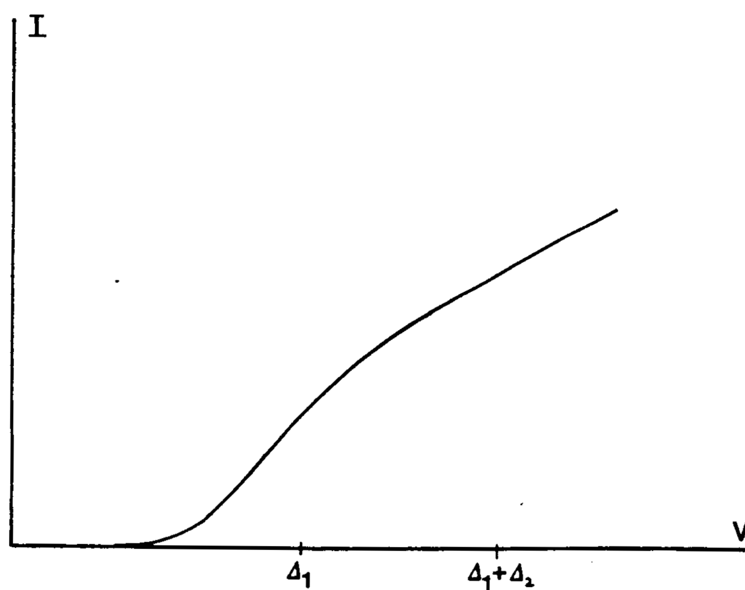

Figure 4.7b I-V curve for a NIS junction

voltage, however, the once abrupt turn on voltage will become rounded, due to the graded distribution of effective turn on voltages. In Fig. 4.7b, the damage is so severe that the material no longer has an associated gap energy near that of the barrier, such that the junction could be modeled as an NIS device.

Unfortunately, damage to the base electrode often affects the subsequently deposited barrier material, yielding a leaky tunneling barrier. Numerous materials and methods exist for barrier fabrication - the most suitable selection depends on the choice of base and counterelectrode materials in addition to the device geometry and method of fabrication. The optimal barrier is of uniform thickness and absent of potential tunneling states. A leaky barrier typically results in an increased current (subgap current) for all voltages below the gap energy.

Damage to the counterelectrode can result in detrimental effects mentioned previously for the base electrode. Damage to the barrier can also occur depending on the method of counterlectrode deposition and composition of the barrier. In the case of damaged superconducting materials, with a heterojunction the suspected material can be identified by examining the $\Delta 1 - \Delta 2$ cusp and the $\Delta 1 + \Delta 2$ turn on voltage. If the subgap current is fairly high, or the turn on voltage too rounded, accurate identification of the sum and difference of the gap voltages can be difficult.

The device fabrication techniques chosen to accomplish all these steps are of extreme importance; the complexity of this challenge will be considered in the following chapters for Nb/PbBi junctions.

CHAPTER V

Initial Fabrication Results

The initial work on this project was undertaken by J. Upshur and Dr. R. Mattauch. An edge geometry was eventually chosen, utilizing the submicron thickness available with a thin Nb film and the less than 2   photolithography capability of the Semiconductor Device Lab to achieve a sub square micron junction area. A considerable amount of attention by other researchers, however, had focused on lead or lead alloy junctions [21,22,23]. One of the material advantages of Pb over Nb is that the dielectric constant for its native oxide is approximately 3-4 times smaller than that of Nb_2O_5. The desired Q of 4 can, therefore, be obtained with a larger junction area for the Pb technology, obviating the need of an edge geometry. A planar geometry is typically chosen with a barrier formed by thermal oxidation in oxygen or even in the atmosphere.

Though relatively promising results below 115 GHz had been obtained with Pb alloy mixers, [24,25] several disadvantages are associated with this technology. It is well known that pure lead films degrade mechanically with thermal cycling. The existing mechanical strain often results in damage to the oxide tunnel barrier, or even an electrical short between the two superconducting electrodes [26]. Though it has been shown that some Pb alloys (deposited

by observing precise schedules) have improved thermal cycling characteristics with respect to mechanical strain, Pb alloy devices have generally demonstrated a gradual drift in device characteristics with time [27]. Pb alloy films are difficult to pattern for small line widths. In addition, the films are typically not mechanically durable enough to sustain a simple photolithographic step. The use of the overlap technology associated with the Pb junctions, for frequencies greater than 115 GHz, would also prove very difficult because of this size limitation.

The choice of Nb as a base electrode was made for several important reasons. Nb is a mechanically rugged refractory metal which is physically compatible with photolithography and numerous patterning steps. Nb devices have also demonstrated superior mechanical and electrical stability properties to lead devices.

Though the edge geometry, as initially planned, utilizes both Nb and a Pb alloy, it was thought that this structure would be a promising step toward an all Nb junction. A schematic drawing of the Nb/Pb alloy device is shown in Fig. 5.1. The technology utilized draws from earlier work at IBM and Cornell University in addition to considerable development at the University of Virginia. A general summary outline of the fabrication technology developed until January 1982 is presented below.

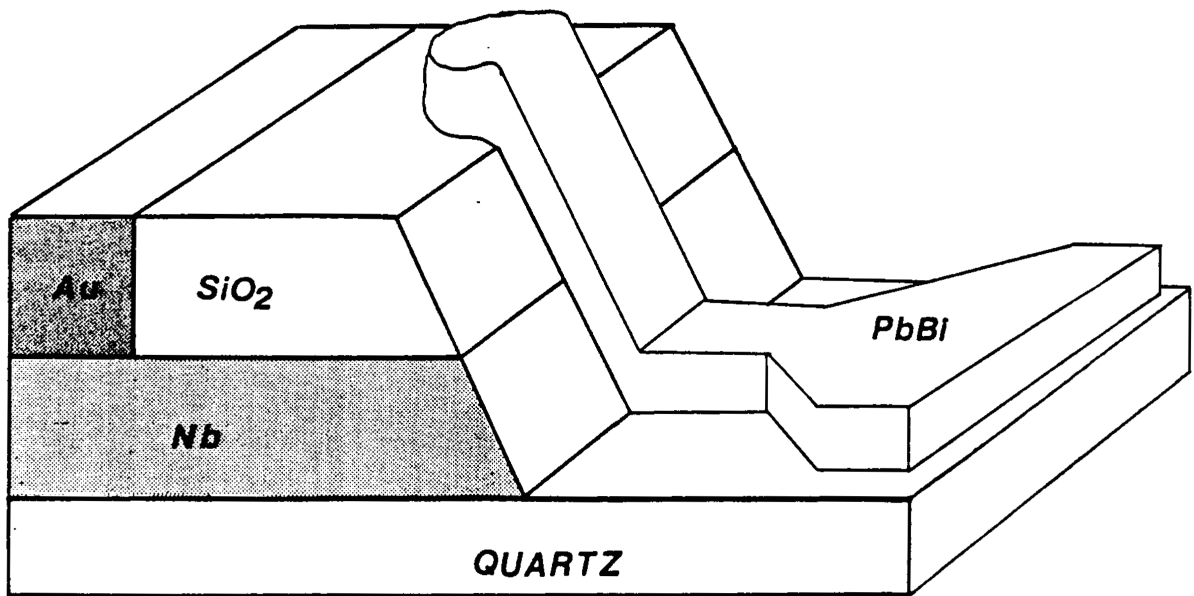

Figure 5.1 Schematic of a Nb/Pb alloy edge contact device

The substrates used are fused Suprasil II quartz (Amersil, Inc.), 19 mm x 19 mm x 7 mils thick, chosen for their superior R.F. properties. The Nb base electrode film was deposited by RF sputtering in an argon plasma at the University of Virginia Physics Department. The Nb target and substrate were sputter etched clean prior to deposition of the approximately 2,000 Å thick film. The system base pressure was typically 2 x 10^{-7} torr. The substrates were then transferred to a different sputtering machine where a sputter etch of the target and substrate was performed followed by the deposition of approximately 9,000 Å of SiO_2. That system's base pressure was typically 2 x 10^{-6} torr. This layer was subsequently patterned with a photolithographic step in the base electrode geometry, as shown in Fig. 5.2. Utilizing the photoresist as a mask, the exposed SiO_2 was removed with a BHF etch and the photoresist subsequently removed with acetone. An ion milling process was then performed, using the dielectric pads as a mask to the 600 eV argon ion beam, removing the exposed Nb film. This step creates an edge in the SiO_2/Nb structure on which the junction area will subsequently be defined. The substrate mount is cooled to 200-250 K during this step for two reasons. Without cooling the ion beam cross links the photoresist, making subsequent removal of the photoresist very difficult. It has also been shown that, without cooling, ion milling at these energies will adversely effect

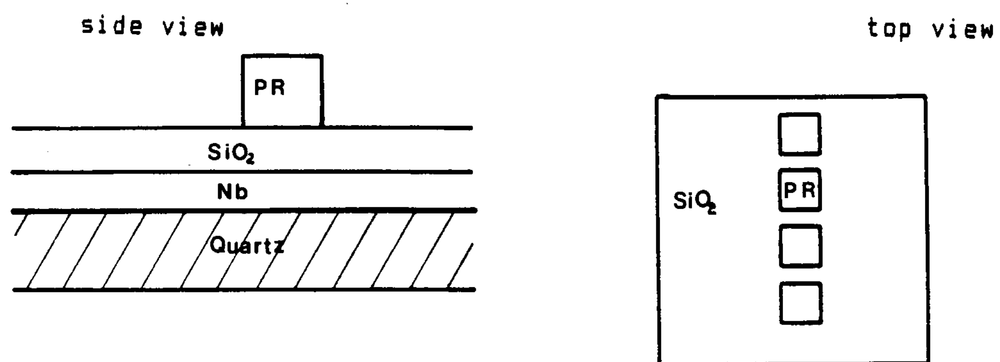

Figure 5.2 Base electrode patterning with photoresist

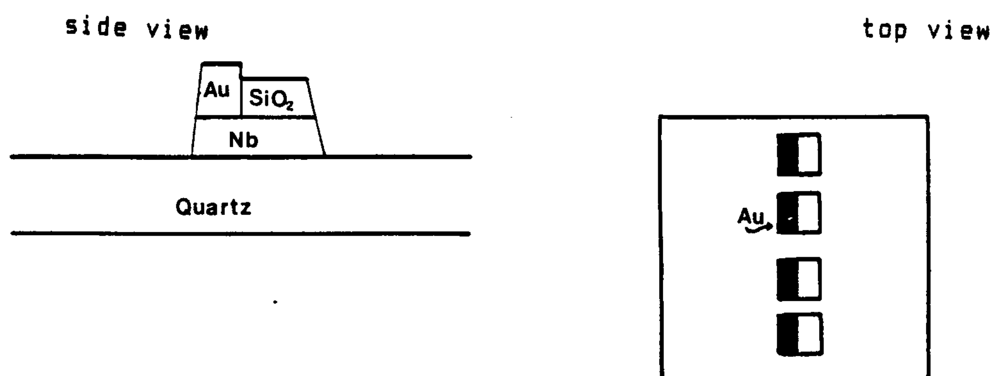

Figure 5.3 Gold contact pads on Nb

the superconducting quality of the Nb film.

The next photolithographic step defined a window in the photoresist on the back half of the base electrode. The exposed SiO_2 was then removed with a BHF etch, forming a contact window to the Nb substrate. A 4,000 Å thick film of gold was then RF sputter deposited onto the chip after a sputter etch cleaning of the exposed Nb surface. The regions of gold covering the photoresist were lifted off with acetone, leaving gold contact pads on the Nb surface (Fig. 5.3).

The final photolithographic step involved definition of the photoresist counterelectrode liftoff stencil. This stencil primarily consisted of a thin open 'finger', 2-4 μm wide, overlapping the SiO_2/Nb edge with an undercut in the profile of the photoresist as shown in Fig. 5-4. A 600 eV argon ion beam was then employed to clean the exposed Nb, using the photoresist stencil as an ion milling mask. The substrate mount was cooled to approximately 200 K during this step. Following the removal of 100-200 Å of surface oxide and Nb, such that the edge plane presents a clean Nb surface, the ion beam was switched off.

An approximately 30% O_2, 70% Ar gas mixture was then obtained and the 600 volt ion beam re-established within a period less than one minute. This reactive ion beam oxidation step was then employed for approximately 30 seconds to form a thin Nb_2O_5 (native oxide) tunnel barrier on the

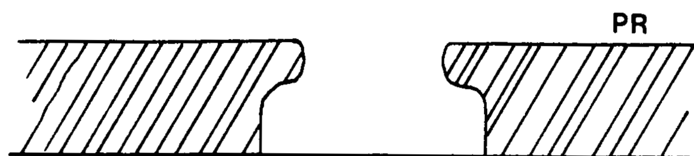

Figure 5.4 Counterelectrode photoresist profile

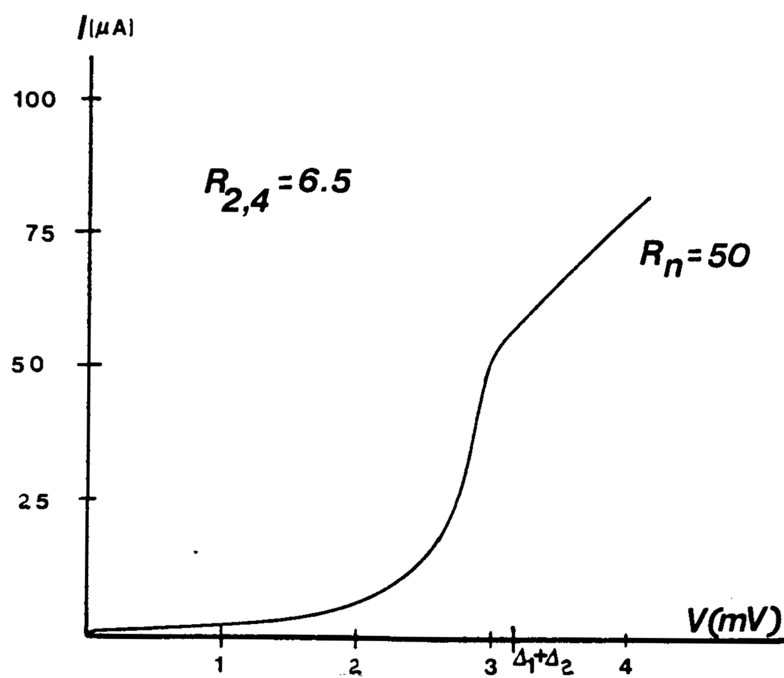

Figure 5.5 Typical I-V curve of a Nb/PbBi device for initial results

exposed Nb. A PbBi counterelectrode was then immediately deposited by thermal evaporation, after a 90% rotation of the substrate holder away from the ion beam, toward the evaporation source. A pre-weighed 28% Bi and 72% Pb charge was evaporated to completion such that an approximately 4,000 A thick film was obtained. This particular PbBi composition is generally referred to as ε phase PbBi, and results in a single phase alloy film. The evaporation system was equipped with a shutter such that the PbBi can be outgassed and heated to a liquid state before counterelectrode deposition. A liftoff step was performed, after removal of the chip from the vacuum system, by soaking the chip in acetone, resulting in five or six completed devices. The processing was completed with the use of a protective covering layer of photoresist to prevent further oxidation and adsorbtion of moisture from the atmosphere. A more detailed discussion concerning device development and changes in fabrication technology from January 1982 to April 1984 follows. This material will be presented for the most part chronologically such that different aspects of the general fabrication technology will be examined more closely as its relevance becomes apparent.

Initial results obtained with this technology were very promising. In Fig. 5.5, a typical I-V curve of a Nb/PbBi device ($R_{2,4}$ = 6.5) is shown. Though the general tunneling characteristics of an ideal SIS device are present, many

non-ideal effects are also exhibited. Of particular importance is the fairly rounded quasiparticle current jump. The I-V 'turn on' structure, expected to be an abrupt 'knee' at $\Delta_1 + \Delta_2 = 3.14$ mV, is actually quite rounded for biases between 1 and 3 mV. However, the subgap current, for biases below 1 mV, is relatively low.

These non-ideal effects indicated the existence of a distribution of gap energies. It was hypothesized that the superconducting quality on the edge of the Nb film had deteriorated. It is well known that value of the energy gap of Nb decreases for films less than 1,000 Å thick. Utilizing an SiO_2 ion milling mask for formation of the base electrode edge (as described above), the typical edge angle achieved was less than 30°, as shown in Fig. 5.6. Nb also has a rather short coherence length of ~100 A. For 30° edge angle, there would exist a film edge length of approximately 200 Å, which would be supported by $\leq$ 100 Å of Nb (Fig. 5.6). It was, therefore, thought that the tapered portion of the Nb edge was presenting a graded distribution of energy gap values, resulting in a rounded current jump below the expected sum potential.

The choice of SiO_2 as a milling mask for the base electrode step had been made for a number of reasons. The technology for SiO_2 deposition and the patterning of such films by chemical etching had been previously developed in the Semiconductor Device Lab. Unfortunately, the ion milling

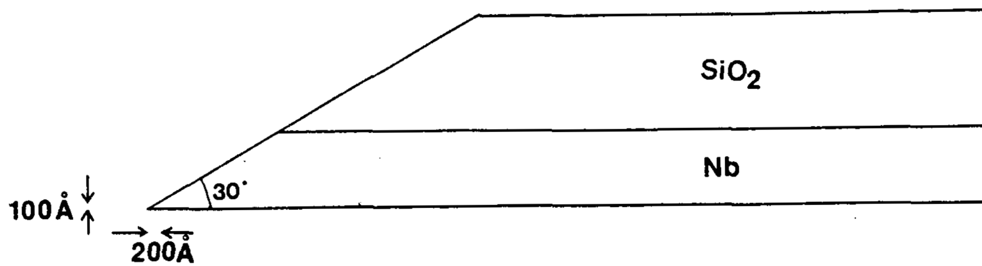

Figure 5.6 Tapered edge profile with edge angle of 30°

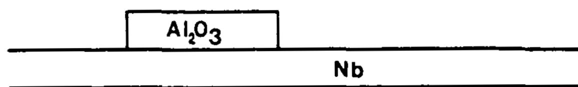

Figure 5.7a Al_2O_3 pad on top of the Nb film

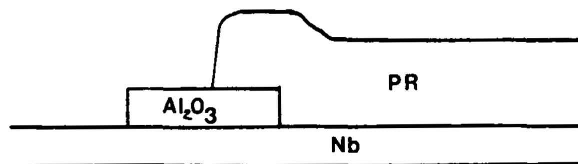

Figure 5.7b Photoresist definition prior to base electrode formation with ion miling machine

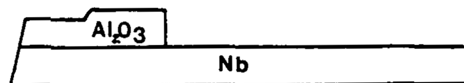

Figure 5.7c Resulting Al_2O_3/Nb base electrode edge structure

rates of SiO_2 and Nb films are nearly identical, resulting in a small edge angle. In order to obtain a steeper edge angle, an alternative Al_2O_3 milling mask technology was developed. The milling rate of Al_2O_3 is more than three times less than the rate of Nb such that the use of Al_2O_3 in the edge milling step should result in a more desirable, steeper profile.

This process was begun with the deposition of 2,500 Å of Al by RF sputtering in an argon plasma. A photolithographic step, which is nearly the inverse of the previous base electrode step, was then performed. An open window in the photoresist, of the same general shape as the previously solid photoresist base pads, was defined on top of the Al/Nb metal layer. The exposed Al layer was then converted to Al_2O_3 by an anodization process. The photoresist and remaining Al were then removed, leaving an Al_2O_3 pad on top of the Nb film (Fig. 5.7a). Since Al_2O_3 is very difficult to pattern chemically, the length of this pad was designed to be shorter than the previous, full length base electrode structure. Another photolithographic step was, therefore, executed, defining solid photoresist pads which partially overlapped the Al_2O_3 structures, as well as regions of the Nb film (Fig. 5.7b) to allow eventual electrical contact for device testing. An ion milling step, exactly the same as used in the SiO_2 technology, was employed to form the final Al_2O_3/Nb base electrode edge structure

(Fig. 5.7c).

In order to develop this new process, a number of technological problems had to be solved. Some of the more sensitive processing parameters will, therefore, be discussed below.

The major difficulty encountered centered on the anodization of the exposed Al film. The anodization was performed in a 0.05 M ammonium tartrate solution with the aluminum film as the anode and a strip of platinum for the cathode. The anodization cell was driven by a constant current supply which yielded a current density of approximately 500 $\mu A/cm^2$. The anodization rate was calibrated at ~13 Å/V. Unfortunately, the thickness of the resulting Al_2O_3 film is 1.7 times the thickness of the original fim. This differential resulted in poor adhesion of the photoresist to the growing Al_2O_3/Al step. As the thickness of the Al_2O_3 film was increased, the edges of the photoresist mask would pull away, resulting in a ragged Al_2O_3 definition.

Initial results for thermally deposited Al films were very poor as less than 500 Å of Al_2O_3 could be formed before the photoresist would begin pulling away. If the anodization was continued, the entire layer of photoresist would eventually lift off. This problem was alleviated with three changes in the fabrication technology. First, the method of Al deposition was changed from thermal evaporation to RF

sputtering. If the substrate was thermally attached to the cooled sputtering table, the resulting small grained films were much harder and more durable than the evaporated films. Secondly, it was determined that if the traditional organic cleaning step (ethanol, tricloroethylene and methanol) performed prior to base electrode photolithography was omitted then the photoresist adhesion was greatly improved. The photolithographic step was, therefore, begun immediately following completion of the Al sputtering. The third important step was the optimization of the photoresist postbake process prior to anodization. It was determined that liftoff was minimized if a 120 C postbake was used for 20 minutes, the temperature of the postbake being the more crucial factor.

Although the Al_2O_3 technology successfully yielded a much steeper edge angle, the quality of the resulting I-V curves was not improved. In fact, the $R_{2,4}$ ratio for such devices (Fig. 5.8) had decreased from 6.5 to 5.3 with respect to the SiO_2 devices. Further work spent experimenting with the Al_2O_3 technology resulted in devices with even lower $R_{2,4}$ ratios. A return to the previous SiO_2 technology showed no improvement in device quality. The conclusion drawn was that the edge slope angle was not the dominant factor, i.e., there was some other fabrication step to which the device I-V characteristics were highly sensitive. This deterioration of device quality and the efforts involved toward pinpointing the source or sources of this degradation will be the subject of Chapter VI.

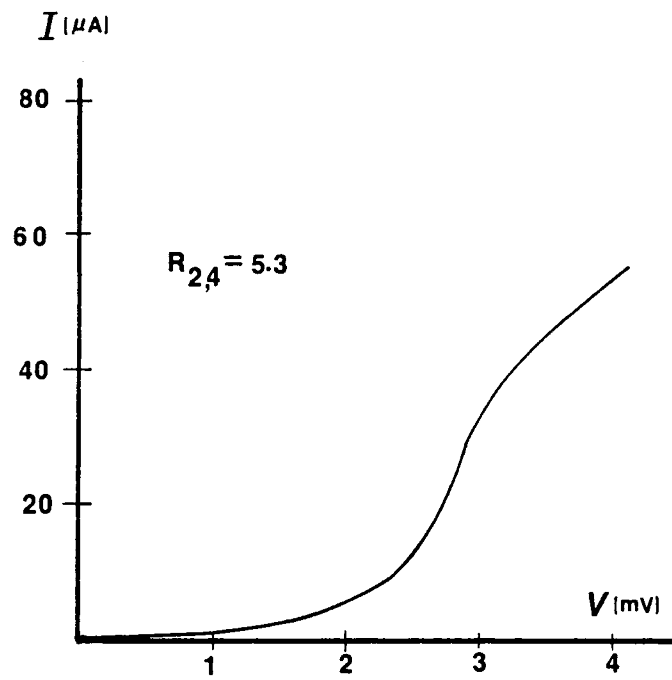

Figure 5.8 Initial I-V curve obtained with Al_2O_3 technology

CHAPTER VI

A Search for the Mechanism of Device Quality Deterioration

Despite attempts to identify and reverse the deterioration of device quality, the degradation continued until February 1983, at which point the I-V characteristics were completely ohmic, lacking all SIS structure. The efforts involved in tracking the causes of device deterioration and the subsequent alterations to equipment and fabrication procedure will be discussed in this chapter.

Before the degradation search is considered, it would be helpful if Appendices A and B were examined. In Appendix A, the general fabrication procedure is explained in more detail than outlined in Chapter V. Specific temperatures, times and chemicals, etc. used in the processing steps are given for the reader to refer to when considering subsequent processing changes. A new SiO_2 base electrode defining technology was developed after the Al_2O_3 method was optimized. This new SiO_2 method utilizes a photoresist/SiO_2 ion milling mask, as opposed to just the SiO_2 of the previous structure, to define the base electrode geometry. Since this technology was much simpler than the Al_2O_3 method and resulted in fairly steep edge angles, the new SiO_2 method was utilized in most of the remaining SIS efforts.

In Appendix B, an introduction to the theory of ion gun operation is given. Since the extremely sensitive device

fabrication steps of cleaning and oxidation involve the use of an ion gun technology, a knowledge of ion gun operation is imperative. A description of the ion gun and associated vacuum chamber used for much of this work is also included in Appendix B.

In the search for the degradation mechanism one of the first areas pursued was the integrity of the superconducting materials. Traditionally, the characteristics of the superconducting transition of the material is used as a quality test for thin films [28]. A T_c value below the transition temperature established for bulk material or a gradual superconducting transition is an indication of poor quality material. Both the Nb and PbBi showed sharp transitions at 9.1 K and 8.3 K respectively. The critical current densities for both materials were obtained from weak-link structures. The measured values for critical current density of 10^7 A/cm^2 correspond to bulk values, indicating quality materials. An alternative quality parameter, often quoted for Nb, is the ratio of a film resistance at room temperature to the resistance measured at 10 K (commonly referred to as the resistance ratio). The measured value of ~3 corresponded to values commonly reported for Nb [18]. Though these results were positive, these tests had not originated as a test of quality for SIS tunnel devices but rather only as an indicator of the superconducting quality of the material.

The possibility that a contaminant was being introduced in one of the processing steps was also fully examined. The extremely crucial step of ion cleaning and oxidation was first investigated. All chamber walls, in a direct line-of-sight with the ion beam, were covered with pure Nb foil. A Nb cover for the copper substrate holder was also installed in an attempt to reduce possible backsputtering of impurities during milling. The ion milling gun, chamber and diffusion pump were disassembled and thoroughly cleaned. This cleaning process was composed of several steps: an acetone wash, a hot H_2O and alconox wash, several hot H_2O rinses, a TCE rinse, a methanol rinse and a 200°C oven bakeout. All O-rings were replaced and the diffusion pump oil changed.

During the cleaning, copper deposits were found on the two alumina insulating rings adjacent to the filament of the ion gun. This copper was deposited by low energy sputtering of the two copper pieces supporting the filament cathode. This design flaw was corrected by mounting the filament via two electrical feedthrough insulators on a brass back plate which is in direct physical contact with the anode chamber. The cathode-anode potential difference is thereby established only at the filament and its holders, significantly reducing the sputtering of metallic impurities from the interior of the gun. The original and replacement design are shown in Fig. 6.1.

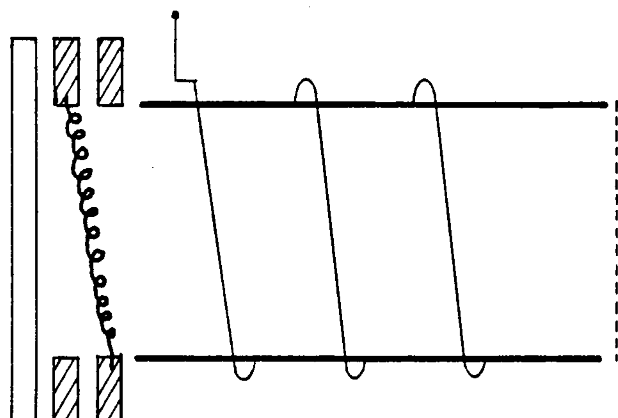

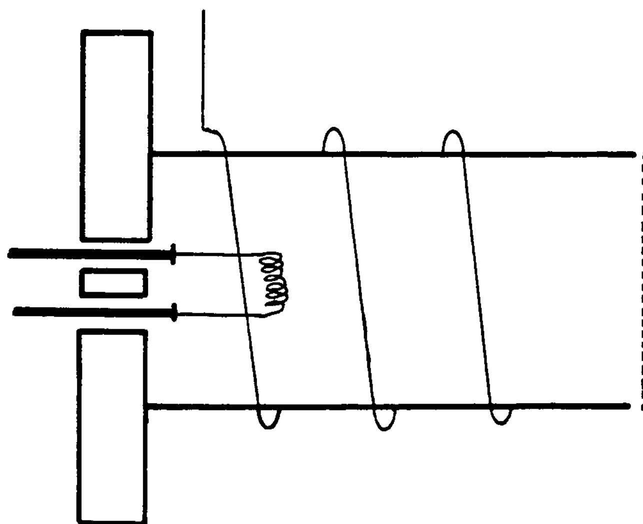

Figure 6.1 Original and replacement designs of the filament assembly

It was also discovered that the carbon grids, provided with the gun, were formed from an unpurified grade of graphite. These grids were replaced with pyrolitic graphite (obtained from B.F. Goodrich Company) containing less than 5 ppm total impurities. Since the ion filament is constantly subjected to ion bombardment (~50 eV), the filament was periodically replaced in an attempt to return the system to the initial operating conditions. Though it was felt that all of the above modifications to the ion gun were beneficial, no improvement in the device quality was seen.

In an attempt to isolate the effects of the ion oxidation step, a number of devices were fabricated utilizing a thermal oxidation step to form the Nb_2O_5 tunnel barrier. In this method the filament and the argon were turned off after the ion cleaning process and an oxygen pressure of 4×10^{-4} torr was established in the chamber. This pressure was maintained for a period of 60 minutes while a thermal oxide was formed. The chamber was subsequently evacuated (pressure $< 1 \times 10^{-6}$ torr) and the substrate holder, which had been allowed to thermally drift from approximately 180 K to approximately 240 K, was recooled to a temperature $T \sim 180$ K. The standard process of evaporation was then resumed. A typical I-V curve resulting from this method is shown in Fig. 6-2. Unfortunately, this test did not alter the continuing trend of device quality degradation.

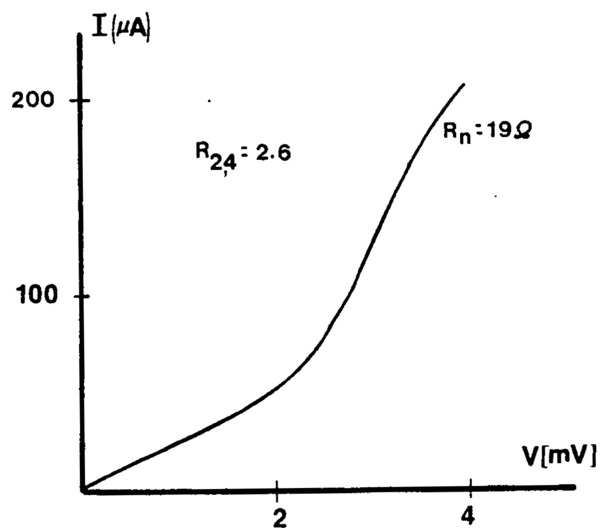

Figure 6.2 Typical I-V curve obtained with thermal oxidation technology

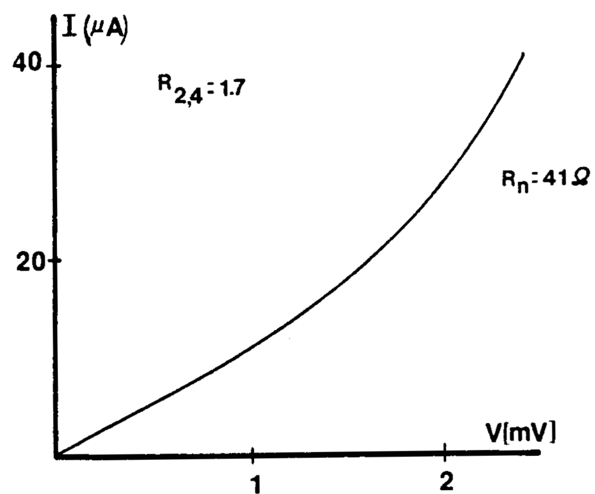

Figure 6.3 Typical I-V curve obtained with extended cleaning step (40 min.)

The peculiar nature of this problem was a very slow rate of deterioration. The quality of devices fabricated on chips on successive months deteriorated slightly but steadily. The impetus for a number of changes to the fabrication schedule was centered on the hypothesis that some sensitive portion of the various fabrication processes was slowly becoming less effective. For example, the duration and temperature of the postbake used in the photolithographic base electrode step was re-examined. Devices were fabricated with postbake parameters changed by varying degrees from the standard method.

Another consideration was the ion milling cleaning step, prior to oxidation. Cleaning times of various durations were examined. It was found that cleaning times less than approximately 5 minutes resulted in a linear I-V structure, however, cleaning durations 2 to 3 times the nominal period of 15 minutes yielded no improvements (Fig. 6-3).

Lower ion beam supply voltages were also used in an attempt to minimize possible surface damage from the argon ions. The edge structure was still formed with a 600 eV beam, however, beam supply votlages of 300, 400 and 500 volts, for the cleaning and oxidation step, were utilized. In Figure 6-4, the I-V curve resulting from such a run with V_{BS} = 350 volts is shown. There is no trace of SIS structure, the I-V characteristics were simply ohmic. At this juncture the task of tracing the source of degradation

C-2

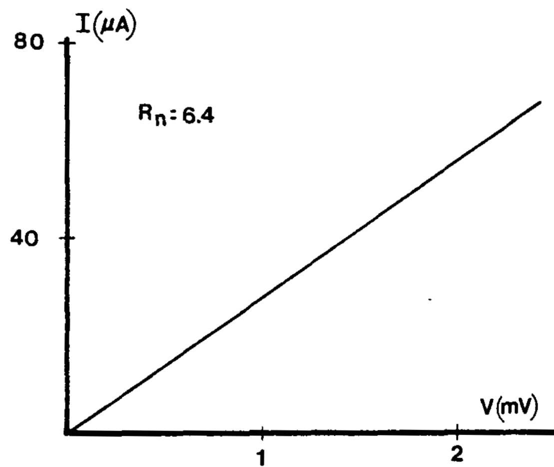

Figure 6.4

Typical I-V curve obtained with low voltage cleanand oxidation (350 volts)

became even more difficult. With no SIS I-V structure, only "positive" effects on device quality could be measured, whereas previously both "positive" and "negative" effects could be seen. Unfortunately, during much of the work after this point, there was little evidence that various alterations in the fabrication technology were having any effect, positive or negative.

Numerous efforts were also focused on the possibility that an undesirable contaminant had been introduced through one of the reagents or materials used in the fabrication steps. All processing solvents, etches and photolithograhic chemicals were replaced. Different ovens were used in the processing and all the beakers were replaced. A method in which the Pb and Bi pellets were alloyed in a pure carbon boat was developed. The pellets were alloyed in a forming gas atmosphere (95% N_2/5% H_2) for 5 minutes at which point the charge was well mixed and shiny. The charge was then removed and immediately placed in a beaker of methanol to prevent formation of a surface oxide. The charge was subsequently set in the evaporation boat and the chamber was quickly roughed out and opened to the diffusion pump.

As a further check on the quality of the superconductive materials, an x-ray analysis was performed on an RF device. No impurities were detected except Ar in the sputtered SiO_2, a common occurrence for films sputtered in Argon plasmas. Unfortunately, this technique is not sensitive to elements

with atomic weights below 24 - most notably carbon and oxygen.

One rather interesting hypothesis centered on the possibility that a crucially needed "contaminant" present initially in some processing step, had been slowly removed or depleted. In particular, a 'contaminant' present in the ion milling gun or chamber might have been removed through repeated use. The system might have become too clean!

An analogous case involving the fabrication of large area SIS devices (where the presence of an unintended impurity was necessary for optimal results) had been reported by Raider et al. [29,30] Their work involved fabrication of Nb/Pb alloy overlap devices, utilizing an argon RF plasma etching of the Nb film prior to oxidation. An oil diffusion pump was used to evacuate their system to ~10^{-8} torr while the cleaning and oxidation steps were performed at a pressure of ~3 μtorr. The conditions required to obtain optimal tunnel barriers with this system were quite unexpected. Tunnel barriers with the most nearly abrupt Nb/Nb_2O_5 interface yielded I-V characteristics with the highest subgap current. However, barriers with a 25-30 thick NbCO intermediate region between the Nb and the native (Nb_2O_5) oxide [31] resulted in optimal devices. The NbCO formation was traced by Raider to the plasma cleaning step where the thickness of this transition region was found to be directly related to the applied RF voltage. Utilizing RF voltages of

~1,100 V, oxygen and carbon impurities, which were unintentionally present in the chamber, were implanted into the Nb. Subsequent plasma oxidation of this surface transformed a portion of the NbCO region into the Nb_2O_5 layer. Devices without the NbCO layer were found to have regions of NbO between the Nb and the Nb_2O_5 tunnel barrier.

The interpretation given for these results [32] was that the NbCO layer shielded the Nb from direct oxidation, preventing formation of NbO - a conductive suboxide of Nb. The NbCO was thought to act as a transition region between the oxygen sensitive Nb and the desired Nb_2O_5 barrier.

Returning to the degradation problem, the possibility existed that a carbon impurity, present initially in the ion gun chamber and required for formation of a NbCO transition layer, had been slowly cleaned away. A lecture bottle of methane gas, to be used as a source of carbon impurity, was incorporated in the gas manifold. Several different schedules for introducing the CH_4 during the cleaning and oxidation steps were developed. In one such schedule the cleaning step was performed with a gas mixture of 10% CH_4 and 90% Argon. In another schedule the CH_4 was admitted for only the last minute of the fifteen minute cleaning step. These and other methods, however, failed to change the resulting ohmic I-V characteristics of the SIS devices.

The growing concern about the background gas composition led to a simple test of vacuum integrity. A chip was

processed following the usual procedure until the ion cleaning step was completed. At this point one of two different procedures would be followed. The first method involved the omission of the oxidation step by immediately turning the substrate into a flux of PbBi. The second method involved the omission of the oxidation step, followed by a one minute pause before evaporation of the PbBi (which formed the counterelectrode). Critical currents were then measured for the resulting devices. Critical current density values resulting from the first method corresponded to bulk values. Results from the second method, however, were two order of magnitudes lower than bulk values. During the one minute pause approximately 8 Å - 12 Å of background gas had formed on the surface.

It was not known whether this condition had always existed in the system or if it was symptomatic of the degradation problem. A leak detector was not conveniently available to check the integrity of the vacuum system, however, an unconventional method was utilized to initially check the system. The vacuum system was evacuated to 9×10^{-7} torr. Helium gas was then directed toward the various seals of the vacuum chamber. When the gas was aimed at the ion gun, the pressure indicated by the ionization gauge decreased to 6×10^{-7} torr. It was apparent that the He gas was entering the chamber through a leak in the ion gun and effecting the ionization gauge operation. It was determined

that the O-ring seals, associated with each insulator ring, leaked (see Appendix B).

The sites of the leaks were in a very sensitive region since entering gas impurities would diffuse directly into the ion beam. It was discovered that the o-ring grooves on the magnet, two grid rings, and the two neutralizer rings had been improperty machined. After a replacement of the o-rings and a machining of the grooves failed to improve the vacuum seal, it was decided to construct a new vacuum chamber in which to entirely enclose the existing ion gun. A chamber was designed (Fig. 6.5 and 6.6) which had a larger clearance between the beam path and chamber walls and which utilized only nine o-rings in comparison to twenty-five for the previous chamber. The ion gun was mounted directly onto a water cooled brass back plate which was isolated from the chamber ground by a plexiglass ring. The o-rings associated with the insulating rings of the ion gun, providing no further purpose, were removed.

Nb/PbBi junctions were subsequently fabricated with the new chamber. The resulting I-V device curve, though of rather poor quality with an excessive subgap current, possessed a weak SIS tunneling structure with a turn-on voltage at the sum of the gap energies (Fig. 6.7). The enclosure of the ion gun within a separate vacuum chamber reversed the pattern of device quality degradation for the first time in two years. However, it appeared that enclosing

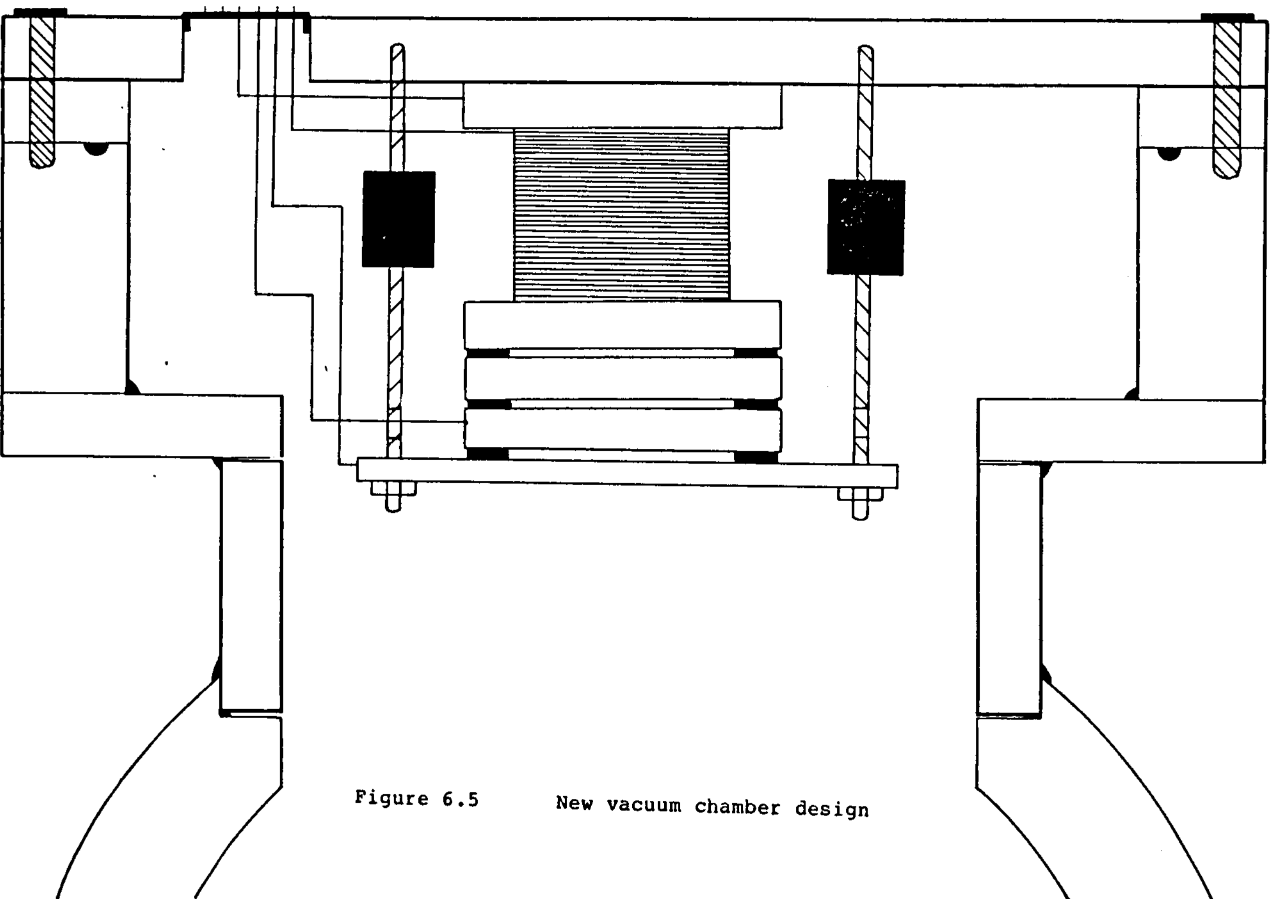

Figure 6.5 New vacuum chamber design

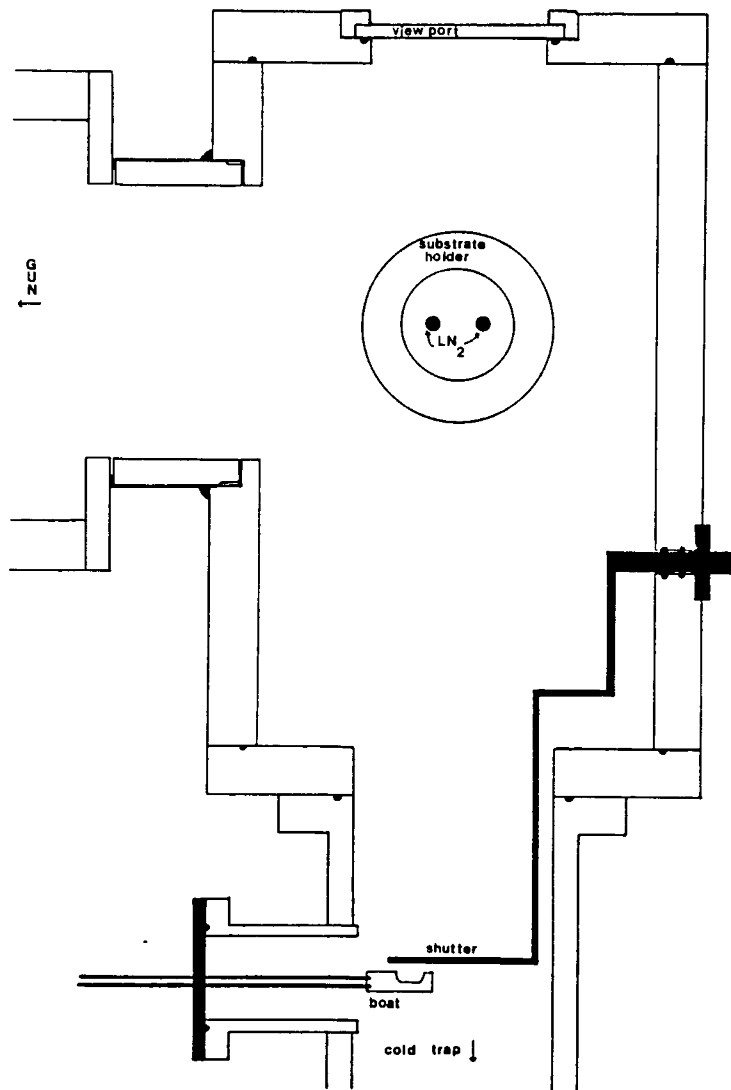

Figure 6.6 New vacuum chamber design

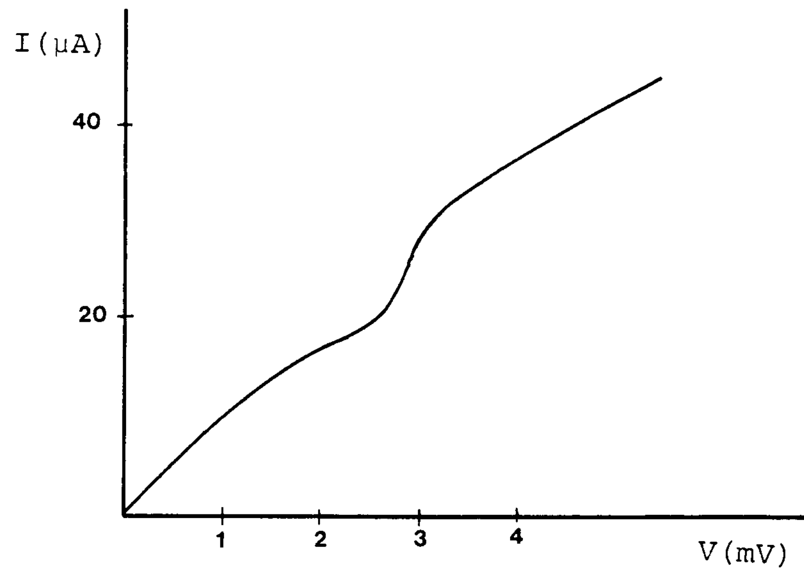

Figure 6.7 Initial I-V curve obtained with new chamber

the ion gun only slightly diminished the effect of some contamination source which was effecting the quality of the tunneling barrier. The integrity of the insulator rings as a vacuum material was immediately suspected. Five plate glass rings were fabricated by slowly grinding the pattern in pieces of plate glass with two concentric brass tubes.

With the new glass rings installed, the operational pressure range increased from a 1×10^{-4} - 4×10^{-4} torr interval to a 5×10^{-4} - 4×10^{-4} torr pressure range. Nb/PbBi junctions were subsequently fabricated; the resulting I-V curves of two junctions, representative of the chip, are shown in Fig. 6-8. A dramatic improvement in device quality was evident; the subgap current was much smaller and the turn-on voltage knee was sharper. The $R_{2,4}$ ratios of these two devices were 3.8 and 4.7. Though these ratios were less than the highest ratios obtained (6.5) before the degradation problems occurred, these results were very encouraging. The old alumina ion gun insulating rings were thought to have been poorly fixed, such that a porous interior material was exposed after a year of ion milling. These rings, which collar the plasma and the existing ion beam, were outgassing (acting as a virtual leak) directly into the plasma and ion beam, contaminating the tunnel barrier.

Two further chips were subsequently fabricated in order to verify the results of chip #37. The I-V curve of the highest quality junction is shown in Fig. 6-9. The $R_{2,4}$

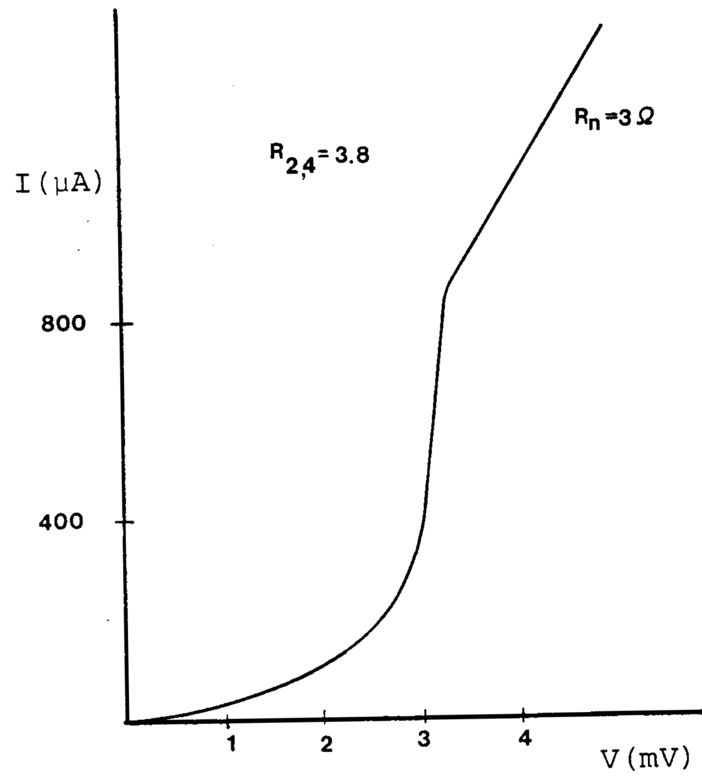

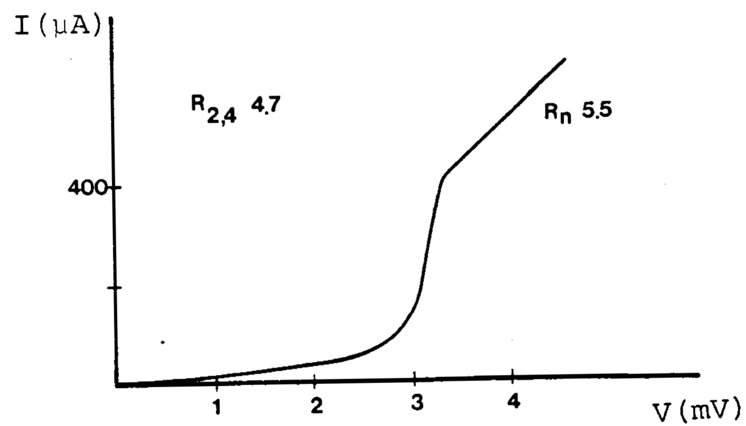

Figure 6.8

Resulting I-V curve obtained with new glass insulator rings

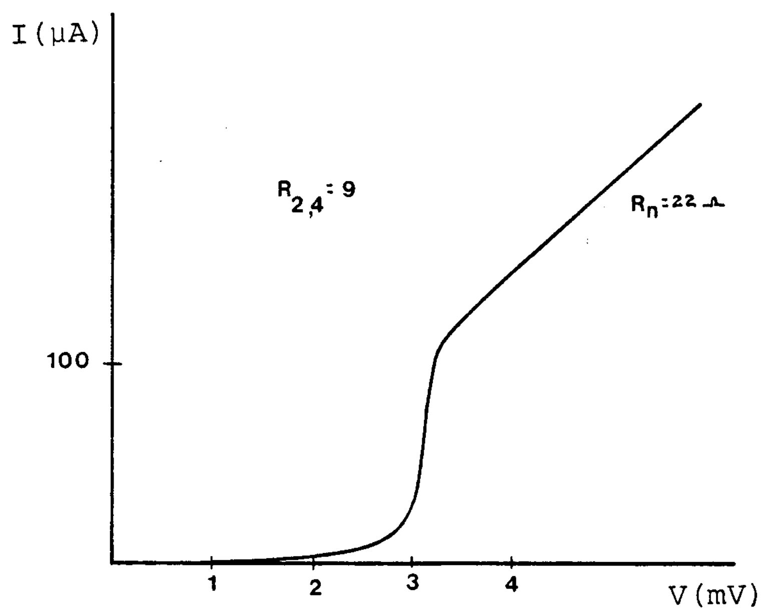

Figure 6.9 I-V curve of the highest quality obtained in this work

ratio was equal to 9, at that time this was the largest ratio ever obtained for a SIS device at the University of Virginia. Unfortunately, devices of only fair quality, characterized by $R_{2,4}$ ratios as low as 2.4, were fabricated on the same chips. It was suspected that the photoresist counterelectrode might have been backsputtered into the junction area during the cleaning and oxidation steps, causing nonuniform results. A device structure, utilizing a SiO_2 window (collared by a photoresist counterelectrode) to define the device area, was subsequently developed (Fig. 6.10). Though two chips were fabricated, no improvement of electrical uniformity across the chip was found.

The batch of Nb, which was being utilized at that time, was examined and the value of the resistance ratio was found (R_{room}/R_{10K}) to have decreased from a previous value of three to a significantly lower value of two. These films were thought to be of too low a quality for SIS tunnel junction fabrication such that an alternative source of Nb films was sought.

At a meeting with Dr. d'Addario of NRAO, it was suggested that James Beall [33] at NBS, who was working on Nb edge junctions in Boulder, Colorado, might be a potential source of Nb films. Upon contact, Mr. Beall very kindly sent four wafers of Si on which 2,500 Å of Nb had been DC magnetron sputtered. The resistance ratio value for these films was 3.5. The electrical quality of junctions

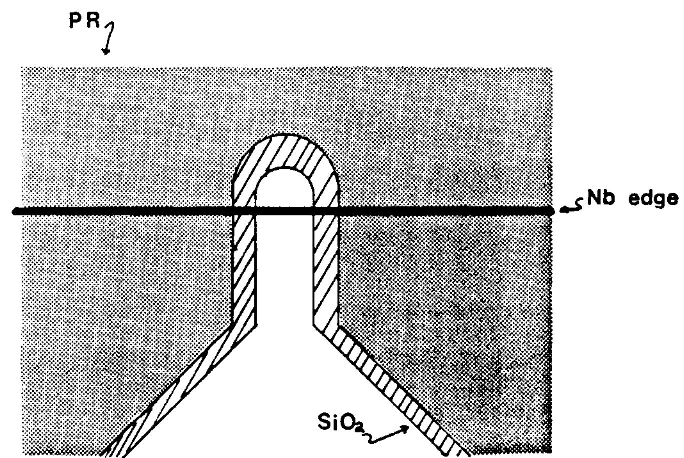

Figure 6.10 SiO_2 window defined junction

fabricated on a chip of this material was highly uniform with $R_{2,4}$ ratios of approximately 5.6. A typical I-V curve is shown in Fig. 6.11 and numerical values for R_{300}, R_2, R_4 and $R_{2,4}$ are tabulated in Table 6-1. A typical I-V curve obtained by Mr. Beall on this same Nb is shown in Fig. 6.12. A comparison of Fig. 6.11 and 6.12 indicates that the fabrication technology used in work described herein is superior. Unfortunately, the Si substrate material has very poor rf characteristics which prevented efficient coupling into such devices when mounted in mixer substrates. Subsequent Nb films, deposited on quartz substrates at NBS, proved to be of inferior quality, yielding poor, nonuniform I-V characteristics.

At this point, a great deal of confidence existed in our fabrication technology and device design; however, a source of high quality Nb films did not appear to be forthcoming. A switch from Nb to NbCN as a base electrode material was subsequently made. NbCN has a superconducting transition temperature of ~16 K, a large energy gap of ~2.4 eV and presents a very physically robust film. Of extreme importance is the reported characteristic of a high quality native oxide, with the absence of conductive suboxides. [34] Dr. Cukauskas of NRL [35] was contacted and he very nicely agreed to supply test NbCN films RF sputtered onto quartz substrates. This work is presently continuing toward optimization of NbCN/Pb alloy devices.

JCN	R_{300}	R_2	R_4	R_{24}
b	21.7	148	25.7	5.7
c	23.2	148	26.4	5.6
d	17.1	142	26.4	5.4
f	22.4	125	22.4	5.6

Table 6-1

Tabulated resistance valves for devices fabricated on NBS Nb

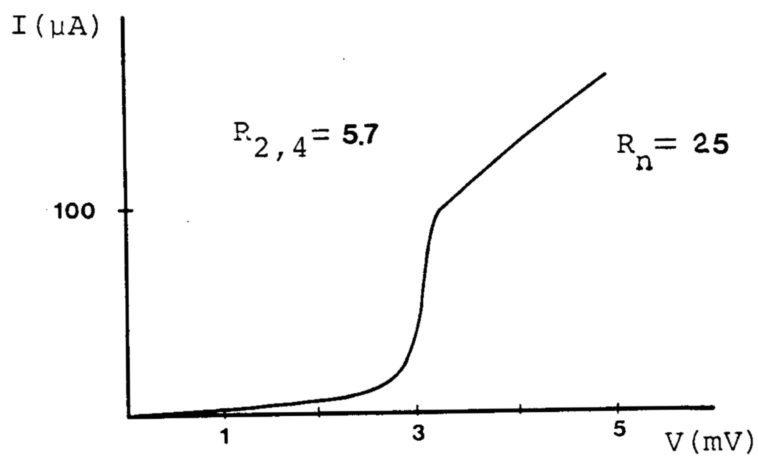

Figure 6.11 Typical I-V curve obtained with NBS Nb

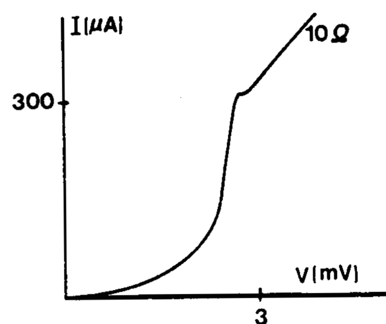

Figure 6.12 Typical I-V curve obtained by Mr. Beall on NBS Nb

CHAPTER VII

Investigation of NbCN

The switch to a NbCN base electrode did not require a significant alteration of the fabrication technology developed for Nb based junctions. The milling rates of the two materials are approximately equivalent, neither material is etched by BHF acid and both materials retain their superconducting properties when deposited as films of thickness greater than 1,000 Å. The anodically formed oxide of NbCN, however, is physically fragile and, therefore, cannot be utilized in a device structure.

Initial development with the ion gun technology yielded junctions which were electrically uniform across the chip, possessing low subgap current for voltages approximately two-thirds below the gap voltage (Fig. 7.1). Though the uniformity of results and low subgap current was very encouraging, the quasiparticle current jump was very rounded, indicating a damaged surface layer of NbCN. It was thought that the formation of the edge structure by ion milling was significantly damaging the superconductor lattice, resulting in a distribution of gap energies across the junction area. The ion cleaning and oxidation of this junction was performed at 450 volts. Junctions were then fabricated utilizing a 350 volt ion beam, resulting in

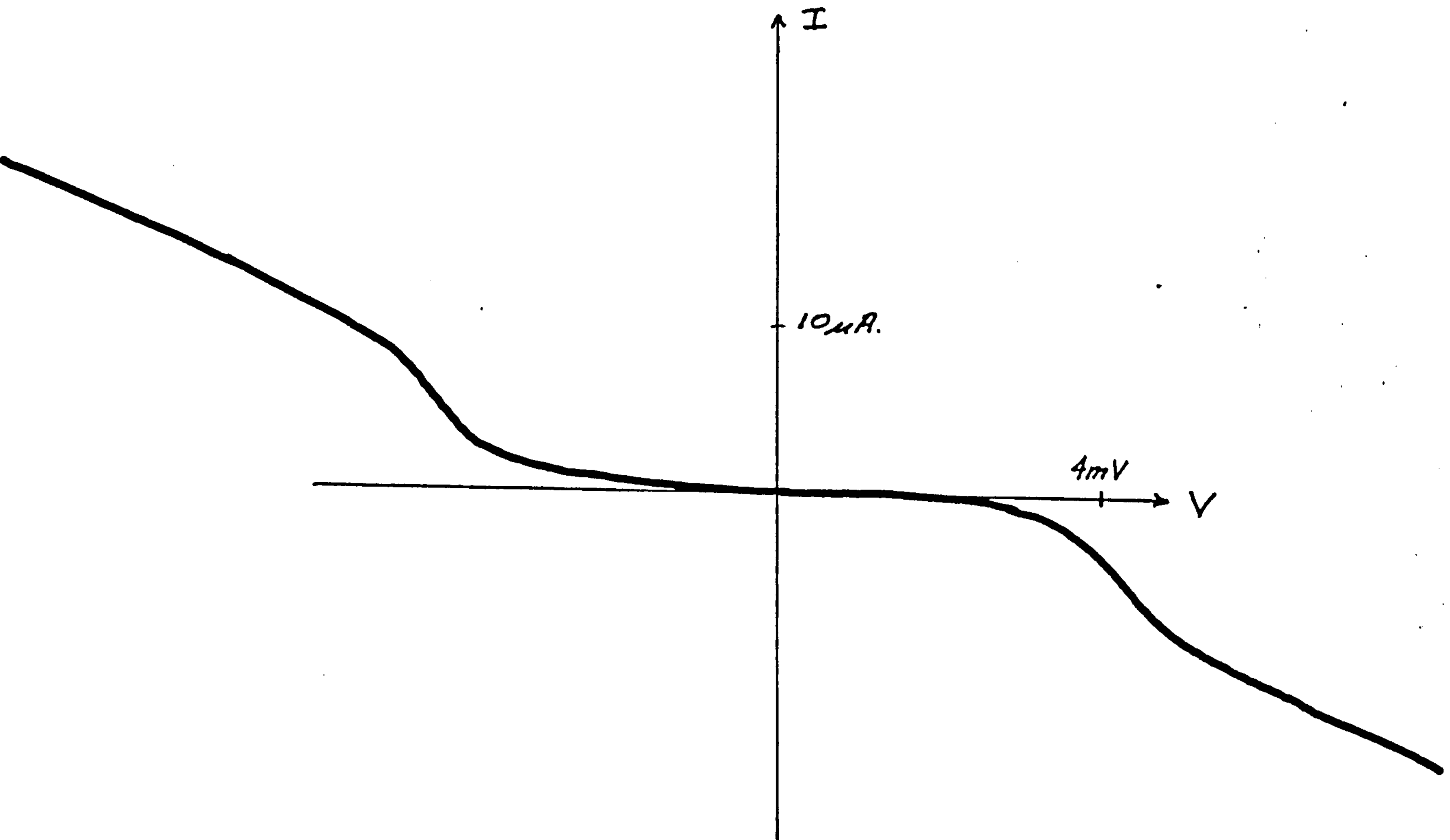

Figure 7.1

devices with improved, sharper tunneling characteristics at the gap voltages.

Since the ion gun used in this work was designed to operate at 600 eV, a number of modifications were made to increase the low beam currents obtained for voltages below 300 eV. Junctions were then fabricated, utilizing a 200 eV ion beam, with measured electrical characteristics which were superior to all previously fabricated devices at this lab (Fig. 7.2). Unfortunately, the efficiency of the ion gun used in this work deteriorated rapidly below 200 eV. Junctions have been fabricated with an ion beam voltage of 125 volts, however the resulting electrical characteristics were poor and non-uniform across the chip. Occasionally, a single device with high quality electrical characteristics was fabricated (Fig. 7.3) on a chip with generally poor electrical characteristics. It is therefore believed that further improvement of device electrical characteristics could be obtained if a high current density, low voltage ion beam was utilized.

After numerous attempts toward improving the performance of the ion gun had failed, a new 3 cm ion source (Model I) was obtained from Commonwealth Scientific Corporation. The efficiency of this ion source, when operated with a beam voltage greater than 100 eV, was excellent. Devices fabricated with this ion source, however, were of poor quality, even when the fabrication was

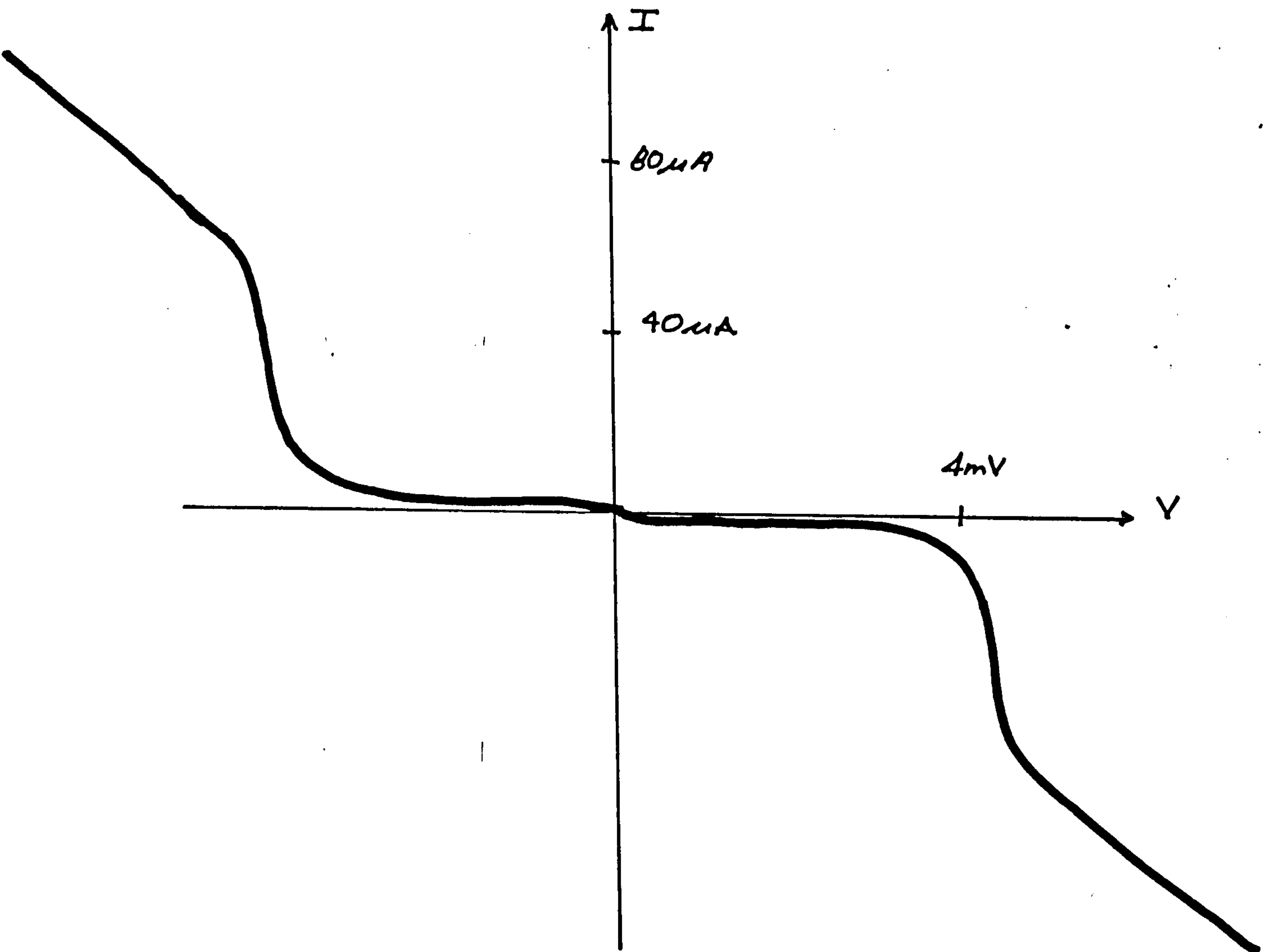

Figure 7.2

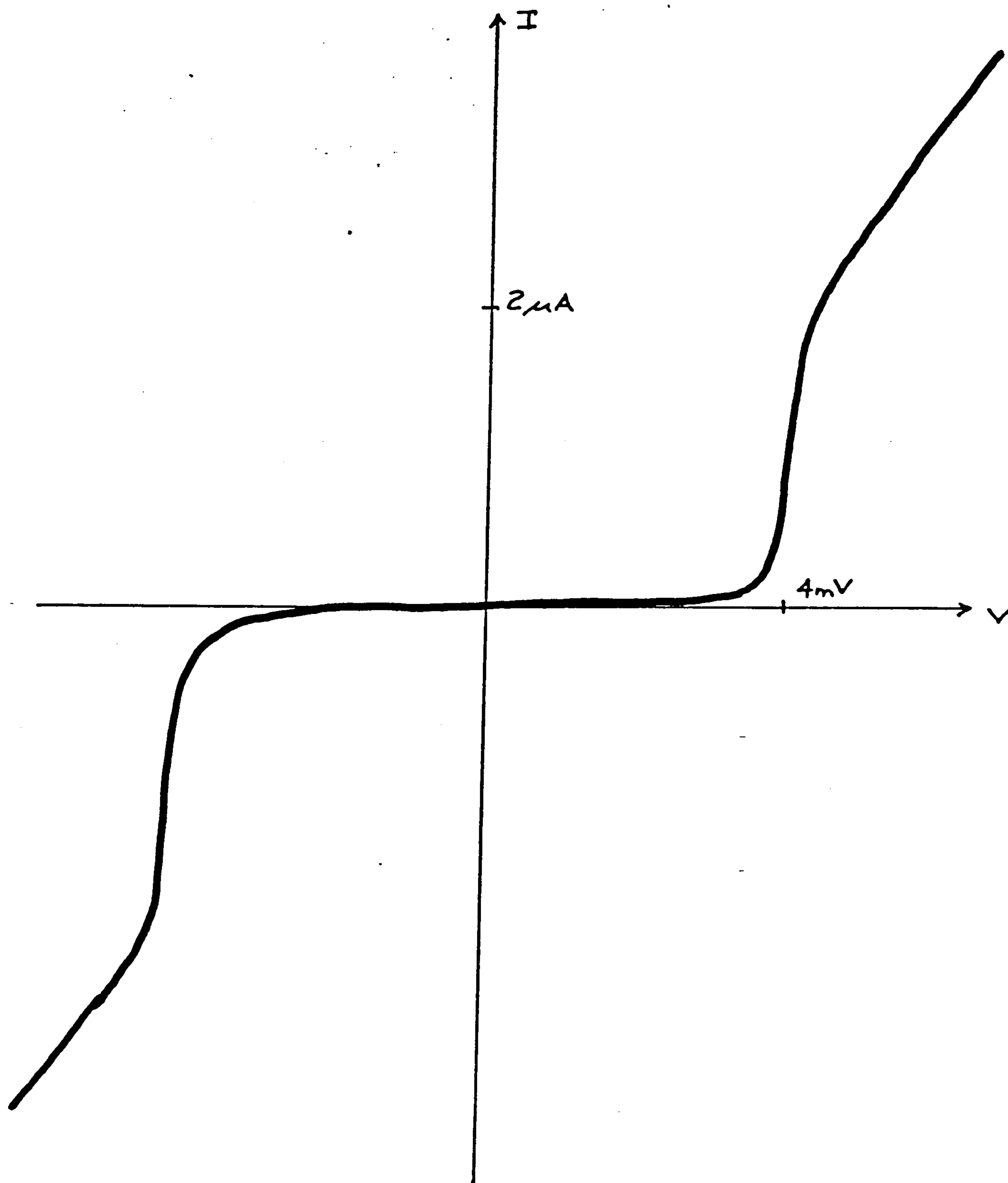

Figure 7.3

performed with a 400 eV ion beam voltage. The base pressure of the chamber was 5×10^{-8} torr, however after 20 minutes of ion source operation the pressure would rise to 1×10^{-6} torr. Again the insulators were immediately suspected, however due to the geometry of the ion gun it was impossible to fabricate glass replacement pieces. Tungsten, thoriated tungsten, tantalum and Nb filaments were all examined in an attempt to find a more efficient emission source. Different ion source operation schedules have also been examined. For one such run, the ion gun was operated at a much higher discharge and filament current than normal, with the sample turned away from the beam. The ion source was then turned off and the pressure allowed to return slowly to a 10^{-8} torr range. This process was repeated five times in an effort to rid the insulators of contaminants. The junctions which were subsequently fabricated possessed typically poor electrical characteristics.

In an effort to provide an efficient low voltage ion source, the vacuum chamber was modified to permit plasma etching (Fig. 7.4). The plasma technology has been utilized successfully for large area planar NbCN junctions (Hikita). It should also permit a low voltage (hence low damage) cleaning and oxidation of the NbCN edge surface. Initial tests of the plasma system indicate that a plasma can easily be obtained for discharge potentials above 25 volts and gas pressures above 1 μm. Devices will be fabricated after the

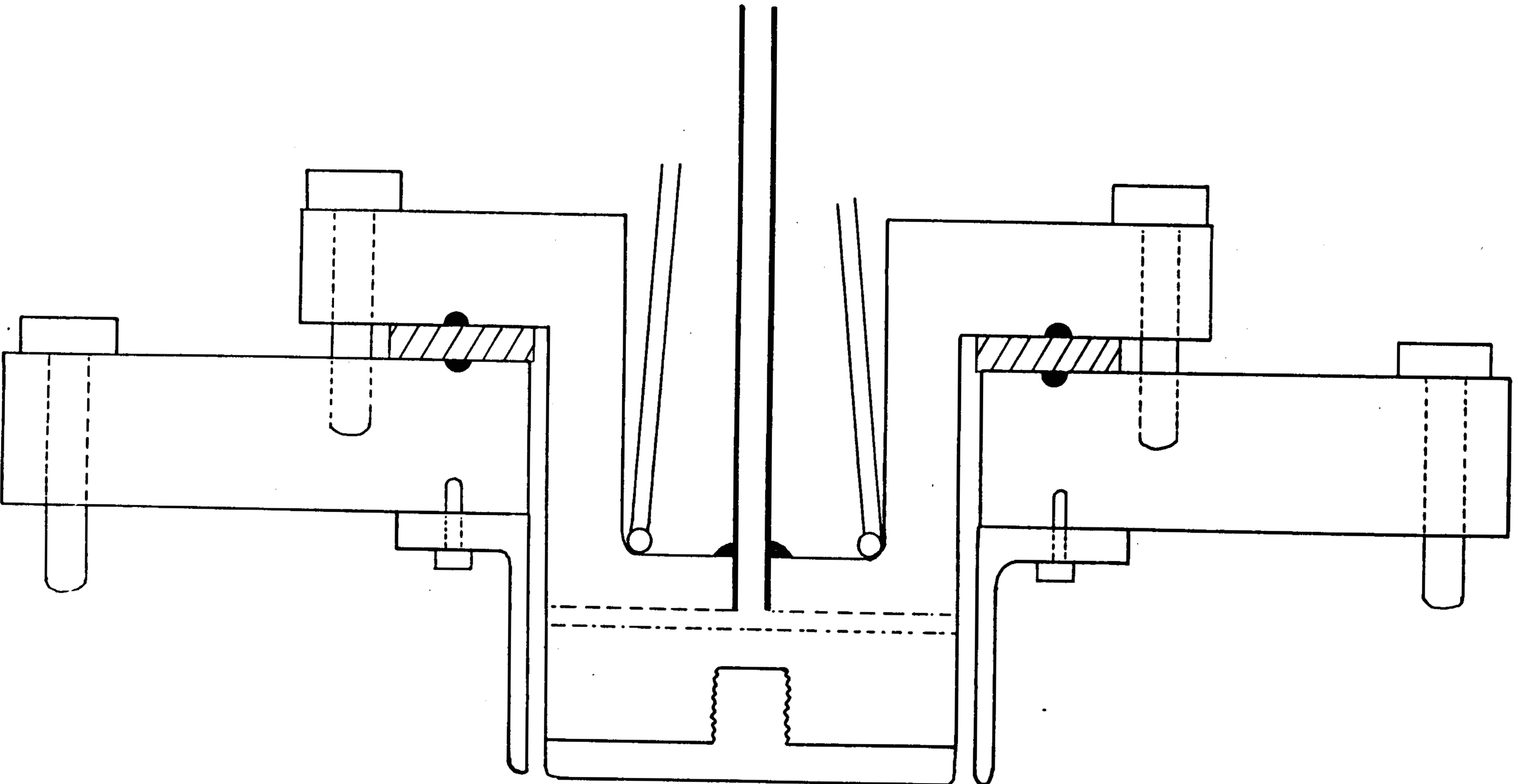

Figure 7.5

etch rate of the system as a function of discharge voltage is determined. It is expected that the most difficult parameters to determine will be the oxygen partial pressure and the oxidation time.

CHAPTER VIII

Conclusion and Recommendation for Future Research

During the course of this work, a number of procedures were developed for fabricating Nb/Pb alloy and NbCN/Pb allow devices. The quality of the tunnel barriers resulting from the oxidation of Nb has been found to be extremely sensitive to contamination. A great deal of effort was expended toward solving a critical degradation of I-V characteristics, due to barrier contamination. It was discovered that the electrical quality of the device was even sensitive to the virtual leaking of gases from porous ion gun insulating rings. It was also shown that the device I-V characteristics are extremely sensitive to the quality of the Nb material.

An investigation of the use of NbCN base electrode films is presently underway. The reported [36] absence of conductive suboxide in the native oxide of NbCN is very encouraging. However, the superconductive quality of the NbCN surface has been found in this work (and others [37]) to be very sensitive to ion bombardment and subsequent surface damage. The use of a plasma etching technolology is presently being explored. This will hopefully permit a low voltage cleaning and oxidation of the NbCN edge surface. The introduction of CF_4 during the cleaning process in order

to clean "chemically" instead of "physically" (perhaps resulting in less surface damage) is also being considered.

The use of an artificial barrier should also be investigated. Excellent results have been obtained by Gurvitch et. al. [38] using an Al_2O_3 barrier with 60 m^2 - 400 μm^2 junction area $Nb/Al_2O_3/PbBi$ and all Nb structures. The subgap current of these devices have also been fabricated [39] which have an unprecedented I-V quality, comparable to the I-V quality of the best Pb based junctions. However, successful micron sized junctions have yet to be fabricated.

The plasma, CF_4 and Al_2O_3 technologies are presently being developed at this lab. The initial results of the plasma technology are promising, with $R_{2,4}$ ratios greater than 20 measured for 2.5 μm^2 devices. Initial results from the Al_2O_3 technology are expected before January. It is felt that all three technologies hold great potential and are worth pursuing. We are presently investigating alternative avenues for future funding.

Appendix A

The general procedure used for fabricating Nb/PbBi tunnel junctions of ~1 μm^2 area is summarized in this appendix. While a particular sequence of specific steps is given, variations on each were performed in the course of development of this fabrication technology.

I. Nb RF Deposition

A. Clean quartz substrates

1. Boil and degrease in ethanol, trichloroethylene, and methanol ("organic clean")

2. Dry bake 120°C for 20 min.

B. RF sputter deposition of 2,000 Å of Nb

1. System base pressure of 2×10^{-7} torr
2. Deposition rate of 40 Å/sec., 10 μm Ar
3. H_2O cooled substrate table

II. SiO_2 RF Deposition

A. Clean chip

1. organic clean
2. Dry bake 80°C for 20 min.

B. RF presputter of 3,000 Å SiO_2 in "empty" chamber

C. RF sputter deposition of 3,000 Å of SiO_2

1. System pressure of 1×10^{-6}
2. Deposition rate of 50 Å/sec., 15 μm Ar
3. H_2O cooled substrate table

4. 500 volts (target), 50 volts (substrate)

III. Base Electrode Photolithography

A. If this photolithographic step follows immediately after SiO_2 deposition, then the following cleaning step is omitted.

B. Clean chip

1. Organic clean
2. Dry bake 80°C for 20 min.

C. Spin AZ1350J photoresist

1. 3,500 RPM 30 sec. (approximately 2 μm)

D. Treatment prior to illumination

1. Prebake 80°C for 25 min.
2. Allow to cool at room temperature (5 min)

E. Exposure with base electrode mask

1. Relative UV intensity 49 (Preco Aliguer)
2. 25 sec.

F. Develop photoresist

1. AZ developer/de-ionized water (DI) 1:1
2. Develop by "inspection" (The photoresist is developed until it appears to have stopped being removed (~ 20 sec.). Development is then continued a few seconds further.)
3. Three rinses in dionized water (DI)
4. Postbake 120°C for 20 min.

IV. Ion Mill of Base Electrodes

A. Chip mounted with Apiezon-L grease to Nb covered substrate holder

B. Operate ion gun for 30 min. with substrate turned away from beam

1. V_{BS} = 600 volts
2. V_A = -50 volts
3. V_{dis} = 50 volts
4. I_{fil} = 14 amps
5. I_b = 50-70 $\mu A/cm^2$
6. I_{dis} = 0.1 - 0.3 amps
7. System pressure $\leq 1 \times 10^{-6}$ torr
8. Cool substrate holder to 180 - 230 K by means of LN_2

C. Ion mill base electrode

1. Continue milling 15 minutes past the time at which the exposed SiO_2 and Nb are removed (quartz substrate becomes visible)
2. Warm chip to room temperature by forcing N_2 gas through LN_2 feedthroughs

D. Treatment after ion milling

1. Rinse twice in boiling xylene to remove Apiezon-L grease
2. Remove photoresist with aceton
3. Rinse with methanol

V. Contact Window Formation

A. Clean chip

1. Organic clean
2. Dry bake 80°C for 20 min.

B. Spin AZ1350J photoresist

1. 4,000 RPM 30 sec.

C. Treatment prior to illumination

1. Prebake 80 C for 20 min.
2. Allow to cool at room temperature (5 min.)

D. Exposure with contact window mask

1. Relative UV intensity 49 (Preco)
2. 25 sec.

E. Develop photoresist

1. AZ/DI 1:1
2. Develop by "inspection"
3. Three rinses in DI water
4. Postbake 120°C for 20 min.

F. Open contact windows in SiO_2 with BHF

1. BHF 3-1/2 - 4-1/2 minutes (60 ml H_2O, 40 ml NH_4F, 9 ml HF)
2. Two rinses in DI water

VI. Gold Contact Deposition

A. Affix chip to H_2O cooled substrate platform with Apiezon-L grease.

B. RF sputter of Au with shutter covering chip

1. System pressure of 1×10^{-5} torr
2. 5,000 Å Au

C. Continue pumping until system pressure of

$\sim 2 \times 10^{-6}$ is obtained

D. RF sputter of Au with shutter covering chip

1. 15 μm Ar
2. 3,000 Å Au
3. 700 volts (target), 75 volts (substrate)

E. RF sputter etch of chip

1. 15 μm Ar
2. ~100 Å removed
3. 500 volts (substrate), 50 volts (target)

F. RF sputter of Au with shutter covering chip

1. 15 μm Ar
2. 1,000 Å Au
3. 700 volts (target), 75 volts (substrate)

G. RF sputter deposition of Au on chip

1. 15 μm Ar
2. 6,000 Å of Au
3. 700 volts (target), 75 volts (substrate)

H. Treatment after Au deposition

1. Rinse twice in boiling xylene to remove Apiezon-L grease
2. Liftoff gold by soaking in acetone
3. Remove with methanol

VII. Counter Electrode Photolithography

A. Clean chip

1. Organic clean
2. Dry bake 80°C for 20 min.

B. Spin AZ1350J photoresist

1. 6,000 RPM, 30 sec (approximately 1.5 μm)

C. Chlorobenzene soak

1. 15 min. soak
2. Blow dry with N_2 gas and let sit for 5 mins.

D. Exposure with counter electrode mask

1. Relative UV intensity 49 (Preco)
2. 30 sec.

E. Develop photoresist

1. AZ/DI 1:1
2. Develop for a period equal to twice the observed optical development time (90 sec.)
3. Three rinses in DI water

VIII. Ion Mill Clean, Oxidation and PbBi Evaporation

A. Load Ta evaporation boat

1. 0.540 grams of Pb, 0.210 grams of Bi

B. Mount chip with Apiezon-L grease to Nb covered substrate holder

C. Operate ion gun for 30 min. with substrate turned away from beam

1. V_{BS} = 600 volts
2. V_A = -50 volts
3. V_{dis} = 50 volts
4. V_{fil} = 14 amps
5. I_b = 50-75 $\mu A/cm^2$
6. I_{dis} = 0.1-0.3 amps
7. System pressure < 8×10^{-7} torr
8. Argon pressure 1×10^{-4} torr
9. Cool substrate holder to 180-210 K

D. Ion clean

1. 45° incidence
2. clean for 15 min.
3. Increase evaporation current to 40 amps
4. Continue cleaning for 20 secs.

E. Oxidation and evaporation (this follows immediately after the cleaning step)

1. Admit O_2 to total pressure of 1.3×10^{-4} torr
2. I_b = 20-25 $\mu A/cm^2$
3. I_{fil} = 15 amps
4. Twenty-five sec. later, increase evaporation current to 60 amps
5. Ten sec. later, turn gun off and increase evaporation current to 90 amps
6. Open evaporation shutter and turn substrate into evaporant
7. Evaporate to completion
8. Warm chip to room temperature by forcing N_2 gas through LN_2 feedthroughs

F. Clean chip and PbBi liftoff

1. Rinse twice in room temperature xylene to remove Apiezon-L grease
2. Liftoff gold by soaking in acetone (light ultrasonic agitation necessary)
3. Blow dry with N_2 gas
4. Spin protective layer of AZ1350J photoresist

Appendix B

The choice of an ion gun technology instead of a more conventional RF plasma technology was made for several reasons. With RF sputtering, the discharge is initiated with the application of an electric field. Excited electrons collide with the chosen working gas atoms resulting in an ionization of these atoms; once the plasma is established, it is maintained by secondary electron emission. Also, with RF sputtering, the substrates and the target are located essentially in the plasma.

Ion sources, however, utilize thermionic emission to sustain the plasma. This permits operation of ion sources at pressures ($\lesssim 10^{-4}$ torr) two orders of magnitude lower than conventional sputtering sources. Also, with ion sources, the plasma region is physically separate from the material to be milled. Because of these two characteristics, the ion source technology should be a cleaner process.

In this Appendix, the fundamentals of ion milling operation will be outlined and the specific system utilized in this work will be considered.

Section I

A typical ion source with power supplies is shown in Fig. B.1. The working gas of the system (typically Ar) enters the discharge chamber through a port in the back of the

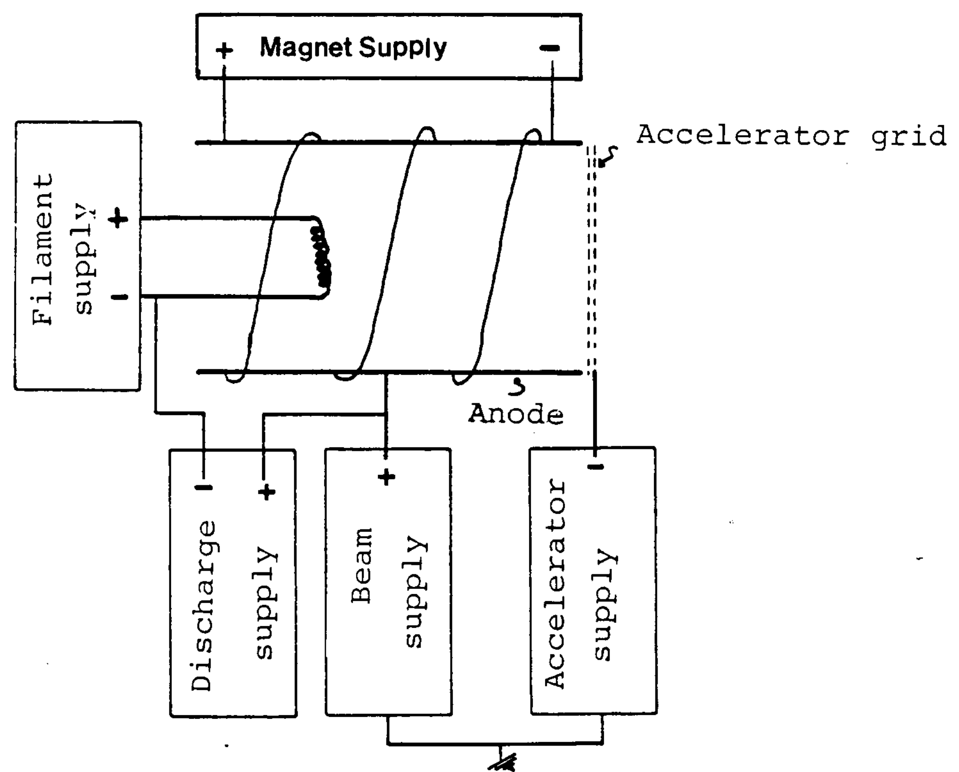

Figure B.1 Typical ion source schematic

gun. Electrons from the filament are thermionically emitted and are accelerated (by a relativly low "discharge" potential, $V_{ds} \sim$ 20-70 volts) to the anode chamber walls. Some of these energetic electrons from the cathode collide with the atoms of the working gas producing a plasma of electrons and ions. This ionization chamber is maintained at a potential V_{bs} above ground. Some of these ions pass through the screen grid and are accelerated through the aligned holes of the negatively biased accelerator grid. The ion beam results from the combination of each of these individual beamlets. The plasma potential is approximately equal to the anode potential which is set by the beam power supply (V_{bs}). With a target connected electrically to ground, the energy of the ions impinging upon the chip is given by the beam power supply potential V_{bs}.

Since ion sources typically operate at such low pressures ($\sim 10^{-4}$ torr), the probability of an electron-source atom collision in the discharge chamber is typically increased by the application of an axial magnetic field between the anode and cathode. The much heavier ions are relatively uneffected. The discharge voltage (V_{ds}) is typically chosen so as to produce only singly ionized atoms. Since a doubly charged ion will obtain twice the energy of a singly charged ion, it will also produce approximately twice the surface damage. Singly charged ions also strike the cathode with an energy equal to eV_{ds}. Doubly charged

ions can, therefore, significantly increase the resulting sputtering contamination since the sputtering rates of most materials increase dramatically with ion energy above typical discharge potentials.

The ion beam is extracted from the discharge chamber by a set of grids (the "ion optics"). Typically, the ion optics consists of two closely spaced graphite grids, though single and multigrid ion optic systems can be utilized for special applications. [40] The screen grid is not biased externally but allowed to float electrically. Its potential has been found to approximately equal the anode potential. The accelerator (or extractor) grid is commonly biased at a negative potential, V_a, while the target is electrically connected to ground. The variation of potential in a typical dual grid system is shown in Fig. B.2. [41]

The ion current is controlled by V_T, the sum of the magnitudes of V_a and V_{bs} ($V_T = V_a + V_{bs}$). The accelerating grid is negatively biased in order to obtain a larger ion current and to prevent backstreaming of electrons into the ion gun. The later reason is of particular importance if a neutralizer filament is positioned after the dual grids. In such a case, the filament is utilized to supply electrons to create a charge neutral beam such that the "neutralized" beam has equal densities of electrons and ions. The accelerating grid presents a negative barrier to these neutralizing and other electrons. Increasing $|V_a|$, however, will also

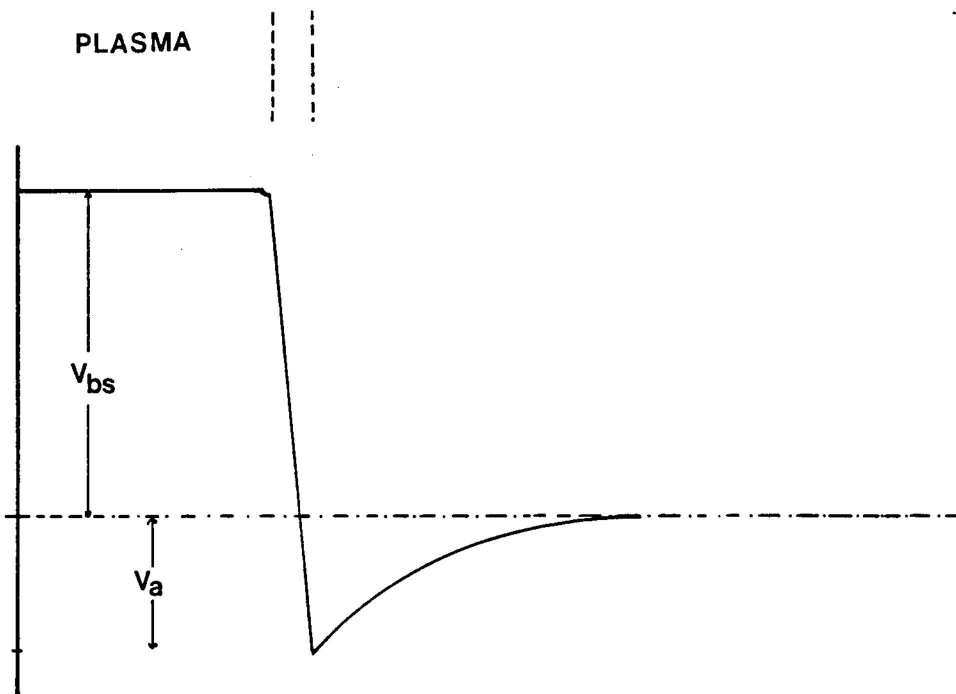

Figure B.2 Variation of potential in a typical dual grid system

increase the beam divergence as well as the ion current striking the accelerator grid. The sputtering yield of this grid and resulting contamination of the target will also increase. The accelerating voltage should, therefore, be adjusted to avoid both backstreaming of electrons into the ion gun and excessive sputtering of the extractor grid.

The ion current is also strongly controlled by the grid separation and geometry. Smaller grid spacing results in a larger electric field between the two grids (for a given V_T) and hence a larger ion current. Typical grid spacings range from 20-200 mils. [42]

Section II

A schematic of the vacuum system, associated with the ion source utilized in this work, is shown in Fig. B.3. The system is pumped by a diffusion pump through an optically dense liquid nitrogen cold trap. An ion gun, obtained from the Commonwealth Scientific Corporation, is mounted to the side of the aluminum chamber. This chamber is equipped with a LN_2 cooled rotatable substrate holder, evaporation boat and evaporation shutter. The beam current density is measured by a 1 cm^2 Nb covered current probe positioned approximately 1/4" to the side and 1/2" behind the substrate holder. A quartz window is positioned on the top of the chamber to permit viewing of the substrate while milling. The working gases for this system are research grade argon and oxygen (Ar, 99.995%, O_2, 99.999%). All valves and tubes are

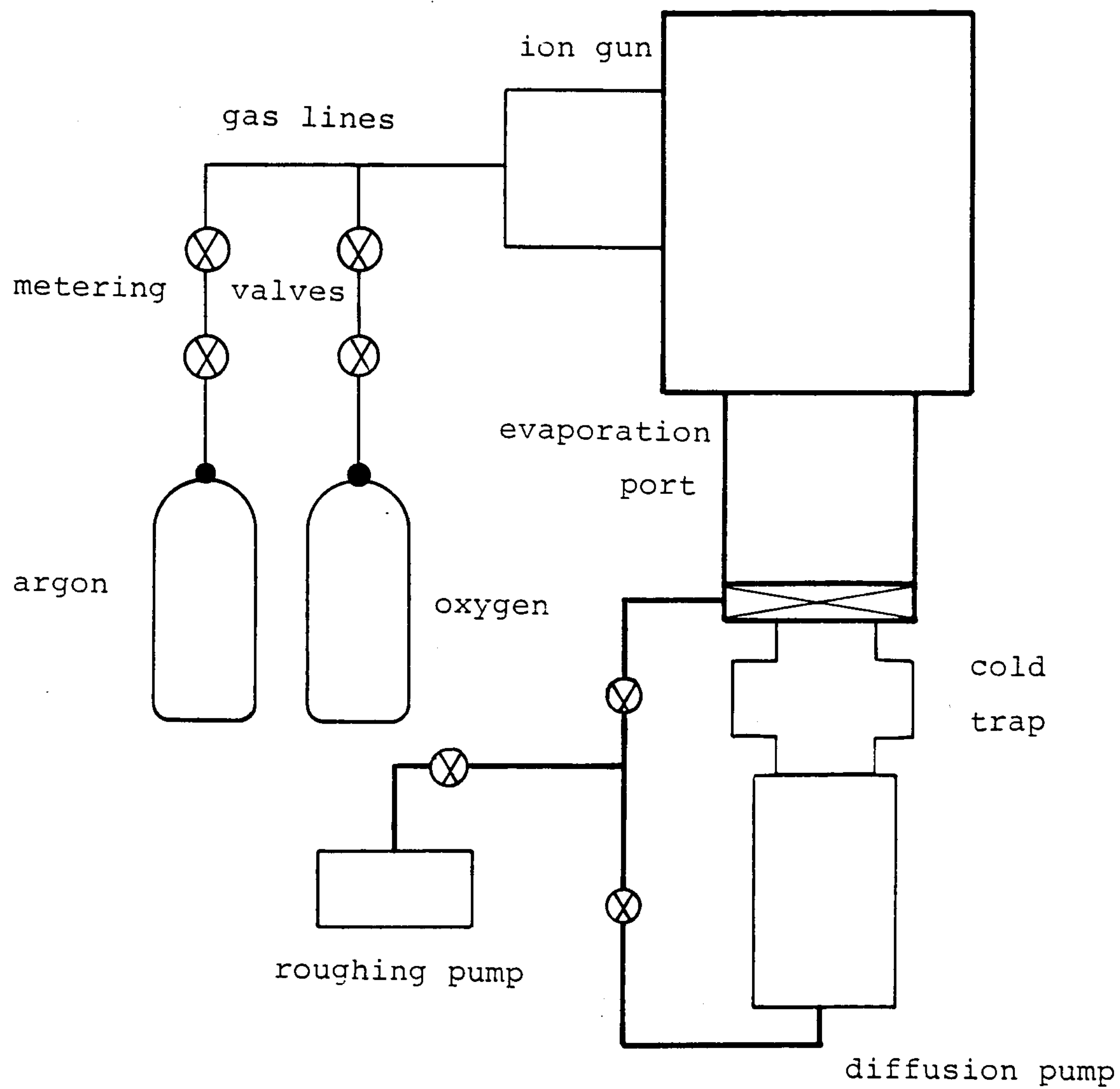

Figure B.3 Schematic of the vacuum system associated with the ion source in this work

stainless steel except a final 12" length of teflon tubing which is required for electrical isolation of the anode chamber. Fine metering valves are utilized to regulate gas flow into the anode chamber.

A schematic of the ion gun is shown in Fig. B1. An aluminum cyclinder serves as both the anode and a holder for the wire turns of the electromagnetic. The anode, screen grid, accelerating grid and retaining piece were each electrically separated by alumina insulating rings while O-ring seals exist between all of the components. Carbon grids with a 60 mil separation and 3 cm beam width are utilized. Both tungsten and thoriated tungsten filaments have been used with similar results. Typical electrical operating conditions for this ion gun are given in Table B-1. Subsequent changes made to this ion gun configuration are described in Chapter V.

System pressure	1×10^{-6} torr
Argon pressure	1×10^{-4} torr
V_{BS}	600 volts
V_A	-50 volts
V_{dis}	50 volts
I_{fil}	14 amps
I_{dis}	.2 amps
I_b	60 $\mu A/cm^2$
I_{sub}	200 K

Table B-1

Typical operating conditions of the ion source system

References

1. M.J. Feldman, NASA Goddard Institute for Space Studies, New York, N.Y. (Fig. 1.1 reprinted from NRAO lecture).

2. J.R. Tucker, Predicted Conversion Gain in Superconductor-Insulator-Superconductor Quasiparticle Mixers, Appl. Phys. Lett. Vol. 36, No. 6, 15 March 1980, pp. 477-479.

3. A.R. Kerr, NASA Goddard Institute for Space Studies, New York, N.Y.

4. T.M. Shen, P.L. Richards, R.E. Harris and F.L. Lloyd, Conversion Gain in mm-Wave Quasiparticle Heterodyne Mixers, Appl. Phys. Lett., Vol. 36, No. 9, 1 May, 1980. pp. 777-779.

5. A.C. Rose-Innes and E.H. Rhoderick, Introduction to Superconductivity. Pergamon Press, U.K., 1978, p. 120.

6. Ibid.

7. J. Bardeen, L.N. Cooper and J.R. Schrieffer, "Theory of Superconductivity," Phys. Rev., Vol. 108, 1 December, 1957, pp. 1175-1204.

8. M.J. Feldman, NASA Goddard Institute for Space Studies, New York, N.Y.

9. J.R. Tucker and M.J. Feldman, "Quantum Detection at Millimeter Wavelengths", submitted to Reviews of Modern Physics, 26, December 1984.

10. McCumber, D.E., J. Appl. Phys., 39, 1968, p. 3113.

11. M.J. Feldman, NASA Goddard Institute for Space Studies, New York, N.Y.

12. A.R. Kerr, NASA Goddard Institute for Space Studies, New York, N.Y.

13. J.R. Tucker and M.J. Feldman, "Quantum Detection at Millimeter Wavelengths", submitted to Reviews of Modern Physics, 26, December 1984.

14. S. Rudner, M.J. Feldman, E. Kollberg, and T. Claeson, J. Appl. Phys., 52, 1981, p. 6366.

15. S. Imai, S. Morita, A. Ishikawa, Y. Takeuti, and N. Mimkoshiba, IEEE Trans. Magn., MAG-21, 1985.

16. J.R. Tucker and M.J. Feldman, "Quantum Detection at Millimeter Wavelengths", submitted to Reviews of Modern Physics, 26, December 1984.

17. J.H. Magerlein, Specific Capacitance of Josephson Tunnel Junctions, IEEE Transactions on Magnetics, Vol. MAG-17, No. 1, January 1981, pp. 280-289.

18. R.F. Broom, S.I. Raider, A. Oorenbrug, R.E. Drake, and W. Walter, IEEE Trans. on Electron Devices, Vol. ED-27, No. 10, October 1980, pp. 1998-2008.

19. S. Rudan, M.J. Feldman, E. Kollberg, and T. Claeson, Superconducting-insulator-superconducting mixing with arrays at millimeter wave frequencies, J. Appl. Phys., 52(10), October 1981, pp. 6366-6376.

20. J.I. Upshur, Ph.D. Dissertation, University of Virginia, August, 1983.

21. R.F. Broom, R. Jaggi, Th. O. Mohr, and A. Oosenbrug, IBM J. Res. Dev., 24, 1980, pp. 206.

22. H.C.W. Huang, S. Basavaiah, C.J. Kircher, E.P. Harris, M. Morakani, S. Klepner, and J.H. Greiner, IEEE Trans. Electron Devices, vol. ED-27, 1980, pp. 1979-1987.

23. J.H. Greiner, Oxidation of lead films by rf sputter etching in an oxygen plasma, J. Appl. Phys., vol. 45, 1974, pp. 32-37.

24. G.J. Dolan, T.G. Phillips and D.P. Woody, Low Noise 115 GHz Mixing in Superconducting Oxide-Barrier Tunnel Junctions, Appl. Phys. Lett., Vol. 34, No. 5, 1979, pp. 347-349.

25. A.R. Kerr, S.-K. Pan, M.J. Feldman, and A. Davidson, Physica, 108B, 1981, pp. 1369.

26. M. Murakami, Thin Solid Films, 59, pp. 105, 1979; S. B-savaiah, M. Murakami, and C.J. Kircher, J. of Phys., vol. 39, 1978, C6-1247.

27. J.V. Gates, S.S. Pei, A comparison of temperature cycling stability of Pb-Alloy Josephson Junctions with Various Counter Electrode Materials, IEEE Trans. on Magn., Vol. MAG-19, No. 3, May 1983, pp. 816-819.

28. A.C. Rose-Innes and E.H. Rhoderick, Introduction to Superconductivity. Pergamon Press, U.K., 1978, p. 120.

29. S.I. Raider, R.E. Drake, IEEE Trans. Magn., MAG-17, No. 1, January 1981, pp. 299-302.

30. S.I. Raider, R.W. Johnson, T.S. Kuan, R.E. Drake, and R.A. Pollak, IEEE Trans. on Magn., No. 3, May 1983, pp. 803-806.

31. S.I. Raider, R.W. Johnson, T.S. Kuan, R.E. Drake, and R.A. Pollak, IEEE Trans. on Magn., No. 3, May 1983, pp. 803-806.

32. S.I. Raider, R.W. Johnson, T.S. Kuan, R.E. Drake, and R.A. Pollak, IEEE Trans. on Magn., No. 3, May 1983, pp. 803-806.

33. J. Beall, National Bureau of Standards, Boulder, Colorado.

34. R.B. van Dover, D.D. Bacon, and W. Robert Sinclair, Appl. Phys. Lett., 41(8), October 1982, pp. 704-706.

35. E.J. Cukauskas, Naval Research Laboratory, Washington, D.C.

36. R.B. van Dover, D.D. Bacon, and W. Robert Sinclair, Appl. Phys. Lett., 41(8), October 1982, pp. 704-706.

37. Makoto Hikita, Koyi Takei, and Masaru Igarashi, Ar ion bombardment effects of NbN/Pb Josephson functions with plasma oxidized barriers, J. Appl. Phys., Vol. 54(12), December 1983, pp. 7066-7072.

38. M. Gurvitch, J.M. Rowell, H.A. Huggins, M.A. Washington and T.A. Fulton, Nb josephson tunnel junctions with thin layers of Al near the barrier, IEDM 81, 1981, pp. 115-117.

39. M. Gurvitch, M.A. Washington, H.A. Huggins, and J.M. Rowell, IEEE Trans. on Magn., No. 3, May 1983, pp. 791-794.

40. H.R. Kaufman, J.J. Cuomo, and J.M.E. Harper, J. of Vacuum Science and Technology, Vol. 21, Sept./Oct. 1982, pp. 725-736.

41. H.R. Kaufman, Fundamentals of Ion-Source Operation, Commonwealth Scientific Corporation, 1984.

42. H.R. Kaufman, Fundamentals of Ion-Source Operation, Commonwealth Scientific Corporation, 1984.

DISTRIBUTION LIST

Copy No.	
1-3	National Aeronautics and Space Administration Goddard Space Flight Center Greenbelt, Maryland 20771 Attention: Dr. Anthony Kerr Code 130
4-5 *	NASA Scientific and Technical Information Facility P. O. Box 8757 Baltimore/Washington International Airport Baltimore, Maryland 21240
6-7	E. H. Pancake Clark Hall
8	E. A. Parrish, EE
9	R. J. Mattauch, EE
10 *	SEAS Files

*One reproducible copy.

JO#6916:rsr